

Aus der Klinik für Strahlentherapie und Radioonkologie
der Medizinischen Fakultät Mannheim, Universität Heidelberg
(Direktor: Prof. Dr. med. Frank A. Giordano)

Geometric Errors and Effects Analysis for the INTRABEAM Source under Treatment Conditions

Inauguraldissertation
zur Erlangung des Doctor scientiarum humanarum (Dr. sc. hum.)
der
Medizinischen Fakultät Mannheim
der Ruprecht-Karls-Universität
zu
Heidelberg

vorgelegt von
Zulfa

aus
Bengkalis, Indonesia
2023

Dekan: Herr Prof. Dr. med. Sergij Goerd.....

Doktormutter/Doktorvater: Herr Prof. Dr. med. Daniel Bürgy, MSc.....

CONTENTS

LIST OF FIGURES	IV
LIST OF TABLES.....	VIII
1 INTRODUCTION	1
1.1 Treatments of breast cancer and the need for an accurate and reliable dose calculation algorithm for the treatment with the INTRABEAM device	1
1.2 Available TPSs and the developing dose calculation algorithm	4
1.3 Aims and scopes of the work.....	6
2 MATERIALS AND METHODS.....	7
2.1 The INTRABEAM source and spherical applicators	7
2.2 Overview of breast IORT treatment with the INTRABEAM device.....	8
2.3 Overview of the Geant4 Monte Carlo Toolkit	9
2.3.1 Geometry and Material classes	12
2.3.2 Primary particle generation.....	13
2.3.3 Stepping Action	13
2.4 The Geant4 Monte Carlo dose calculation algorithm.....	14
2.5 Modelling the treatment geometries	15
2.5.1 DICOM interface and the reconstruction of patient geometry ...	16
2.5.2 Slice selection criteria	21
2.5.3 Volume overlapping and the cavity.....	23
2.6 Applicator position and orientation	34
2.6.1 Implementation of the position and orientation shifts into the <i>PrimaryGeneratorAction</i> class of the source model	36
2.6.2 Derivation of scoring equations the spherical applicator and their implementation within the <i>SteppingAction</i> class of the source model. .	37
2.6.2.1 The coordinate system and the scoring surface of the source	37
2.6.2.2 The reference coordinate system and the scoring surface for the spherical applicator.....	38
2.6.2.3 Particle scoring for the spherical applicator	39

2.6.2.4	Translation and rotation	40
2.7	The dose scoring algorithm	43
2.8	The visualization	45
2.8.1	The initial feature of the GUI	46
2.8.2	Methods to run a simulation.....	47
2.8.3	The new feature of the GUI	48
2.9	Dose quantifications.....	50
2.9.1	Dose in heterogeneous medium.....	50
2.9.2	Dose in homogeneous medium vs. heterogeneous medium	51
2.9.3	Effects of Geometric errors.....	52
2.9.4	Analysis of the DVH	54
2.10	Dose uncertainty calculations	55
2.11	Data Processing analyses	56
3	RESULTS.....	57
3.1	Effect of volume overlapping	57
3.2	Applicator position and orientation	57
3.2.1	The PrimaryGeneratorAction	57
3.2.2	The SteppingAction.....	58
3.3	Visualization	59
3.4	Effect of heterogeneities on dose distributions	61
3.4.1	The dose profiles.....	61
3.4.2	The DVHs of the homogeneous vs. the heterogeneous CTs	64
3.5	Effect of geometric errors on dose distributions.....	68
3.5.1	Air gap	68
3.5.2	Blood interface	74
3.6	The calculated dose uncertainty	81
4	DISCUSSION.....	84
4.1	Effects of tissue heterogeneity	86
4.2	Effect of the air gap and blood interface	89
4.3	The dose uncertainty	94
4.4	Limitations and future works.....	96

5	SUMMARY.....	99
6	REFERENCE LIST	100
7	APPENDIX.....	108
	7.1 Structure of a .g4dcm, .g4dcmb, or .g4cdcm file	108
	7.2 The reconstructed patient geometry.....	109
	7.3 The dose points of the other OARs	115
8	CURRICULUM VITAE.....	116
9	ACKNOWLEDGMENTS.....	118

LIST OF FIGURES

Figure 2-1. a. The INTRABEAM XRS and its b. spherical applicators ⁴².....7

Figure 2-2. IORT procedure during a BCS. a. determination of the tumor position, b. creating access (incision) to the tumor, c. surgical removal of the tumor, d. positioning an appropriate applicator in the tumor bed, e. the tumor bed irradiation, and f. applicator removal after 20-50 minutes of irradiation and incision closing ⁴⁵.9

Figure 2-3. The Geant4 kernel and its functionality.....10

Figure 2-4. a. Tissue characterization phantom, Gammex-RMI 467. b. The calibration curve relates the HUs and electron density.18

Figure 2-5. The 3D visualization of the reconstructed patient geometry. For the visualization purpose, the initial resolution is reduced by factor of 8 in the x and y axes.....21

Figure 2-6. A cropped CT image of a corresponding slice. The included OARs are the left breast (without the target volume), heart and both lungs.....23

Figure 2-7. Visualization of the reconstructed patient geometry. a. with no cavity and b. with the cavity. The created cavity has the size corresponding to the size of the used spherical applicator.....34

Figure 2-8. Visualization of the trajectories of 100 primaries photons generated when the applicator is a. only translated (50 mm and 30 mm along the-x and y-axes, respectively), b. only rotated (by 315 degrees around the-z axis), and c. both translated and rotated (displaced 50 mm along the-x axis and 30 mm along the y-axis, and rotated subsequently by 315 degrees around the-z axis).35

Figure 2-9. Visualization of the applicator position and orientation after rotation around the coordinate center 0,0,0 and translation to a coordinate point a, b, c37

Figure 2-10. The modelled INTRABEAM source probe and its coordinate system. .38	.38
Figure 2-11. The modeled INTRABEAM spherical applicator and its coordinate system. The x-axis defines the long axis of the applicator. The y and z-axes specify the transverse plane.39	39
Figure 2-12. Geometrical model of the INTRABEAM source and its spherical applicator.....39	39
Figure 2-13. The initial version of the developed GUI. A 3.5 cm spherical applicator positioned in a water phantom is visualized.47	47
Figure 2-14. The simulation setups. The modeled spherical applicator is placed within the tumor bed in the a. homogeneous patient geometry and b. heterogeneous patient geometry. The blue circle describes a cross-section of the 1 cm defined target volume.52	52
Figure 2-15. Visualizations of the 5 mm blood gap (red circle) a. surrounding the cavity and b. surrounding the surface of the spherical applicator. The blue circle represents the defined target volume.....53	53
Figure 3-1. Comparison of depth dose curves in patient homogeneous CT and in water phantom for the 3.5 cm spherical applicator.....57	57
Figure 3-2. Visualization of the path of the 100 primary photon particles that were generated by the algorithm, a. before correction, b after correction to the <i>SteppingAction</i> implemented.....58	58
Figure 3-3. The calculated central axis dose plane for the 3.5 spherical applicator before and after the correction applied in the <i>SteppingAction</i> class of the algorithm.59	59
Figure 3-4. The updated GUI of the INTRABEAM source model. The left panel of the GUI shows the added features associated with the geometry of the patient and the scoring functionality.60	60

Figure 3-5. Dose distributions in a. homogeneous patient geometry and b. heterogeneous patient geometry superimposed on a CT image of the corresponding slice ²³.....62

Figure 3-6. Dose profiles for the homogeneous and heterogeneous patient geometries. The dose profiles are obtained from the selected area shown in **Figure 3-5** ²³. A bone interface (rib) appears 20 cm from the applicator surface.....64

Figure 3-7. a. The dose points of the extracted target volume (left) and b. its central axis dose plane (right).65

Figure 3-8. a. The dose points of the left breast minus the target volume and b. dose distribution at the central axis.....65

Figure 3-9. DVHs in the patient geometry for 20 Gy prescribed at the applicator’s surface for a. the target volume and left breast, b. heart, left and right lungs. Calculations were conducted for the homogeneous CT (solid lines) and heterogenous CT (dotted lines) ²³.....67

Figure 3-10. Dose distributions in the patient geometry superimposed on the CT axial slice for simulations in the presence of a. 2 mm air gap and b. 5 mm air gap between the applicator surface and tumor bed.....69

Figure 3-11. Dose profiles a. without and with the presence of the 2 mm and 5 mm air gaps. b. The respective relative deviations. The dose profiles of each setup were extracted from the applicator surface.....71

Figure 3-12. DVHs in the patient geometry for a. the target volume and left breast and b. the other OARs for the simulations without the air gap (Ref) and with the air gaps of 2 mm and 5 mm (AG).73

Figure 3-13. Dose distributions in patient geometry overlaid in the CT axial image of a corresponding slice for the simulations with the 2 mm and 5 mm blood present between the applicator surface and tumor bed.....75

Figure 3-14. Comparisons of dose profiles a. without the presence of blood and in the presence of the 2 mm and 5 mm blood interfaces and b. their relative dose differences.....77

Figure 3-15. DVHs in the patient geometry for 20 Gy prescribed at the applicator’s surface for a. the target volume and the left breast and b. the other OARs. Simulations were performed for the reference setup (ref) and the error setups with the presence of the 2 mm and 5 mm blood interfaces (BI).79

Figure 3-16. Comparisons of the calculated dose uncertainty as a function of the number of primary history for the homogeneous and heterogeneous CTs.81

Figure 3-17. Comparisons of the calculated dose uncertainty as a function of the number of primary histories for the reference (without air gap) and the error setups (with the air gap).82

Figure 3-18. Comparisons of the calculated dose uncertainty as the function of the number of histories for the reference and the error setups with the 2 mm and 5 mm blood interfaces.....83

Figure 7-1. The 3D dose points of the defined OARs and their corresponding 2-D dose distributions of the associated dose slice for the a. left lung, b. heart, and c. right lung.115

LIST OF TABLES

Table 2-1. Data attributes, tags, and VRs used to build a patient geometry.....17

Table 2-2. Details of the mass density, electron density range, and elemental composition data of the materials/tissues used in the MC dose calculations ^{23,55,56}.
.....19

Table 3-1. The absorbed doses in the target volume and other OARs for the homogeneous and heterogeneous patient CT geometries ²³.68

Table 3-2. The absorbed dose deposited in the target volume and the other OARs for the simulations with and without the consideration of the air gap between the applicator and tumor bed.....74

Table 3-3. The absorbed doses in the target volume and the other OARs for the simulations with and without the presence of blood interface between the applicator surface and tumor bed.....80

1 INTRODUCTION

1.1 Treatments of breast cancer and the need for an accurate and reliable dose calculation algorithm for the treatment with the INTRABEAM device

Radiation delivery to the incised breast after breast conservation surgery (BCS) or lumpectomy is considered a viable alternative to radical mastectomy in the treatment of breast cancer patient ¹. A recommended approach for patients with early-stage breast cancer is whole breast radiation therapy (WBRT) with a boost to the tumor bed after the BCS because of the reduced local relapse rate and increased overall survival ². However, clinical trials and observational studies have shown that the majority of recurrences are localized close to the primary tumor site ^{3,4}. These data resulted in a growing interest in accelerated partial breast irradiation (APBI). APBI reduces the volume of the treated breast by confining the delivered doses to the target volume (tumor bed) and escalates the delivered doses by increasing the daily fraction dose of radiation ². Because it treats only a small part of the breast volume, potential lung and cardiac toxicities of the treatment radiation and overall treatment time are reduced compared to WBRT ⁵. Several APBI techniques are available, including linac-based intensity-modulated radiotherapy, multicatheter interstitial brachytherapy, balloon-based catheters, and intraoperative radiation therapy (IORT).

IORT is a technique to deliver a single high dose of radiation to macroscopic tumor foci or tumor bed during surgical tumor resection ⁶. Performing the technique at the time of surgery aims to prevent local recurrence by eliminating any residual tumor cells in the tumor bed ⁷. One of the most frequently used devices in the IORT technique is the INTRABEAM[®] system (Carl Zeiss Meditec AG, Jena, Germany) ^{8,9}. It is a mobile, miniature kilo-voltage radiotherapy device that produces a nearly spherical dose distribution similar to a localized, low-energy brachytherapy source ¹⁰. Currently, the INTRABEAM device has been used to treat breast cancer ¹¹, spinal metastases ^{12,13}, brain tumors ¹⁴, gastrointestinal tumors ¹⁵, head and neck tumors ¹⁶, non-melanoma skin cancer ¹⁷, and endometrial carcinoma ¹⁸. IORT with the INTRABEAM device has

several advantages, such as a single high dose delivery to the target volume with a rapid dose fall-off, ensuring maximum exposure to the tumor bed while sparing the nearby organs at risk (OARs) ^{10,19}, short treatment time, increased radiobiological effectiveness (RBE) ²⁰, and minimum shielding requirements. These advantages have led to the increased use of the INTRABEAM particularly for the APBI ²¹. Further description of the source is provided in the MATERIALS AND METHODS section.

One of the limitations associated with the practice of IORT with the INTRABEAM device is the lack of an image-based planning system ^{22,23}. Unlike other treatment modalities, 3D treatment planning for the INTRABEAM device has not been fully incorporated into the treatment processes due to the difficulties in installing functional in-room imaging in the operation room (OR) ⁸. These include the limited space of the OR, the size of the imaging devices, the additional time required to place the imaging device while preserving the sterile surgical setup, image artifacts caused by metallic surgical tools and table parts, and installation costs. As a result, the current planning and verification of plans for the INTRABEAM system is primarily based on measurements conducted in a simplified configuration consisting of an applicator and a water phantom rather than an image-based planning system ²⁴. However, this form of dosimetry limits the accuracy of the treatment for various reasons.

Firstly, the experimental methods of dosimetry of the INTRABEAM treatment planning are highly dependent on the dosimetry protocols utilized ²⁵. Zeiss provides two dose-rate calculation protocols, which are the Calibration V4.0 protocol and the TARGIT protocol. The Calibration V4.0 protocol represents the physical dose surrounding the INTRABEAM source, while the TARGIT protocol follows the dose rate used in the TARGIT (**TAR**Geted **Intraoperative radioTherapy**) clinical trial ²⁵. The dose rate discrepancies between both protocols are 14% to 30%, with the largest shift found for the smallest applicators ²⁵. The experimental methods of dosimetry are also limited, time-consuming, and challenging. This is because the measurements are conducted with ionization chambers, optically stimulated luminescence dosimeters, and radiochromic films that only provide a limited amount of data ²⁴. From a technical

perspective, detector placement in a volume of interest demands high geometric precision. A slight deviation of the detector positioning might cause a significant variation in the detector readings due to the steep dose fall-off of the INTRABEAM source ^{19,26}. Some in vivo studies have indicated an average dose difference of approximately 20% between the intended and the actual dose at the surface of the applicator ^{26,27}. In some measurements, the difference can be as high as 64% ²⁷. Therefore, it is crucial to use a 3D treatment planning system (TPS) to ensure a more reliable treatment planning option for cancer treatment with the INTRABEAM device.

Secondly, tissue heterogeneity influences the achieved absorbed dose distributions ²⁸. For low-energy X-ray sources, patient tissues could not be considered analog to water ^{22,28}. The presumption that the patient is composed of only water and the inconsideration of patient tissue heterogeneities means that the actual doses absorbed in the target volume and organs at risk, such as lung, heart, and chest wall, remain unknown ²³. Accurate and precise knowledge of the absorbed dose delivered to these critical organs is crucial to achieve optimal treatment outcomes and to have meaningful comparisons of the patient outcomes with other treatment modalities ²⁹.

Another limitation of relying treatment planning solely on a simplified measurement configuration is the forsaking of geometric errors and their effects on dose distributions. A water phantom indeed provides the ideal scenario, a perfectly matched adherence between the applicator surface and the treated phantom volume as water follows whatever shape of the applicator inserted. In fact, achieving perfect applicator conformance to the tumor bed during the treatment procedure is a challenging task. The imperfect applicator-tumor bed conformity might be caused by geometric errors. Geometric errors in IORT with the INTRABEAM device attributed to misalignments of the applicator in the tumor bed because of the irregular surface of the surgical cavity ³⁰, undocumented size and shape of the target volume and its position in the beam ⁸, or incorrect applicator size used in the treatment ³⁰. These errors might cause the formation of additional interfaces filled with air or blood fluid between the applicator and the tumor bed. These interfaces might occur in breast IORT, especially if the

treated volume was too thick to be fully visualized by the surgeon and radiation oncologist⁸. Even though extra precautions were performed to exclude fluid from the cavity and to ensure no cavity distortion around the applicator sphere: This included complete hemostasis and the use of purse-string suture in such a way that the breast tissues were tightly attached to the spherical applicator³¹, air gaps or fluid interfaces between the applicator and tumor bed might still appear and affect the absorbed doses delivered to the tumor bed and the other OARs.

Chiavassa et al. reported the existence of air interface in the post-operative CT scans of a cadaver's prostate bed following a prostatectomy procedure³². The interfaces were observed in the vicinity of both the applicator stem and the spherical component of the applicator. Similarly, a study of breast IORT incorporating image guidance and high-dose-rate (HDR) brachytherapy using a multilumen balloon applicator placed into a lumpectomy bed done by *Trifiletti et al.* revealed that according to the initial intraoperative CT scans in 7 out of 29 patients have poor applicator-tissue conformity because of the large air cavities and gaps present between the inserted balloon applicator and tumor bed³³. Additionally, *Trifiletti et al.* reported that even after performing measures to improve the conformity (repetitive vacuum suctioning of air bubble through the applicator port, performing adjacent tissue transfer, or applying external pressure to the breast), the gap or interface between the applicator and the tumor bed remained³³. Thus, the uncertainty of the applicator position within the target tissue during an IORT procedure with the INTRABEAM device might introduce dosimetric inaccuracy and contribute to the dose discrepancy from the intended dose delivered. However, should geometric errors occur, it is necessary to understand the dosimetric implications. A comprehensive failure and effect analysis was therefore proposed for a better understanding and quantification of the dosimetric errors.

1.2 Available TPSs and the developing dose calculation algorithm

Radiance (GMV SA, Spain) is the first available commercial TPS for IORT with the INTRABEAM device. The system has been developed to perform dose calculations for

various clinical situations³⁴. The system considers tissue heterogeneities and employs a hybrid Monte Carlo algorithm that allows users to perform fast dose calculations³⁵. However, the accuracy of the system is limited as the anisotropy of the source^{36–38} was not considered in the dose computation³⁹. The consideration of the INTRABEAM source as an isotropic source resulted in dose discrepancies of approximately 14% in the region close to the applicator shank. This discrepancy can contribute to a dose increase of up to 3 Gy in a breast IORT treatment, in which 20 Gy is usually prescribed at the surface of the applicator³⁹. The system is also not yet widely adopted into clinical practice³⁴. A Monte Carlo study of the dose distribution in a patient from a treatment using the INTRABEAM device will help clinicians better understand the delivered dose to the surrounding tissues and aid decision-making.

A Monte Carlo source model (algorithm) for dose calculation was previously developed in-house for the INTRABEAM source⁴⁰. The algorithm was implemented in Geant4, a freely available open-source toolkit for simulating radiation interaction with matter and a powerful Monte Carlo tool in the modelization of accurate physics models and experimental setups, particularly for medical physics applications⁴¹. The source model considers all available knowledge in the source-modeling process, including geometric data of the source, data from experiments and simulations, and mathematical knowledge. It also fulfills the requirements of a clinical dose calculation algorithm with a high accuracy⁴⁰. Thus, the algorithm can be used to perform virtual quality assurance tests as well as treatment planning and to investigate likely errors that would have been otherwise difficult or impossible to evaluate by experimental methods²³. Further description of the algorithm is provided in the MATERIALS AND METHODS section.

Despite the superiority of the source model, as previously stated, it was unfeasible to perform simulations and dose calculations of a patient with the algorithm. The initial version of the algorithm was limited to dose calculation in a homogenous medium. To calculate dose distributions of a patient, the algorithm should be able to handle dose calculation in a heterogeneous medium involving various material/tissue types.

1.3 Aims and scopes of the work

This work aims to extend the algorithm for dose calculation in heterogeneous media. This will make it possible to accurately calculate the absorbed doses in the target volume and organs at risk (OARs) of the heterogeneous patient.

Estimating dose distributions within a patient from a breast IORT treatment with the INTRABEAM device is complex for some reasons mentioned above. To solve this, an interface to import a patient's CT data is included and integrated into the source model. The interface reads the original CT data, converts them, and saves them in a format compatible with the Geant4 format. Some parts of the original codes are modified to include the interface. All the converted patient CT data are subsequently used by the source model to build or reconstruct a 3D patient geometry. A more advanced and sophisticated dose scoring method taking into account patient tissue heterogeneities is also developed. A feature is established to enable the adjustment of the applicator position in the cavity/tumor bed. Having such a capability is essential in this work, as the applicator should be adjusted to fit the surgical cavity/tumor bed before the radiation delivery. Additionally, some features are added in the graphical user interface (GUI) to visualize the treatment setup. The GUI helps to visualize and assess the position of the applicator within the tumor bed before the simulation is performed.

Simulations are conducted after adjusting the applicator position inside the tumor bed located within the left breast. The absorbed dose distributions within the target volume and the OARs of the patient are after that determined. The obtained dose distributions are then evaluated and compared with the dose distributions obtained from the water phantom as the current standard practice in the breast IORT treatment with the INTRABEAM. Finally, the effect of geometric errors on dose distributions and the absorbed doses deposited in the target volume and the OARs are investigated. The geometric errors are implemented in the simulated treatment setup by introducing an air gap or a blood pooling between the surface of the applicator and the tumor bed. The impact of geometric errors is evaluated by comparing the dose profiles and DVHs with those obtained from a reference setup.

2 MATERIALS AND METHODS

2.1 The INTRABEAM source and spherical applicators

The INTRABEAM device is a mobile miniature of an X-ray generator operating at a generating potential of 50 kV. The source consists of a cathode gun and a target tube. The cathode gun contains the filament that emits electrons when heated, the anode serves as an electrons accelerator, and the beam deflector composes of two sets of X-Y deflection coils to control beam position at the X-ray target and to ensure a symmetric and fairly isotropic photon output ¹⁰. The target tube is a drift tube (probe) attached to the cathode gun and comprises a narrow cylinder and a hemispherical cap containing a gold target at one end. The cylinder has 10 cm long with inner and outer radii of 1.5 mm and 1.6 mm, respectively. The gold target has a thickness of approximately 1 μm and is coated with NiO, Ni, and CrN for biocompatibility and physical durability ⁴⁰. **Figure 2-1** shows the INTRABEAM X-ray source and its spherical applicators.

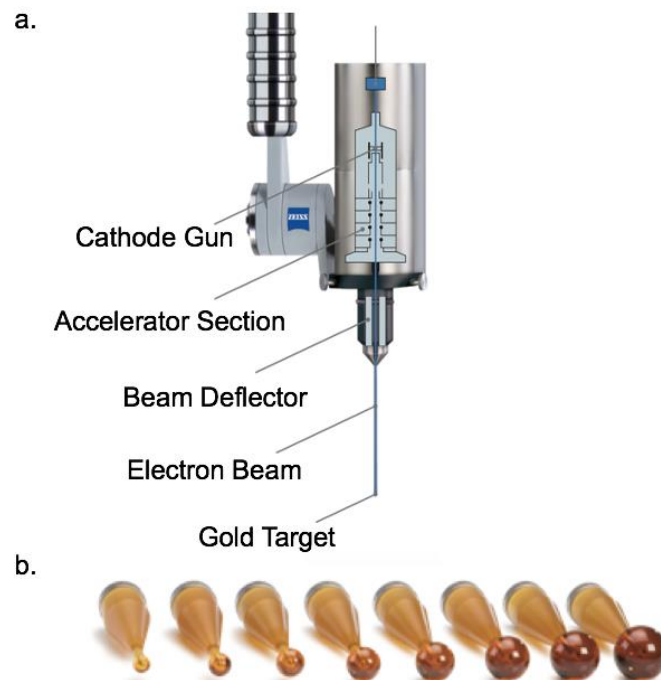


Figure 2-1. a. The INTRABEAM XRS and its b. spherical applicators ⁴².

X-ray production in the INTRABEAM source begins with the emission of electrons from the cathode gun. The accelerator section of the source then accelerates these electrons to a maximum energy of 50 keV. With the help of the beam deflector, the electrons are directed down the narrow probe to strike a thin concave gold target at the hemispherical end of the probe. When the electron beam collides with the gold target, a portion of the energy generated by the interaction of the electrons with the target material is transformed into radiation. This x-ray radiation is in the form of characteristic and bremsstrahlung radiations emitted in a nearly spherical distribution centered at the tip of the probe ⁷.

The breast IORT treatment with the INTRABEAM device is performed by placing the source in a fixed position within a spherical applicator made from polyetherimide (PEI). The applicator has diameters ranging from 15 mm to 50 mm with 5 mm step increments, allowing treatment of different sizes of the tumor cavity. Beam hardening, lower energy photons removal from the x-ray beam, is through an aluminum layer insertion into the smaller applicators (diameter less than or equal to 30 mm). For larger applicators, the applicator thickness suffices for the intended purpose. Beam hardening is required to produce an isotropic photon beam at the applicator surface. Readers are referred to literature ^{10,36,43,44} for detailed descriptions of the source and the applicators.

2.2 Overview of breast IORT treatment with the INTRABEAM device

The IORT treatment of an early-stage breast cancer patient with the INTRABEAM device, in general, begins with the acquisition of pre-operative mammography, ultrasound, and in selected cases also MRI or CT scans of the patient. After the tumor has been identified, it is surgically removed from the diseased breast. A spherical applicator that fits the tumor bed is selected and attached to the X-ray source (XRS). The whole arrangement is afterward positioned into the surgical cavity. A prescribed dose, usually 20 Gy at the applicator surface following the TARGIT protocol, is delivered to the target volume with a typical treatment duration of 20-50 min ²³. The

treatment time depends on the size of the applicator used. The larger the size of the applicator, the longer the treatment time provided to the patient. Efforts are made to ensure good contact between the applicator surface and tissues in the tumor bed and to exclude air or fluid from the cavity for optimal dose delivery to the tumor bed. **Figure 2-2** illustrates the treatment procedures.

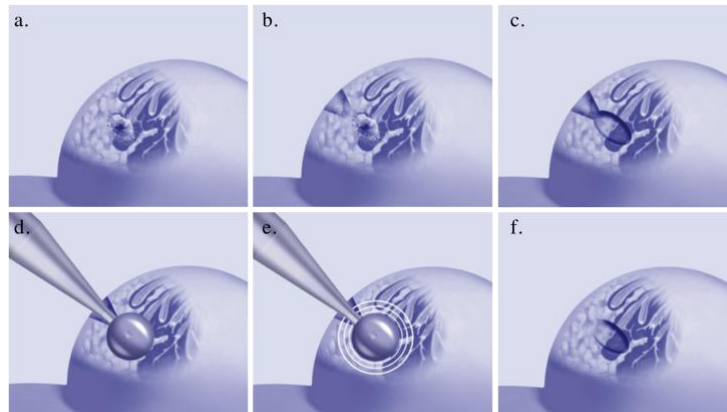


Figure 2-2. IORT procedure during a BCS. a. determination of the tumor position, b. creating access (incision) to the tumor, c. surgical removal of the tumor, d. positioning an appropriate applicator in the tumor bed, e. the tumor bed irradiation, and f. applicator removal after 20-50 minutes of irradiation and incision closing ⁴⁵.

2.3 Overview of the Geant4 Monte Carlo Toolkit

The **GEometry And Tracking 4** (GEANT4) is a Monte Carlo (MC) simulation toolkit used to simulate and track the passage of particles through matter. The GEANT4 code is written using the C++ programming language and has been developed extensively since its first release in 1998. Nowadays, Geant4 is a widely recognized open-source and freely available MC code that has been used in multiple scientific fields from high energy physics (HEP) to space science and medical physics ^{46,47}. In the field of medical physics, Geant4 offers the ability to study new strategies and methodologies in diagnostic and therapy, evaluate available techniques, and plan therapy treatments that demand accurate dose mapping ⁴⁶.

The Geant4 toolkit is composed of tools that provide all aspects of the simulation process. The toolkit has comprehensive detector and physics modeling capabilities that allow users to model experimental setups based on geometry and materials and define the particle involved and their physics interactions. It has the ability to track the particle in matter and describe the detector response. It also provides interfaces that enable users to interact with the applications, store the results in analysis objects, and visualize the geometry using visualization drivers and graphical user interface ⁴⁷.

Figure 2-3 illustrates a diagram of the Geant4 kernel consisting of different class categories. The higher categories used the bottom categories as the foundation of the toolkit.

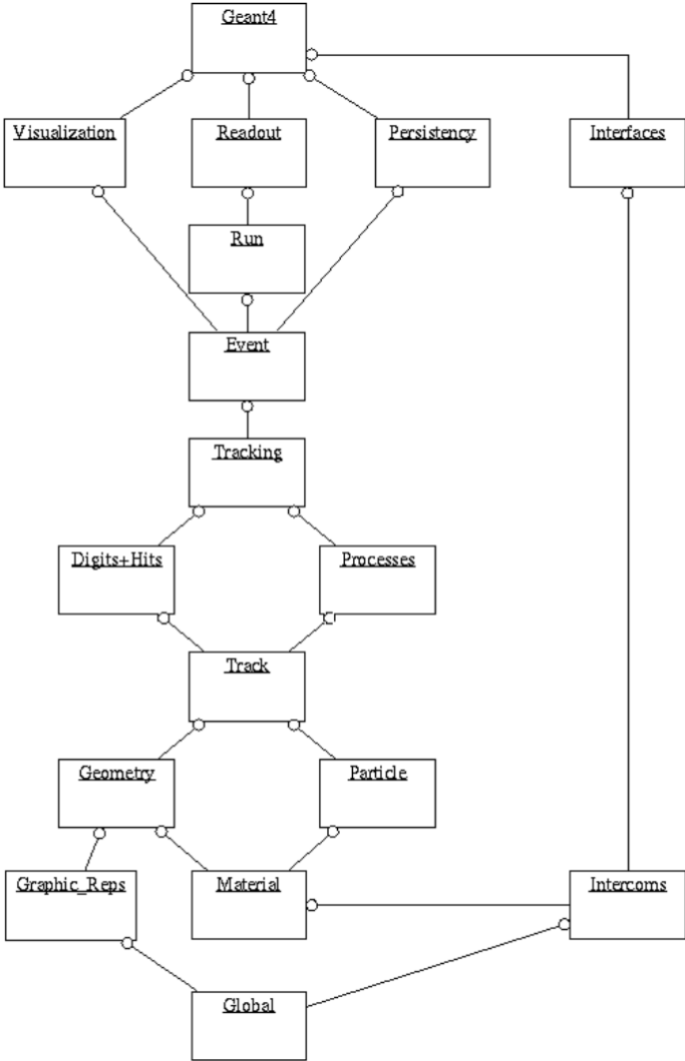


Figure 2-3. The Geant4 kernel and its functionality ⁴⁷.

The *Global* category covers the system units, constants, numerics, and random number handling ⁴⁸. The *Materials* and *Particles* categories describe the physical properties of particles and materials for simulating the particle-matter interactions. The *Geometry* module gives the ability to build geometries. The *Track* category contains classes for track and steps used by the *Processes* category. The *Process* category contains implementations of models of physical interactions. This class describes the interactions between particle and matter allowed during the simulation (the photoelectric effect, the Compton effect, pair production, Rayleigh scattering, etc.). The *tracking* category invoking all processes manages the contribution of these processes to the evolution of a track's state and provides information in sensitive volumes for hits and digitation. The *Event* category organizes events in terms of their tracks. The *Run* category manages collections of events (runs). The events share the detector implementation, physics conditions, and primary generation in a single run. A *Readout* category allows the handling of a pile-up. Finally, capabilities that use all these categories and connect to facilities outside the toolkit through abstract interfaces provide visualization, persistency, and user interface capabilities. Readers are referred to literatures ^{46,47} for more in-depth and complete descriptions of the toolkit.

Of all class categories of the Geant4 toolkit mentioned above, users must provide the *Materials*, *Particles*, and *Geometry* classes to perform a simulation. *Global*, *Track*, *Tracking*, *Event*, *Run*, and *Readout* classes are also required to conduct a simulation, but modifications to these classes are not compulsory. Other class categories such as *Intercoms*, *Graphic-Reps*, *Digits and Hits*, *Interfaces*, *Visualization*, and *Persistency* are not required. However, they provide beneficial information to users through the capabilities to visualize geometrical structures and data storage.

The following sub-sections describe in more detail the main features of the most important packages of Geant4 used, which are the subject of the development of the algorithm.

2.3.1 Geometry and Material classes

The *Geometry* class facilitates the users to describe the geometrical structure of a detector. This class also allows the system to propagate particles efficiently through it. A complex geometry is built by assigning every component of the detectors to a volume. Each volume is given shape and size, material, and position. The basic shape is defined by the concept of solid volume. Simple solids, for instance, rectilinear boxes, trapezoids, spherical and cylindrical sections, or shells can be built using the *Constructed Solid Geometry* class (CSG) of the toolkit. Another way to create solids is by combining simple solids using boolean operations (unions, intersections, and subtractions).

The Geant4 *Materials* class is used to describe the material description of a volume. The described material is either a single element or a mixture of elements ⁴⁹. A detector volume is defined using the concepts of logical and physical volumes. The logical volume represents the detector element of a particular shape. Meanwhile, the physical volume portrays the spatial position and orientation of the detector volumes. The physical volume represents the spatial positioning of the logical volume with respect to an enclosing mother volume. All the modeled volumes are positioned within the mother volume in a hierarchical manner ⁵⁰. The mother volume coordinate system is used to describe the position of the daughter volume. At the top of the hierarchy volume is the World volume where all particle interactions occur. Outside the World no particle interactions are considered and no particle is tracked. The physical volume must be defined starting from the logical volume. A physical volume can be placed once in its mother volume or through parameterization placements that allow repetitive placements of the same logical volume many times. All the modeled volumes are declared in the source file "*DetectorConstruction*". The material description is also included in the "*DetectorConstruction*" and defined for all detector components.

2.3.2 Primary particle generation

The primary generator (*PrimaryGeneratorAction* class) is a member of the *Run* category. Unlike other members of this category, the *PrimaryGeneratorAction* class is mandatory to provide. In general, the *PrimaryGeneratorAction* class is a module to control all parameters required to generate particles, such as particle types, initial energy, and initial position and orientation of the primary particles.

Particle transport in Geant4 simulation initiates by generating primary particles called primaries. The primaries are generated either using a particle gun or a general particle source. The Geant4 toolkit has several pre-built generators, including the *G4ParticleGun*, *G4GeneralParticleSource*, *G4SingleParticleSource*, and *G4HEPEvtInterface*. Readers are referred to Geant4 documentation available at the Geant4 website for a detailed description of the primary generator class of the toolkit. The primary particles in this work are defined using the *G4ParticleGun* class as it is suitable and adequate to describe the primary particle source of the INTRABEAM system. The properties of the primaries, such as particle type, kinematics, etc. must also be provided, and a source file named “*PrimaryGeneratorAction*” specifies all the parameters needed to generate the primaries.

2.3.3 Stepping Action

The stepping action (*SteppingAction* class) is also a member of the *Run* category. Although this class is essential to run a simulation, it's not mandatory to modify this class. However, a few lines of code are needed to extract useful information about a particle (such as energy deposition, kinetic energy, and position). Given geometry, physics, and primary track generation, information about a particle when it travels through matter or tissue can be retrieved. To retrieve the valuable information in Geant4, the users can utilize either *user hooks* (*G4UserTrackingAction*, *G4UserSteppingAction*, etc.) or *Geant4 scoring functionality*. A detailed description of the techniques goes beyond the scope of this thesis. Readers are referred to Geant4

documentation available at the Geant4 website for a more thorough comprehension of the techniques. As for this work, particle scoring is conducted using the stepping action approach as it is straightforward, flexible, and gives full access to almost all information.

2.4 The Geant4 Monte Carlo dose calculation algorithm

A previously developed in-house MC source model (algorithm) was adapted for this work^{24,40}. The algorithm was implemented in version geant4.9.4.p02 of the toolkit and has been successfully tested in version geant4.10.03.p03. In general, the adapted source model provided all requirements needed to run a simulation, such as the geometry of the source, applicators, and phantom, particle types, position, and energy, and the appropriate physical processes allowed during the simulation. In this work, the initial model was adapted with modifications to the initial conditions of the primary particles and applicator position.

The INTRABEAM source model consists of two main parts, which are the static machine-specific geometry and the dynamic phantom-specific geometry²⁴. The static-machine geometry depicts the XRS and is applicator and phantom-independent. The dynamic phantom-specific geometry is the description of the phantom/patient, as well as the applicator. Particle interactions in the static part are pre-computed once. The properties of the photons (such as the particle type, direction of travel, and initial energy) are collected in a virtual space called a phase space file (PSF). Repetitive simulation in the static part was overcome by modeling each photon characteristic in the PSF using mathematical functions. The use of mathematical functions to generate photons on a reference surface is known as a virtual source model (VSM). The characteristics of the generated photons from the VSM are similar to those in the PSF. The generated photons can be used subsequently to start a simulation in the dynamic part of the source model.

The *Physicslist*, which specifies the interaction types a primary particle can undergo during the simulation was taken from the Geant4 's *Brachytherapy* example. All photon interactions (Rayleigh scattering, photoelectric effect, Compton scattering, etc.) were considered using the Geant4 standard electromagnetics physics package and the Livermore electromagnetics models for boson and lepton processes. The *defaultCutValue*, the production threshold of the secondary particles along the track of the primary particles, was set to 0.01 mm. Below the threshold, no secondary particles were produced.

As the phantom geometry used in this work is replaced with the patient geometry, new algorithms associated with the patient geometry were added. Some parts of the existing algorithms were also modified to be adaptable to the geometry replacement and the treatment conditions implemented into the simulation setups. Some of the added features, as previously mentioned, are the interface to import the patient CT data used by the source model to build the patient geometry, algorithms for calculating the absorbed dose considering the patient tissue materials, and algorithms for adjusting the applicator position. The modified algorithms include the algorithm for the *DetectorConstruction* such that it can read and build the patient geometry from the imported patient data from the interface, the algorithm to describe the initial conditions for the primary particles (*PrimaryGeneratorAction*), and the algorithm for the initial conditions for the *SteppingAction* (*SteppingAction*) related to the change of the applicator position and orientation.

2.5 Modelling the treatment geometries

The absorbed dose distribution within the patient was determined by simulating photon transport and its interactions within the patient geometry. The INTRABEAM source, spherical applicator, surgical cavity, and patient geometries were therefore modeled. The geometries of the source and applicator were adapted from the previous version of the source model and were modeled using the CSG class. The patient geometry was modeled using a set of anonymized pre-operative CT scans of a breast cancer

patient imported using a DICOM interface. The surgical cavity was modeled using information from the imported pre-operative patient CT files and the employed applicator.

2.5.1 DICOM interface and the reconstruction of patient geometry

Geant4 accommodates means of patient data import for medical purposes⁵¹. Patient-specific anatomy to be imported is primarily in digital imaging and communication in medicine (DICOM) formatted computed tomography (CT) datasets. The datasets contain information on the anatomy and other supplementary information to obtain the density distribution of the organs and tissues. The resampled CT data were imported into the source model using a DICOM interface integrated into the source model. Complex patient anatomy involving geometries and tissue heterogeneities is modeled by incorporating specific material properties such as material composition, electron density, and mass density data⁵². The developed DICOM interface is mainly based on the DICOM extended medical example in the Geant4 package.

A DICOM file consists of a header and image datasets. The header stores clinical and technical information of the given image, while the image datasets contain pixel-intensity data⁵³. An attribute has a particular numeric code series called a DICOM tag identifying the attribute and a DICOM value representation (VR) portraying the data type and format of the attribute value. The attributes, tags, and VRs used by the DICOM interface are presented in **Table 2-1**.

Table 2-1. Data attributes, tags, and VRs used to build a patient geometry.

Attribute	Tag	VR
Rows	(0028,0010)	US
Bits Allocated	(0028,0100)	US
Smallest Image Pixel Value	(0028,0106)	US or SS
Largest Image Pixel Value	(0028,0107)	US or SS
Rescale Slope	(0028,1053)	DS
Rescale Intercept	(0028,1052)	DS
Pixel Presentation	(0008,9205)	CS
Modality	(0008,0060)	CS
Manufacturer	(0008,0070)	LO
Institution Address	(0008,0081)	ST
Institution Name	(0008,0080)	LO
Manufacturer's Model Name	(0008,1090)	LO
Device Serial Number	(0018,1000)	LO
Pixel Spacing	(0028,0030)	DS
Slice Thickness	(0018,0050)	DS
Slice Location	(0020,1041)	DS
Transfer Syntax UID	(0002,0010)	UI
Pixel Data	(7FE0,0010)	OB or OW

US: Unsigned Short; SS: Signed Short; DS: Decimal String, CS: Code String; LO: Long String, ST: Short Text; UI: Unique Identifier; OB: Other Byte String, OW: Other word string

All the attributes except the pixel data belong to the header. The pixel data is a unique attribute representing image datasets. The patient CT images can be reconstructed using these image datasets and information from the header. DICOM interface extracts all relevant information of these attributes using their corresponding tags. Algorithm to read and retrieve the information needed was taken from the DICOM extended medical example in the Geant4 package. Readers are referred to the Geant4 website for detail description of the DICOM medical example in the Geant4 package.

Modeling a patient geometry in Geant4 requires detailed material/tissue characteristics data of the patient. The characteristic data is derived using a calibration curve established from CT images of a tissue characterization phantom⁵⁴. The calibration curve is used to convert the CT number in each voxel of the patient's CT image into density. The RMI 467 (Gammex, Middleton, WI, USA) electron density phantom is used to create the calibration curve for this work. The RMI 467 consists of 16 inlays of tissue-mimicking materials with various density values. The Brilliance Big Bore, Philips Healthcare scanner at an anode-cathode potential of 120 kV and exposure time product of 150 mAs, was used to scan the phantom. A MATLAB program was developed to extract the information from the phantom scan. The average CT value of each phantom material was obtained by drawing a circular ROI of diameter 1.2 cm on each inlay of the central slice of the phantom. A calibration curve was established by interpolating the obtained mean pixel value and the electron density data points. **Figure 2-4** depicts the RMI 467 tissue characterization phantom and the resulting calibration curve obtained from the RMI 467. Since air is not provided as one of the calibration phantom materials, an inlay is removed to represent the air.

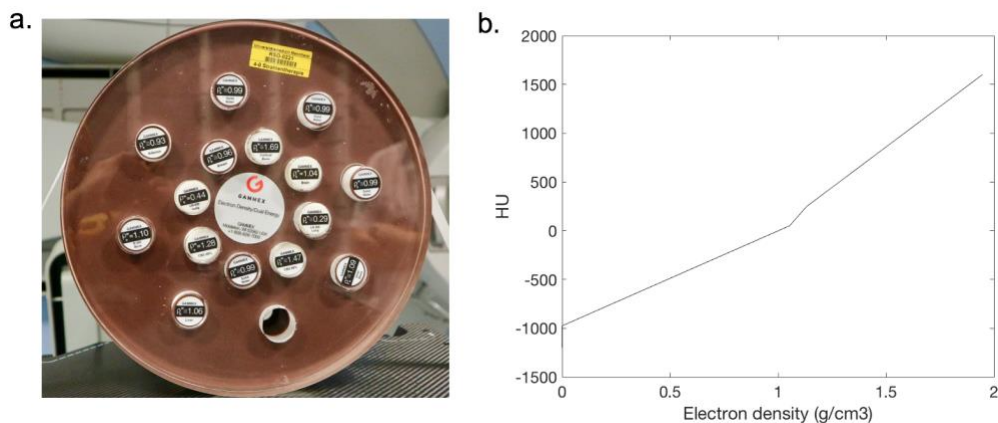


Figure 2-4. a. Tissue characterization phantom, Gammex-RMI 467. b. The calibration curve relates the HUs and electron density.

The calibration curve is included in the INTRABEAM source model as an input file for the *DetectorConstruction*. The calibration curve is saved in a file named *CT2density.dat*. The *DetectorConstruction* converts the mean pixel values (in HUs) to

densities based on the data in the *CT2density.dat* file. The obtained densities were then grouped into several intervals according to the electron density information⁵⁵. Each interval defines a material/tissue indexed with a unique number. Ten materials were built using the elemental composition data and subsequently assigned to a density value based on the mass density data of the corresponding material summarized in **Table 2-2**. Since the density data for air is not available from the calibration phantom, the data was taken from the *Medical Extended* example included in the Geant4 package.

Table 2-2. Details of the mass density, electron density range, and elemental composition data of the materials/tissues used in the MC dose calculations^{23,55,56}.

Material/ tissue	Mass Density [Electron Density range] (g/cm ³)	Composition (%)				
		H	C	N	O	Others
Air	0.00129 [0.000 - 0.207]	-	-	70.0	30.0	-
Lungs (inhale)	0.260 (0.207 - 0.290)	10.3	10.5	3.1	74.9	0.2 Na, 0.2 P, 0.3 S, 0.3 Cl, 0.2 K
Lungs (exhale)	0.508 [0.290 - 0.440]	10.3	10.5	3.1	74.9	0.2 Na, 0.2 P, 0.3 S, 0.3 Cl, 0.2 K
Adipose	0.950 [0.440 - 0.930]	11.4	59.8	0.7	27.8	0.1 Na, 0.1 S, 0.1 Cl
Breast	1.020 [0.930 - 0.960]	10.6	33.2	3.0	52.7	0.1 Na, 0.1 P, 0.2 S, 0.1 Cl
Water	1.000 [0.960 - 0.990]	11.2	-	-	88.8	-
Muscle	1.050 [0.990 - 1.050]	10.2	14.3	3.4	71.0	0.1 Na, 0.2 P, 0.3 S, 0.1 Cl, 0.4 K
Liver	1.060 [1.050 - 1.060]	10.2	13.9	3.0	71.6	0.2 Na, 0.3 P, 0.3 S, 0.2 Cl, 0.3 K
Rib	1.410 [1.060 - 1.280]	6.4	26.3	3.9	43.6	0.1 Na, 0.1 Mg, 6.0 P, 0.3 S, 0.1 Cl, 0.1 K, 13.1 Ca
Dense bone	1.920 [1.280 - 1.690]	3.4	15.5	4.2	43.5	0.1 Na, 0.2 Mg, 10.3 P, 0.3 S, 22.5 Ca

The obtained densities and materials data, along with other relevant information extracted from the header of every DICOM file (such as the number of columns, numbers of rows, pixel spacing, and slice thickness), were saved as a set of text files and a set of binary files with the extension of .g4dcm and .g4dcmb per the Geant4 file extension convention. The .g4dcm and the .g4dcmb files are the converted DICOM files compatible with the Geant4 application and can be used to build the patient geometry. Unlike a DICOM file that contains a header (organized as a constant and standardized series of tags) and image datasets (stored as a long series of 0s and 1s) packed into a single file, the structures of the .g4dcm and .g4dcmb files are simple without series of tag used. Although the .g4dcmb file is also a binary file with a header, the amount of data stored is not as much as in the DICOM file's header. Both the .g4dcm and the .g4dcmb files save the information according to the following order/structure,

1. number of materials,
2. each material index and its name,
3. number of voxels and their minimum and maximum extension in X, Y, and Z,
4. the $nVoxelX * nVoxelY * nVoxelZ$ material indices (one per voxel),
5. the $nVoxelX * nVoxelY * nVoxelZ$ material densities (one per voxel).

Readers are referred to APPENDIX (section 7.1 page 108) for the detailed structure of the files.

The converted data contained in the .g4dcm were then read and utilized by the *DetectorConstruction* of the source model to reconstruct the patient geometry. As previously mentioned, the imported patient CT data reading is mostly based on the DICOM extended example providing in the Geant4 package. However, minor modification were performed especially to integrate the codes into the algorithm. **Figure 2-5** illustrates the reconstructed geometry. The codes are available in APPENDIX (section 7.2 page 109).

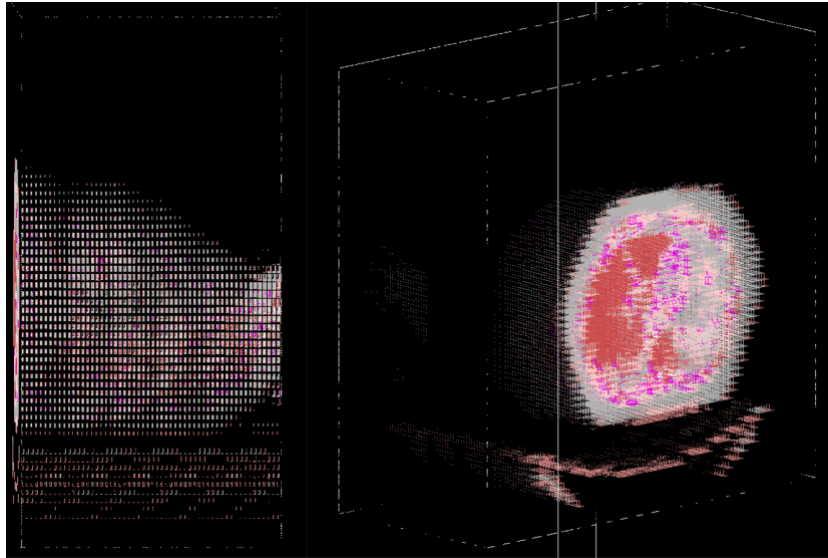


Figure 2-5. The 3D visualization of the reconstructed patient geometry. For the visualization purpose, the initial resolution is reduced by factor of 8 in the x and y axes.

2.5.2 Slice selection criteria

The shape of the cavity depends on the voxel dimension of the DICOM images. Because the unmodified DICOM image has dimensions of 1.1719 mm × 1.1719 mm × 5 mm (current protocol for EBRT in our center for breast CT) where the slice thickness is larger than the pixel spacing, the created cavity volume in returns is asymmetrical. In other words, the shape and dimension of the cavity are wider in the z-direction. The CT voxel dimension was then resampled to 1 mm × 1 mm × 1 mm to ensure the symmetrical shape of the resulted cavity. The voxel resampling was performed in MATLAB using linear interpolation.

The linear interpolation of the CT data was conducted using information from the original CT files. The information needed is pixel data, the number of voxels (in x, y, and z), pixel spacing, and slice thickness. The pixel data were extracted from the image datasets of the original CT, while the number of voxels, pixel spacing, and slice thickness were withdrawn from the header of the CT file. The result is a new image dataset with the defined voxel size. Since the voxel was resized, the *SliceLocation* and the *ImagePositionPatient* were also modified following the new voxel size. The

structure of the header file of the original CT was then copied. The modified data and the data obtained from the 3D interpolation were inserted into this structure. The unmodified data of the header file were kept and also inserted into the copied structure. A set of new CT files were then created using this new structure. As the resolution changed, the resulting CT files were 386 files with total voxels of $599 \times 599 \times 386$ (the number of CT files before resizing is 72 files). On the other hand, the simulation accuracy represented by the simulation uncertainty depends on the number of particle histories used in the simulation. Particle histories are the tracking of a primary photon and the underwent interactions until the photon loses its energy. To achieve high accuracy, a simulation involving millions of voxels demands a more significant number of histories. The larger the number of histories, the more accurate the calculation²⁴. However, simulations with these scenarios are computationally expensive and time-consuming⁵⁷.

To minimize these constraints, we used only slices in which the cavity, a target volume, and the investigated organs at risk are included. The target volume is defined as a microscopically tumor-free margin of 1 cm around the resected tumor surrounding the applicator⁵⁸. The investigated OARs are the left breast minus the target volume, lungs, and heart. For this purpose, slice selections were made based on organ outlines determined using the DICOM-RT structure data. Based on these outlines, a total of 233 CT files were used in the simulations. Since we were interested only in the target volume and the OARs, the voxel size was further reduced by cropping each CT file with voxel size $599 \times 599 \times 233$ to become $300 \times 300 \times 233$. The cropping was also conducted in MATLAB and applied to the voxels on the x and y planes. **Figure 2-6** presents the resulting CT image of a corresponding slice. All the performed simulations were conducted using the cropped CT files.

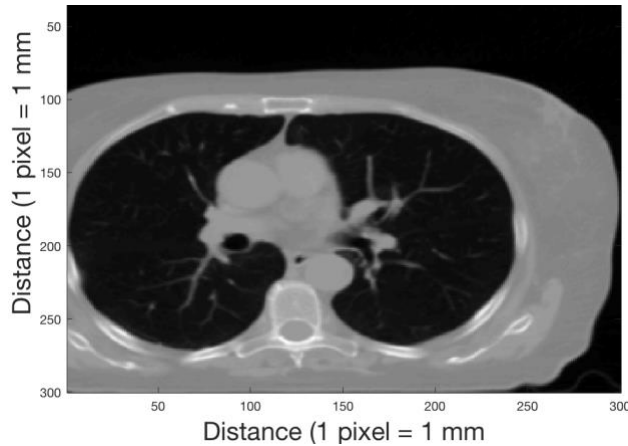


Figure 2-6. A cropped CT image of a corresponding slice. The included OARs are the left breast (without the target volume), heart and both lungs.

2.5.3 Volume overlapping and the cavity

All simulations in this work were performed with the source and applicator positioned in the virtual cavity. Not only is the positioning done to mimic the treatment conditions, but it is also accomplished to avoid volume overlapping between the patient geometry and the applicator. The overlapping refers to the condition where the volumes either protrude from the mother volume or intersect themselves⁵⁹. Volume overlapping is a well-known issue in Geant4⁵⁰ and might affect the simulation results. However, the effect on dose distribution in a voxelized geometry is unknown. Thus, we assessed the impact by performing the simulations in a homogenous-voxelized patient geometry with and without the cavity included in the simulations. The obtained results were also compared to the results from the simulation performed in a simple water phantom as a reference. The comparison is relevant because all simulations conducted with the initial version of the algorithm incorporate cavity²⁴. The cavity was created by subtracting the cavity volume from a simple water phantom geometry considered a box. Unlike the geometry of the water phantom which consists of only a simple box, the homogeneous patient geometry consists of millions of voxels. The cavity is created by replacing the materials of some considered patient voxels with air and subtracting the phantom container. A phantom container is a volume that holds each voxel of the

patient geometry. The subtraction of the cavity from the phantom container was also based on the geometric data of the applicator.

The idea to create the cavity is based on the *DicomIntersectVolume* included in the DICOM extended medical example. The *DicomIntersectVolume* demonstrates that it is possible to create a partial phantom volume that is the intersection of a phantom with a volume. We can also consider the cavity as a partial volume that is the subtraction, rather than the intersection, of the patient volume with the spherical applicator. For this purpose, the geometric data of the 3.5 spherical applicator, particularly the shape and size of its outer part, are used as a boundary to subtract the patient volume. Should the subtract volume (the cavity) have the same shape and size as the 3.5 spherical applicator, the adherence between the applicator surface and the created cavity (the tumor bed) can be ensured. The following implemented code describes how the outer part of the 3.5 cm spherical applicator is built from the sphere, tube, and cone that form the 3D shape of the cavity.

Code 1: Geant4 code to create the outer part of the 3.5 cm spherical applicator

```
//build solid for creating cavity for spherical applicator of 3.5 cm in diameter
G4UnionSolid* ZeissCavity::buildCavity235()
{
    // Shape to be created
    G4ThreeVector pos1 = G4ThreeVector(0 *mm, 0 *mm, 0 *mm);           // Pos sphere1
    G4RotationMatrix* zRot = new G4RotationMatrix;                     // assumed not rotate.
    zRot->rotateZ(0.*deg);
    zRot->rotateY(-90.*deg);
    G4double pSPhi = 0. *deg;
    G4double pDPhi = 360 *deg;

    //Sphere
    G4String s1_name_35 = "Sphere1";
    G4double maxRadius1_35 = 17.5 *mm;                                 // no cavity-assumed
    G4Orb* sSphere_1 = new G4Orb(s1_name_35, maxRadius1_35);

    //Tube
    G4String t1_name_35 = "Tube1";
    G4double pRMin_1 = 0. *mm;
    G4double pRMax_1 = 5.25 *mm;
    G4double pDz_1 = (7.323 * 0.5) *mm;
    G4double ang = (180.0-159.0752);
    G4double posTube1_z = (0-17.5 * cos(ang*pi/180)-(7.323*0.5)) *mm;
    G4ThreeVector pos2 = G4ThreeVector(posTube1_z, 0 *mm, 0 *mm); //Tube1
}
```

```

G4Tubs* sTube_1 = new G4Tubs(t1_name_35, pRMin_1, pRMax_1, pDz_1, pSPhi, pDPhi);

// Union Solid 1
G4UnionSolid* uniSolid_1 = new G4UnionSolid("cavity_part1", sSphere_1, sTube_1, zRot, pos2);

//Cone1
G4String c1_name_35 = "Cone1";
G4double innerRad_1 = 0. *mm;
//G4double outerRad_1 = 9.25 *mm;
G4double outerRad_1 = 8.25 *mm;
G4double innerRad_2 = 0. *mm;
//G4double outerRad_2 = 6.25 *mm;
G4double outerRad_2 = 5.25 *mm;
G4double hz_1 = (10.7*0.5) *mm;
G4double posCone1_z = (posTube1_z - pDz_1 - hz_1) *mm;
G4ThreeVector pos3 = G4ThreeVector(posCone1_z, 0 *mm, 0 *mm); //Cone1

G4Cons* sCone_1 = new G4Cons(c1_name_35, innerRad_1, outerRad_1, innerRad_2, outerRad_2,
hz_1, pSPhi, pDPhi);

G4UnionSolid* uniSolid_2 = new G4UnionSolid("cavity_part2", uniSolid_1, sCone_1, zRot, pos3);

//Cone2
G4String c2_name_35 = "Cone2";
G4double innerRad_3 = 0. *mm;
G4double outerRad_3 = ((41.4*0.5)-1) *mm;
G4double innerRad_4 = 0 *mm;
//G4double outerRad_4 = 9.25 *mm;
G4double outerRad_4 = 8.25 *mm;
G4double hz_2 = (70.95*0.5) *mm;
G4double posCone2_z = (posCone1_z - hz_1 - hz_2) *mm ;
G4ThreeVector pos4 = G4ThreeVector(posCone2_z, 0 *mm, 0 *mm); //Cone1

G4Cons* sCone_2 = new G4Cons(c2_name_35, innerRad_3, outerRad_3, innerRad_4, outerRad_4,
hz_2, pSPhi, pDPhi);

G4UnionSolid* uniSolid_3 = new G4UnionSolid("cavity_part3", uniSolid_2, sCone_2, zRot, pos4);

//Tube2
G4String t2_name_35 = "Tube2";
G4double pRMin_2 = 0. *mm;
G4double pRMax_2 = (41.4*0.5) *mm;
G4double pDz_2 = (46.75 * 0.5) *mm;
G4double posTube2_z = (posCone2_z - hz_2 - pDz_2) *mm;
G4ThreeVector pos5 = G4ThreeVector(posTube2_z, 0 *mm, 0 *mm); //Tube1

G4Tubs* sTube_2 = new G4Tubs(t2_name_35, pRMin_2, pRMax_2, pDz_2, pSPhi, pDPhi);

G4UnionSolid* uniSolid_4 = new G4UnionSolid("cavity", uniSolid_3, sTube_2, zRot, pos5);

return uniSolid_4;
}

```

After the spherical applicator volume was generated, a 3D transform (translation and rotation) was applied to the applicator volume. The transformation is necessary since we have to place the spherical applicator in a particular position within the patient volume. Assume the origin of the applicator is at (0,0,0). Due to the treatment conditions, the applicator is translated, for instance, to (110 mm, 20 mm, 0 mm) and rotated at 215 degrees about the z-axis from its initial position at (0,0,0). Such transformations are known as affine transformations. In Geant4, the affine transformation is performed using the *G4AffineTransform* class. According to the *Geant4 User's Guide for Application Developers*, the *G4AffineTransform* is a class for geometric affine transformations that support an efficient arbitrary rotation and transformations of vectors, as well as the computation of compound and inverse transformations ⁴⁸. The relative patient volume and the applicator transform are then determined by inverting the 3D transform matrix of the applicator and then calculating the relative position. A transformed coordinate is then created. The code snippets for the scenario are as follows.

Code 2: 3D transform for the applicator relative to the patient volume.

```
void ZeissCavity::SetNewValue(G4UIcommand * command, G4String val)
{
    if (command == cavity) { set_cavity(cavity->GetNewIntValue (val));}
    //---- and then fill the output files with...
    // build solid of the cavity
    if (cavity_type == 215) {buildCavity215();}
    else if (cavity_type == 220) {buildCavity220();}
    else if (cavity_type == 225) {buildCavity225();}
    else if (cavity_type == 230) {buildCavity230();}
    else if (cavity_type == 235) {buildCavity235();}
    else if (cavity_type == 333) {buildCavity333();}
    else {G4cerr << " _____WARNING::Choose the correct cavity_type_____";}

    //----3D transform for the cavity
    G4ThreeVector posCavity2 ((260.-150.)*mm, (170.-150.)*mm, 0.*mm);
    G4AffineTransform theCavityTransform;
    G4RotationMatrix* zRot2 = new G4RotationMatrix;
    zRot2->rotateZ(-215.*deg);
    zRot2->rotateX(0.*deg);
    zRot2->rotateY(0.*deg);
    theCavityTransform = G4AffineTransform(zRot2, posCavity2).Invert();

    //----Calculate relative phantom - volume 3D transform
    G4PhantomParameterisation* thePhantomParam = GetPhantomParam(true);
```

```

G4RotationMatrix* rotph = new G4RotationMatrix();
G4ThreeVector posPhantom (0 *mm, 0.*mm, 0);
G4AffineTransform thePhantomTransform;

thePhantomTransform = G4AffineTransform( rotph, posPhantom);

G4AffineTransform theTransform;
theTransform = theCavityTransform*thePhantomTransform;
G4ThreeVector axisX( 1., 0., 0. );
G4ThreeVector axisY( 0., 1., 0. );
G4ThreeVector axisZ( 0., 0., 1. );
theTransform.ApplyAxisTransform(axisX);
theTransform.ApplyAxisTransform(axisY);
theTransform.ApplyAxisTransform(axisZ);}

```

The following code snippet describes how to create the .g4cdcm output files and how the required information is included in these files. The .g4cdcm file is created for every slice of the patient volume and performed using the *for loop*. Each of the files was inserted with information such as the number of materials, followed by each material index and its name, and the number of voxels in each slice of the CT file. The materials data was retrieved from the *thePhantomParam*, which gives access to all information of the reconstructed patient geometry. The extractions of the maximum and minimum extension in the x, y, and z axes were based on the initial position and orientation of the reconstructed patient geometry, in which the patient geometry is not translated nor rotated and is at the center of the coordinate system (0,0,0). Thus, the resulting extensions in the x, y, and z are as expected, which are -150 (minimum) and +150 (maximum) for the x and y axes. Meanwhile, the extension in the z-axis depends on the position of each slice in the reconstructed patient geometry.

Code 3: Geant4 code to create output files and insert the required information to build the patient geometry and the cavity into these files.

```

//-----Loop to phantom voxels
G4int nx = thePhantomParam->GetNoVoxelX();
G4int ny = thePhantomParam->GetNoVoxelY();
G4int nz = thePhantomParam->GetNoVoxelZ();

//-----Extract the name of each CT file from Data.dat to be used to name the output files
G4String fileName;
for (G4int iz = 0; iz < nz; iz++)
{

```

```

checkfile >> fileName;
fileName += ".g4cdcm";
std::ofstream fout(fileName);
if(!fout) {
    G4Exception("ZeissCavity::SetNewValue",
        "",
        FatalErrorInArgument,
        G4String("Cannot open output file " + fileName).c_str());
}

//-----Write out the number of phantom materials
std::vector<G4Material*> materials = thePhantomParam->GetMaterials();

//-----Write out each material indices and names
fout << materials.size() * 0.5 << G4endl;

for ( unsigned int ii = 0; ii < 0.5 * materials.size(); ii++ ) {
    fout << ii << " " << materials[ii]->GetName() << G4endl;
}

//-----Write out the number of voxels in X, Y, and Z
fout << nx << " " << ny << " " << 1 << G4endl;

//-----Define the condition for creating the cavity
G4int nxy = nx*ny;
fVoxelsInside = new G4bool[nx*ny*nz];
G4double voxelHalfWidthX = thePhantomParam->GetVoxelHalfX();
G4double voxelHalfWidthY = thePhantomParam->GetVoxelHalfY();
G4double voxelHalfWidthZ = thePhantomParam->GetVoxelHalfZ();

//-----Write Maximum and Minimum extensions in X, Y
fout << -voxelHalfWidthX*nx+thePhantomTransform.NetTranslation().x() << " "
<< voxelHalfWidthX*nx+thePhantomTransform.NetTranslation().x() << G4endl;
fout << -voxelHalfWidthY*ny+thePhantomTransform.NetTranslation().y() << " "
<< voxelHalfWidthY*ny+thePhantomTransform.NetTranslation().y() << G4endl;

```

Code 4 describes the core of the modeled cavity. The developed cavity code uses the information of each patient voxel and the geometrical data of a selected spherical applicator to generate the boundary definition to create a cavity volume. The cavity code shown in the code snippets is for the 3.5 cm diameter spherical applicators. The codes for other types and sizes of the applicator were also developed but not provided here.

Code 4: Geant4 code to create the boundary of the cavity.

```

//-----Loop to get slice position for each slice: the location sequences are made to be continue.

```

```

G4double sliceThickness = 2*voxelHalfWidthZ;
fout << sliceThickness*(iz)+thePhantomTransform.NetTranslation().z() << " "
<< (iz+1)*sliceThickness+thePhantomTransform.NetTranslation().z() << G4endl;

for( G4int iy = 0; iy < ny; iy++) {
  G4bool bPrevVoxelOutside = true;
  G4bool b1VoxelFoundOutside = false;
  G4double voxelCentreX;
  G4double voxelCentreY;
  G4double voxelCentreZ;
  for(G4int ix = 0; ix < nx; ix++){
    voxelCentreX = (-nx+ix*2+1)*voxelHalfWidthX;
    voxelCentreY = (-ny+iy*2+1)*voxelHalfWidthY;
    voxelCentreZ = (-nz+iz*2+1)*voxelHalfWidthZ;
    G4ThreeVector voxelCentre(voxelCentreX, voxelCentreY, voxelCentreZ);
    theTransform.ApplyPointTransform(voxelCentre);
    G4bool bVoxellsOutside = true;
    if (ix >= 220 && ix <= 300 && iy >= 130 && iy <= 210 ){
      for(G4int ivx = -1; ivx <= 1; ivx+=1 ) {
        for( G4int ivy = -1; ivy <= 1; ivy+=1 ){
          for( G4int ivz = -1; ivz <= 1; ivz+=1 ) {

            G4ThreeVector voxelPoint = voxelCentre + ivx*voxelHalfWidthX*axisX +
            ivy*voxelHalfWidthY*axisY + ivz*voxelHalfWidthZ*axisZ;
            if (cavity_type == 235) {
              EInside positionCavity = buildCavity235()->Inside(voxelPoint);
              if(positionCavity == kInside ) {
                bVoxellsOutside = false;
                break;
              } else {}
            } else{}
          }
        }
        if( !bVoxellsOutside ) break;
      }
      if( !bVoxellsOutside ) break;
    }
    G4int copyNo = ix + nx*iy + nxy*iz;
    if( bVoxellsOutside ) {
      if( !bPrevVoxelOutside ) {
        G4Exception("ZeissCavity::SetNewValue",
        "",
        FatalException,
        "Volume cannot subtract phantom in discontinuous
voxels, "
        "please use other voxel");
      }
      if( b1VoxelFoundOutside ) {
        b1VoxelFoundOutside = true;
      }
    }
  }
}

```

```

                                fVoxellsOutside[copyNo] = true;
        } else {
        fVoxellsOutside[copyNo] = false;
    }
}

```

The first part of Code 4 describes the iteration loop to every patient voxel after the initiation of the cavity by the user. The center of every patient voxels are determined and the position of every center in the transformed coordinate is obtained. The *voxelPoint* representing the boundary is then defined. When the creation of the spherical applicator is initiated, its position within the boundary is evaluated such that if the loop check found a point is inside this boundary region then the material and density of this voxel are replaced with air. Otherwise, the material and density of the voxel are remained. Details of the material and density assignments of a particular voxel are described by the following code snippets.

Code 5: Geant4 implementation to replace the material and density of the selected cavity voxels.

```

//-----To Write The Materials
for( G4int iy2 = 0; iy2 < ny; iy2++) {
    G4bool b1xFound = false;
    for(G4int ix2 = 0; ix2 < nx; ix2++){
        size_t copyNo = ix2 + ny*iy2 + nxy*iz;
        if(fVoxellsOutside[copyNo]) {
            G4int matIndices = thePhantomParam->GetMaterialIndex(copyNo);
            fout << matIndices << " ";
            b1xFound = true;
        }
        else if (!fVoxellsOutside[copyNo]) {
            fout << "0 ";
        }
        else{}
    }
    if(b1xFound ) fout<< G4endl;
}
//----To -write densities
for(G4int iy = 0; iy < ny; iy++) {
    G4bool b1xFound = false;
    for(G4int ix = 0; ix < nx; ix++) {
        size_t copyNo = ix + ny*iy + nxy*iz;
        if(fVoxellsOutside[copyNo]) {
            fout <<std::fixed << std::setprecision(6);

```

```

        fout <<thePhantomParam->GetMaterial(copyNo)->GetDensity()/g*cm3<< " ";
        b1xFound = true;
    }
    else if(!fVoxellsOutside[copyNo]) {
        fout << "0.001290 ";
        // Air
    }
    else{}
}
if(b1xFound) fout << G4endl;
}
G4cout << "\n\nOutput file " << fileName << " is written..." << G4endl;
fout.close();
}

```

The cavity output files are named based on an input file, the *Data.dat* file. The *Data.dat* is an input file used by the *DetectorConstruction* to reconstruct the patient geometry. This file contains information such as compression value, the number of CT files imported, and the name of all imported CT files. The information required to name the cavity output file is the number of files and the name of each imported CT file (without the format). Thus, this information was extracted from the *Data.dat*. The reason for naming the cavity output file with the name provided in the *Data.dat* is because similar file name information is used by *DetectorConstruction* in reconstructing the patient geometry such that when the output files (.g4cdcm) are imported later to the source model, the same *Data.dat* file can be used as input for the *DetectorConstruction* to reconstruct the patient geometry and the cavity.

Code 6: Geant4 code to create and set the name of each cavity output file.

```

//-----create the output files
G4String inputfile = "Data.dat";
std::ifstream checkfile(inputfile.c_str());
if(!inputfile) {
    G4Exception("ZeissCavity::SetNewValue",
        "",
        FatalErrorInArgument,
        G4String("File not found " + inputfile).c_str());
}
G4int compressionValue;
checkfile >> compressionValue;
// not
used
G4int nFile;
checkfile >> nFile;

```

The modified material and density information was saved as a series of new text files with the extension of .g4cdcm. A .g4cdcm file has the same structure and information as the .g4dcm file, except it now includes the cavity definition. The .g4cdcm files were read by the *DetectorConstruction* and the patient geometry and the cavity were subsequently built. The implementation of the cavity subtraction from the phantom container uses the *G4SubtractionSolid* class of the Geant4 toolkit and is described in the following code.

Code 7: Geant4 code to create and set the name of each cavity output file.

```
//---- Define the volume that contains all the voxels
fContainer_solid = new G4Box("phantomContainer",fNVoxelX*fVoxelHalfDimX,
fNVoxelY*fVoxelHalfDimY,
fNVoxelZ*fVoxelHalfDimZ);

// Creating sphere for the cavity
G4double rMax = 17.5*mm;
G4Orb* sSphere_1 = new G4Orb ("cavity", rMax);

//Tube
G4ThreeVector pos1 = G4ThreeVector(0 *mm, 0 *mm, 0 *mm); //sphere1
G4RotationMatrix* zRot = new G4RotationMatrix; //assumed
not rotated.
zRot->rotateZ(0.*deg);
zRot->rotateY(-90.*deg);
G4double pSPhi = 0. *deg;
G4double pDPhi = 360 *deg;
G4String t1_name_35 = "Tube1";
G4double pRMin_1 = 0. *mm;
G4double pRMax_1 = 6.25 *mm;
G4double pDz_1 = (7.323 * 0.5) *mm;
G4double ang = (180.0-159.0752);
G4double posTube1_z = (0-17.5 * cos(ang*pi/180)-(7.323*0.5)) *mm;
G4ThreeVector pos2 = G4ThreeVector(posTube1_z, 0 *mm, 0 *mm); //Tube1
G4Tubs* sTube_1 = new G4Tubs(t1_name_35, pRMin_1, pRMax_1, pDz_1, pSPhi, pDPhi);

// Union Solid 1
G4UnionSolid* uniSolid_1 = new G4UnionSolid("cavity_part1", sSphere_1, sTube_1, zRot, pos2);

//Cone1
G4String c1_name_35 = "Cone1";
G4double innerRad_1 = 0. *mm;
G4double outerRad_1 = 9.25 *mm;
```

```

G4double innerRad_2 = 0. *mm;
G4double outerRad_2 = 6.25 *mm;
G4double hz_1 = (10.7*0.5) *mm;
G4double posCone1_z = (posTube1_z - pDz_1 - hz_1) *mm;
G4ThreeVector pos3 = G4ThreeVector(posCone1_z, 0 *mm, 0 *mm); //Cone1

G4Cons* sCone_1 = new G4Cons(c1_name_35, innerRad_1, outerRad_1, innerRad_2, outerRad_2,
hz_1, pSPhi, pDPhi);

G4UnionSolid* uniSolid_2 = new G4UnionSolid("cavity_part2", uniSolid_1, sCone_1, zRot, pos3);

//Cone2
G4String c2_name_35 = "Cone2";
G4double innerRad_3 = 0. *mm;
G4double outerRad_3 = (41.4*0.5) *mm;
G4double innerRad_4 = 0 *mm;
G4double outerRad_4 = 9.25 *mm;
G4double hz_2 = (70.95*0.5) *mm;
G4double posCone2_z = (posCone1_z - hz_1 - hz_2) *mm ;
G4ThreeVector pos4 = G4ThreeVector(posCone2_z, 0 *mm, 0 *mm); //Cone1

G4Cons* sCone_2 = new G4Cons(c2_name_35, innerRad_3, outerRad_3, innerRad_4, outerRad_4,
hz_2, pSPhi, pDPhi);

G4UnionSolid* uniSolid_3 = new G4UnionSolid("cavity_part3", uniSolid_2, sCone_2, zRot, pos4);

G4ThreeVector transl(110, (170-150), 0); // untuk 300x300x233
//G4ThreeVector transl(110, (170-150), 0); // 300-260 = 40. 0 ditengah kr ikut world. jadi posisi
cavity (150-40) = 110.
G4RotationMatrix* zRot2 = new G4RotationMatrix;
zRot2->rotateZ(-215.*deg);
G4SubtractionSolid* fContainer_cavity = new G4SubtractionSolid("fContainer_cavity",
fContainer_solid, uniSolid_2, zRot2, transl);

```

To subtract the phantom container, the outer part of the spherical applicator is created using boolean solid. All the applicator parts are then combined using the class *G4UnionSolid*. The initial volume of a phantom container is a simple box. A new phantom container is subsequently created by subtracting the applicator from the initial volume of the phantom container. The resulted cavity is presented in **Figure 2-7** below.

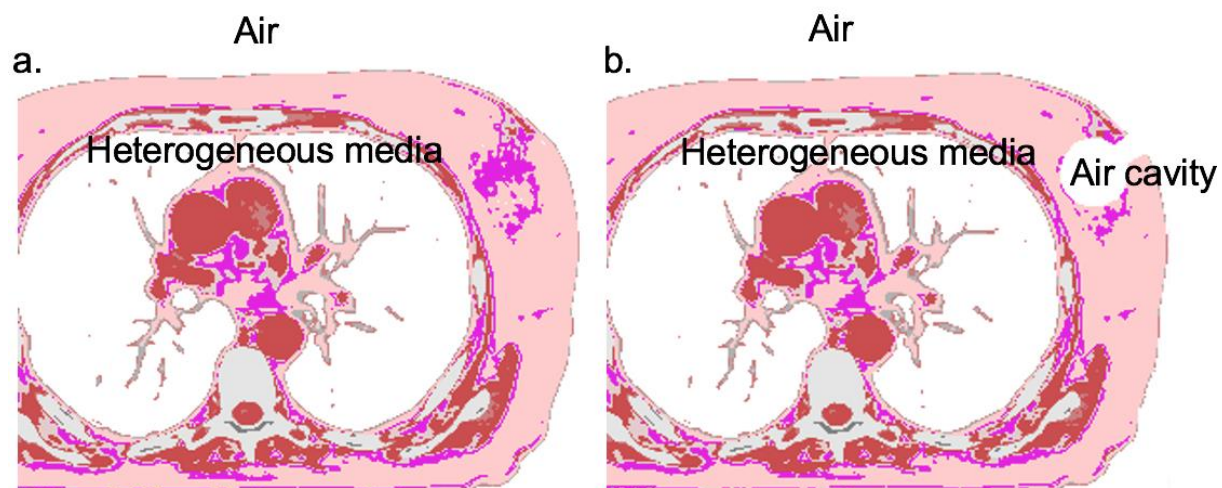


Figure 2-7. Visualization of the reconstructed patient geometry. a. with no cavity and b. with the cavity. The created cavity has the size corresponding to the size of the used spherical applicator.

2.6 Applicator position and orientation

The previous version of the source model offers the ability to change the applicator position and orientation in all axes. However, the particle generator and scoring are valid only for a fixed-predefined applicator position. **Figure 2-8** illustrates the trajectories of 100 primaries photon when the applicator is translated, rotated, and both translated and rotated. The generated radiation was modeled correctly if the applicator was either translated or rotated at a defined position (**Figure 2-8**). In this work, the applicator has to be translated and rotated from its initial position and orientation to adjust its position within the surgical incision or the tumor bed. However, in **Figure 2-8**, the trajectories of the photon is incorrect when the applicator is translated and rotated. To have a valid model of particle generator and scoring for such a situation, the algorithm should be adaptable to the position and orientation shifts. The adjustment to

the position and orientation shift is applied in the *PrimaryGeneratorAction* and the *SteppingAction* classes of the source model.

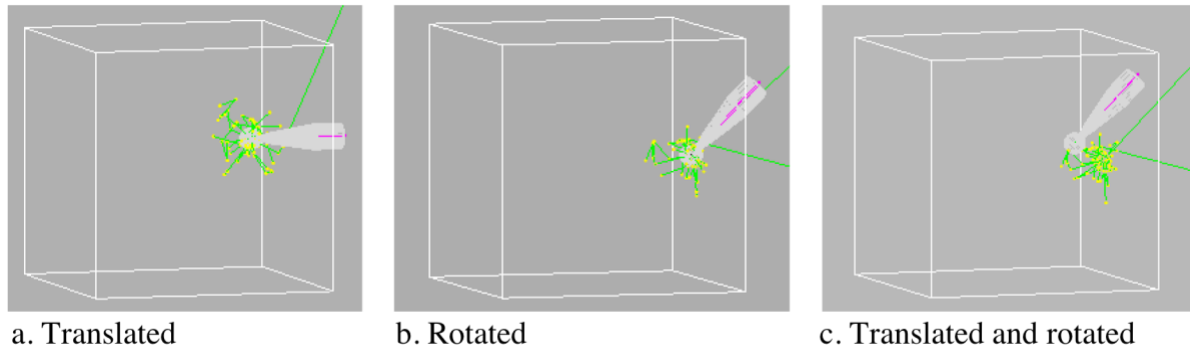


Figure 2-8. Visualization of the trajectories of 100 primaries photons generated when the applicator is a. only translated (50 mm and 30 mm along the-x and y-axes, respectively), b. only rotated (by 315 degrees around the-z axis), and c. both translated and rotated (displaced 50 mm along the-x axis and 30 mm along the y-axis, and rotated subsequently by 315 degrees around the-z axis).

Particle generator and particle scoring in the algorithm are associated with the *PrimaryGeneratorAction* class and the *SteppingAction* class (both are members of the *Run* category of the Geant4 toolkit). Descriptions of these classes are in sections 2.3.2 and 2.3.3. As previously described, the *PrimaryGeneratorAction* class controls all the parameters to produce the primary particle. The controlled parameters are the initial position and orientation of the primary particles. If the position and orientation of the applicator change, then these changes have to be applied as well to the primary particle.

Meanwhile, the *SteppingAction* class conducts particle scoring, extracting relevant and valuable information about a particle when it travels through matter or tissue. In Geant4, scoring is always done in a 3D volume and depends upon the simulated scene or simulation setup. The scoring plane of the INTRABEAM source is the external surface of the INTRABEAM's drift tube ²⁴. In breast IORT treatment with the

INTRABEAM device, a spherical applicator is attached to the XRS. The scoring surface is, therefore, the outer surface of the spherical applicator.

2.6.1 Implementation of the position and orientation shifts into the *PrimaryGeneratorAction* class of the source model

The implementation of the position and orientation shifts to the *PrimaryGeneratorAction* class of the source model is straightforward by using the *G4RotationMatrix* and the *G4ThreeVector* classes. The *G4RotationMatrix* allows to rotate a particle or a solid about the coordinate axes, while the *G4ThreeVector* translates the position of the particle or volume. The following code snippet describes how the position and orientation of a primary photon is readjusted due to the position and orientation shifts of the applicator.

Code 8: GEANT4 implementation of applicator positioning correction.

```
//Kinetic energy
kinE = 50*keV;
particleGun->SetParticleEnergy(kinE);
pos1 = rm* pos; //Rotation then translation

//Matrix translation applied to initial position and orientation of the particles
G4ThreeVector pos5((pos1(0)+AppltranslationX), (pos1(1)+AppltranslationY),
(pos1(2)+AppltranslationZ));

//New position and orientation for the primaries
dir = rm*dir;
particleGun->SetParticlePosition(pos5);
particleGun->SetParticleMomentumDirection(dir);
```

The algorithm simply rotates and translate the primary particles using the *rm* and *AppltranslationX*, *AppltranslationY*, *AppltranslationZ*. The *rm* is a rotation matrix applied to the initial position *pos*, while *pos1* is the position of the particle after rotation. The variables *AppltranslationX*, *AppltranslationY*, and *AppltranslationZ* represent the applicator translation in the x, y and z-axes. The *rm* (*rotation in x, y, and z-axis*), *AppltranslationX*, *AppltranslationY*, and *AppltranslationZ* are inputs provided by users through a GUI. The new position and orientation of the primary particle is then saved

as a position vector $pos5$. The $pos5$ are then applied to the $particleGun$, the particle generator (see section 2.3.2). As a result, the position and orientation of the generated primary particles follow the position and orientation of the applicator according to the input provided by the user in the simulation.

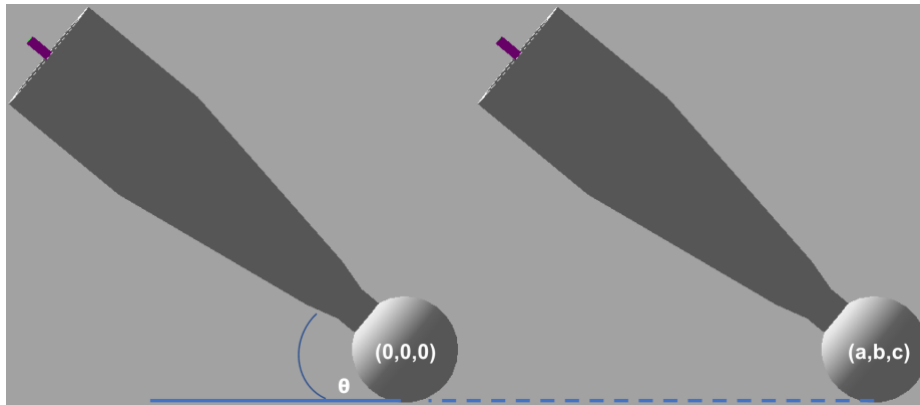


Figure 2-9. Visualization of the applicator position and orientation after rotation around the coordinate center $(0,0,0)$ and translation to a coordinate point (a, b, c) .

2.6.2 Derivation of scoring equations the spherical applicator and their implementation within the *SteppingAction* class of the source model.

2.6.2.1 The coordinate system and the scoring surface of the source

The origin of the coordinate system for the INTRABAM source is the central point in the union plane between the hemispherical and cylindrical parts of the INTRABEAM drift tube²⁴. The reference coordinate system for the bare probe is shown in **Figure 2-10**. The geometrical model of the INTRABEAM drift tube consists of a hemispherical and a cylinder joined together at one end. The x-axis specifies the long axis of the source, while the y and z-axes represents the transverse plane.

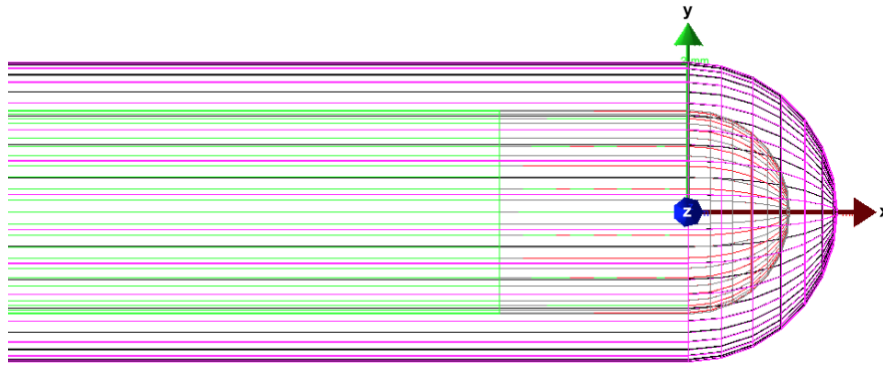


Figure 2-10. The modelled INTRABEAM source probe and its coordinate system.

A particle will be scored if it crossed the external surface of the drift tube. Based on the reference coordinate system, a photon particle will be scored in a scoring volume if it either fulfilled the following conditions,

$$y^2 + z^2 \geq R|x| \leq 0 \quad (2-1)$$

or

$$x^2 + y^2 + z^2 \geq R|x| \geq 0 \quad (2-2)$$

The variable R is the approximate radius of the external surface of the INTRABEAM drift tube (≈ 1.6 mm).

2.6.2.2 The reference coordinate system and the scoring surface for the spherical applicator

Figure 2-11 shows the reference coordinate system for the spherical applicator. The origin of the coordinate system is the center of the sphere. For the breast IORT treatment with the INTRABEAM device, a spherical applicator is applied to the source and placed afterward in a particular position within a patient geometry. The scoring volume is, therefore, the external surface of the spherical applicator and the patient geometry. A particle will be scored after crossing the external surface of the spherical applicator.

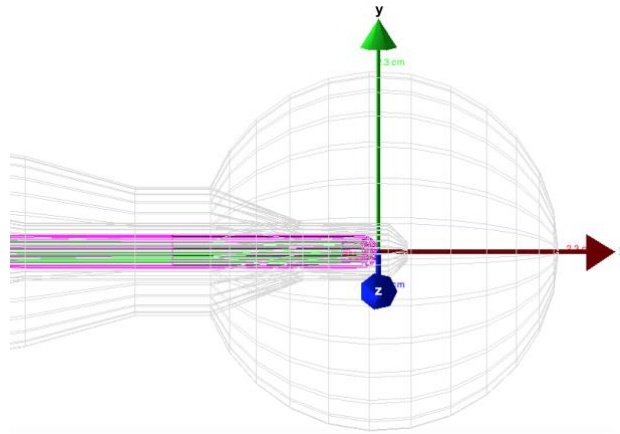


Figure 2-11. The modeled INTRABEAM spherical applicator and its coordinate system. The x-axis defines the long axis of the applicator. The y and z-axes specify the transverse plane.

2.6.2.3 Particle scoring for the spherical applicator

As described in the preceding section, the scoring plane of the particles is the external surface of the spherical applicator. The considered applicator parts for the scoring purpose are the sphere and the shank (cylinders and cones). However, for the simplicity of particle scoring, the spherical applicator is assumed to consist of a sphere and a cylinder only. The geometrical model of the spherical applicator is presented in **Figure 2-12**.

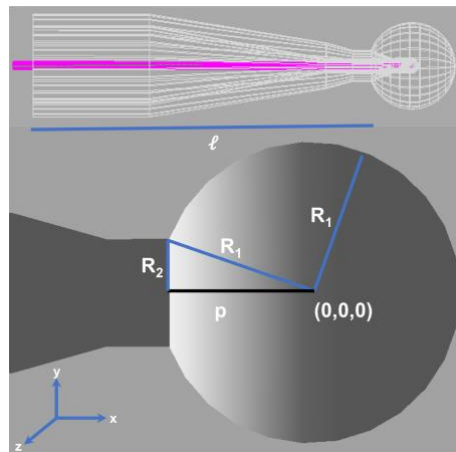


Figure 2-12. Geometrical model of the INTRABEAM source and its spherical applicator.

Based on the reference coordinate system (**Figure 2-11**) and the geometrical model of the spherical applicator (**Figure 2-12**), either of the following conditions must be fulfilled for a photon to be scored,

$$y^2 + z^2 \geq R_1^2 \mid -p - l \leq x \leq -p \quad (2-3)$$

Or,

$$x^2 + y^2 + z^2 \geq R_2^2 \mid x \geq -p \quad (2-4)$$

Where $x, y,$ and z represent the position of a photon particle in the reference coordinate system. Variable R_1 denotes the radius of the sphere, R_2 is the radius of the cylinder, l is the length of the tube, and p is the distance of the tube from the sphere. All of these variable values depend on the diameter of the spherical applicator used. Variable R_1 and R_2 for the 3.5 cm spherical applicator are 17.5 mm and 6.25 mm, respectively. Variable p is determined using the Pythagoras theorem, where the obtained value is 16.3459 mm.

2.6.2.4 Translation and rotation

In the breast IORT treatment with the INTRABEAM device, a spherical applicator is adjusted to the position of the tumor bed (surgical cavity). The adjusting might be by translating the applicator to a particular position and rotating it about the z-axis. The translation and rotation applied to the applicator modify the equations (2-3) and (2-4) above.

Assume that the initial position and orientation of a photon particle is at (0,0,0). Since the applicator is rotated and subsequently translated, as described in *PrimaryGeneratorAction*, the new position and orientation of the photon particle (x', y', z') because of the rotation at angle θ along the z-axis and translation to (a, b, c) is derived as follows.

$$\begin{pmatrix} x' \\ y' \\ z' \end{pmatrix} = \begin{pmatrix} \cos\theta & -\sin\theta & 0 \\ \sin\theta & \cos\theta & 0 \\ 0 & 0 & 1 \end{pmatrix} \begin{pmatrix} x \\ y \\ z \end{pmatrix} + \begin{pmatrix} a \\ b \\ c \end{pmatrix} \quad (2-5)$$

In which the $\begin{pmatrix} \cos\theta & -\sin\theta & 0 \\ \sin\theta & \cos\theta & 0 \\ 0 & 0 & 1 \end{pmatrix}$ is the rotation matrix at the z-axis and the $\begin{pmatrix} a \\ b \\ c \end{pmatrix}$ represents the translation of (x, y, z) to a position (a, b, c) . Equation (2-6) can be written as,

$$\begin{pmatrix} x \\ y \\ z \end{pmatrix} = \begin{pmatrix} \cos\theta & \sin\theta & 0 \\ -\sin\theta & \cos\theta & 0 \\ 0 & 0 & 1 \end{pmatrix} \begin{pmatrix} x' - a \\ y' - b \\ z' - c \end{pmatrix} \quad (2-6)$$

from this equation we obtain,

$$(x) = (x' - a)\cos\theta - (y' - b)\sin\theta \quad (2-7)$$

$$(y) = (a - x')\sin\theta + (y' - b)\cos\theta \quad (2-8)$$

and,

$$z = z' - c \quad (2-9)$$

by substituting equations (2-7), (2-8), and (2-9) into equations (2-3) and (2-4), new conditions for the particle scoring are obtained. A photon particle will be scored if it satisfies either of the following conditions,

$$((a - x')\sin\theta + (y' - b)\cos\theta)^2 + z^2 \geq R_1^2 \quad (2-10),$$

or

$$((x' - a)\cos\theta + (y' - b)\sin\theta)^2 + ((a - x')\sin\theta + (y' - b)\cos\theta)^2 + z^2 \geq R_2^2 \quad (2-11)$$

by solving eq. (2-11), we obtain,

$$(x' - a)^2 + (y' - b)^2 + (z' - c)^2 \geq R_2^2 \quad (2-12)$$

in which, equations (2-10) and (2-12) are true if the following conditions are fulfilled,

$$(x' - a)\cos\theta + (y' - b)\sin\theta > -p \quad (2-13)$$

$$-p - l(x' - a)\cos\theta + (y' - b)\sin\theta \leq -p \quad (2-14)$$

The implementations of the equations into the algorithm are as follow.

Code 9: The implementation of applicator positioning in the *SteppingAction* class.

```
G4int ZeissSteppingAction::check_condition( const G4Step& aStep, G4SteppingManager &)
{
    // Initial conditions for particle scoring
    condition1 = sqrt((PosiY * PosiY) + (PosiZ * PosiZ));
    condition2 = sqrt((PosiX * PosiX) + (PosiY * PosiY) + (PosiZ * PosiZ));

    // The application of the new applicator position and orientation is only applicable for the spherical
    // applicator
    // New conditions are defined based on the derived equations above
    if ( (app_type == 215) || (app_type == 220) || (app_type == 225) || (app_type == 230) || (app_type
    == 235) || (app_type == 240) || (app_type == 245) || (app_type == 250))
    {
        condition1= sqrt((((AppltranslationX-PosiX)*sin(ApplRotateZ))+((PosiY-
        AppltranslationY)*cos(ApplRotateZ)))
        *(((AppltranslationX-PosiX)*sin(ApplRotateZ))+((PosiY-
        AppltranslationY)*cos(ApplRotateZ))))+
        (((PosiZ-AppltranslationZ) * (PosiZ-AppltranslationZ)))); // eq. 2-10
        condition2 = sqrt(pow((PosiX-AppltranslationX),2) + pow((PosiY-AppltranslationY),2) + pow((PosiZ-
        AppltranslationZ),2)); // eq. 2-12

        // Get access to the DetectorConstruction, volumes and edep
        const ZeissDetectorConstruction* detectorConstruction = static_cast<const
        ZeissDetectorConstruction*>
        (G4RunManager::GetRunManager()->GetUserDetectorConstruction());
        G4VPhysicalVolume* volume = aStep.GetPreStepPoint()->GetTouchableHandle()->GetVolume();
        edep = (aStep.GetTotalEnergyDeposit())/CLHEP::keV;
    }
}
```

```

// Specified that the volume is the defined scoring volume and a particle will be scored if it
fulfill the conditions
in equations. 2-11, 2-13, 2-14, and 2-15)
if (volume == detectorConstruction->GetScoringVolume()) {
    if (((PosiX-AppItranslationX)*cos(AppIRotateZ)) + ((PosiY-
AppItranslationY)*sin(AppIRotateZ)) >= point1) && (((PosiX-AppItranslationX)*cos(AppIRotateZ)) +
((PosiY-AppItranslationY)*sin(AppIRotateZ)) <= point2 ) && (condition1 >= rphsp1)) {return true;}
        // rphsp1 = R1
    else if (((PosiX-AppItranslationX)*cos(AppIRotateZ)) + ((PosiY-
AppItranslationY)*sin(AppIRotateZ)) >
point2) && (condition2 >= rphsp2) ) {return true;}           // rphsp2 = R2
    else {return false;}
}
else {
    if (((PosiX-AppItranslationX)*cos(AppIRotateZ)) + ((PosiY-
AppItranslationY)*sin(AppIRotateZ)) >= point1) && (((PosiX-AppItranslationX)*cos(AppIRotateZ)) +
((PosiY-AppItranslationY)*sin(AppIRotateZ)) <= point2 ) && (condition1 >= rphsp1))
        // point2 = p,
        {return true;}
    else if (((PosiX-AppItranslationX)*cos(AppIRotateZ)) + ((PosiY-
AppItranslationY)*sin(AppIRotateZ))
> point2) && (condition2 >= rphsp2) )
        {return true;}
    else {return false;}}
} else {
    if ((condition1 >= rphsp1) && (edep > 0)) {return true;}
    else if (((PosiX-AppItranslationX)*cos(AppIRotateZ)) + ((PosiY-
AppItranslationY)*sin(AppIRotateZ)) > point2) && (condition2 >= rphsp2) && (edep > 0))
        {return true;}
    else {return false;}
}
}
}

```

2.7 The dose scoring algorithm

The scoring algorithm in the earlier version of the source model was to calculate dose distribution for a homogeneous water phantom. The dose delivered to this phantom is estimated by tallying deposited energy (edep). For a simple homogeneous water phantom, assuming the dose to equal energy deposition is considered adequate as the density value for water is 1 g cm⁻³. Since the work aims to investigate absorbed dose distribution in a volume consisting of complex tissues and structures, the absorbed dose considering the density of each unique material/tissue that radiation passes through is the preferred variable to obtain.

A previous study conducted by McCarthy⁶⁰ estimated the absorbed dose in spongiosa and CT-scanned bone using the prior version of the source model. However, because the absorbed dose was calculated post-processing by dividing the energy distribution by the appropriate density value, it only provided a rough estimation of the absorbed dose and did not improve the scoring algorithm. A more advanced scoring algorithm integrated into the source model is required to calculate the absorbed dose in the patient geometry. Unlike the post-processing approach, the developed scoring algorithm is straightforward and is integrated within the source model. The algorithm calculates the absorbed dose in the medium by dividing the deposited energy with mass (*edep/mass*) and accumulates the calculated doses throughout the simulation. This approach considers the density of each individual material of the patient volume in the dose calculations. The snippets of the implemented codes within the INTRABEAM source model are as follows.

Code 10: Algorithm for calculating the absorbed doses by considering patient tissue heterogeneities.

```
// Function to perform dose calculation in the scored volume
void ZeissAnalysis2::patientDose( const G4Step& step, G4SteppingManager &) //fn5
{
    // To get edep
    G4Track* aTrack = step.GetTrack();
    edep = (step.GetTotalEnergyDeposit());
    G4double posX = aTrack->GetPosition().x() *mm;
    G4double posY = aTrack->GetPosition().y() *mm;
    G4double posZ = aTrack->GetPosition().z() *mm;

    x = round(posX); y = round(posY); z = round(posZ);

    // To get material density, and name of the material
    G4double density = step.GetTrack()->GetMaterial()->GetDensity()/(g/cm3);

    G4String matName = step.GetPreStepPoint()->GetMaterial()->GetName();

    // Voxel size
    G4double volz = 1.*mm3/cm3;
    G4double mass = density * volz;

    // Loop to every voxel
    if ((x > 300) || (y > 300) || (z > 233)) {}
}
```

```

else if ((x<0) || (y < 0) || (z < 0)) {}
else {
    N = ZeissPrimaryGeneratorAction::getNode_Proc_Num();
    if (co_ordinates[z][y][x].LASTHI == N)
        { //local scoring. Accumulates the scores WITHIN a particular history
            co_ordinates[z][y][x].Dose_temp = co_ordinates[z][y][x].Dose_temp + edep/mass;
        } else {
            // Global scoring. Empties the local scores into the global container during the NEXT
            history.
            co_ordinates[z][y][x].dose_deposit      += co_ordinates[z][y][x].Dose_temp;
            co_ordinates[z][y][x].dose_deposit2     +=(co_ordinates[z][y][x].Dose_temp
            *co_ordinates[z][y][x].Dose_temp);

            // Local container assumes the value of the CURRENT SCORE
            co_ordinates[z][y][x].Dose_temp = edep/mass;
            co_ordinates[z][y][x].LASTHI = N;
        }
    }
}
}

```

The algorithm described above is the most important part from the whole scoring algorithm to calculate the absorbed dose. The first part of this algorithm is to retrieve information about the deposition energy (*edep*), material name, and density of each voxel that the x-ray radiation passed through within the patient volume. From this information, mass is computed. The absorbed dose (*edep/mass*) is then calculated and accumulated within the scoring voxels during the simulation. The scoring volume is defined based on the CT-based patient geometry. Thus, the number of voxels and size of each scoring voxel are set identical to those of the constructed patient geometry. The number of voxels created for the scoring purpose is 300 × 300 × 233 voxels.

2.8 The visualization

Visualization is an essential part of the Geant4 toolkit. In Geant4, a GUI is an existing tool that can be used by the users to verify the simulated geometrical model and physics process. Its potential to produce graphical representations of the geometrical hierarchy and draw views and sections of the detector will help users better understand the developed geometrical model. The visualization in this work is primarily to visualize

the applicator and reconstructed patient geometries and assess the position of the applicator relative to the tumor bed.

2.8.1 The initial feature of the GUI

The previous version of the algorithm was also packed with the visualization capability, which allows the visualization of the modeled INTRABEAM source, applicators, and phantom geometries. **Figure 2-13** demonstrates the visualization GUI. On the left panel of the GUI, there are several menus available. Each menu is used to describe the simulation setup. *Appl* is the menu for the applicator in which users can build an applicator and change its position (translate and rotate) relative to the reference coordinate system. A menu dedicated to the phantom geometry (*Phantom*) was also added. The *Phantom* is used to create a phantom geometry and specify its material (vacuum or water), size, and position. The *Analysis* is the menu used to change the voxel size of the scoring volume. By default, the voxel size of the scoring volume (water phantom) is 1mm^3 . Within the *Analysis*, the voxel size of the scoring volume can be redefined, for instance, to 0.1mm^3 . The menu *Generator* offers options to select the radiation source used in a simulation. The *Generator* provides two radiation sources: the primary electron source and the VSM source, whose type depends on the purpose of the simulation. The menu *SteppingAction* is used to generate a PSF or a 3D dose file. If the desired output is the dose, then the 3D dose distribution within a water phantom is simulated. If there is a change to the source, applicator, or phantom geometry, a submenu *update_geometry* is used to update the geometry. A built geometry does not exist until it is updated.

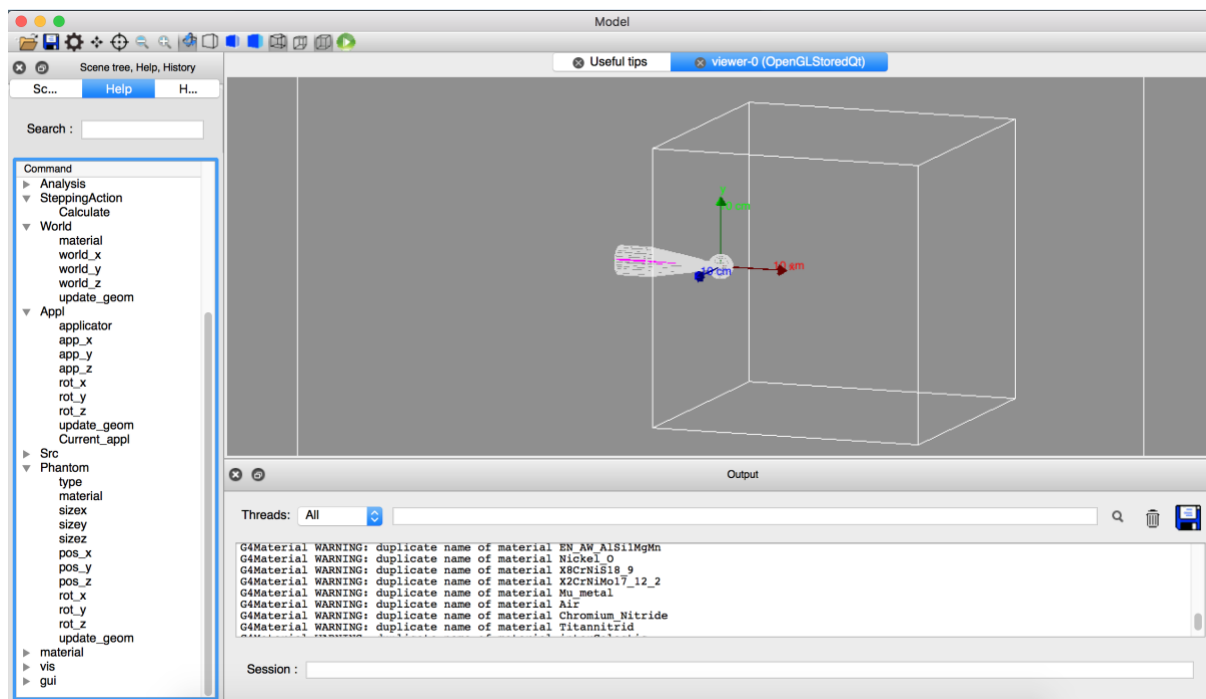


Figure 2-13. The initial version of the developed GUI. A 3.5 cm spherical applicator positioned in a water phantom is visualized.

2.8.2 Methods to run a simulation

There are several options to run a simulation. The first option is to use the GUI ⁶¹. Access to the GUI is through the terminal window by navigating to a working directory and executing the compiled code (**./Model**). A window similar to **Figure 2-13** will open. Users provide a command via the *Session* box of the interface. The available list of commands can be found on the left panel of the GUI. This method is not encouraged because it is slow, especially in performing a simulation. However, the GUI approach is necessary to gain confidence that a simulation setup is accurate.

The second option to perform a simulation is by using the command approach ⁶¹. The command approach employs the compiled code (**./Model**) with a list of commands saved in a macro file named *vis.mac*. This file contains all the instructions required to execute and is editable. Unlike the GUI approach, the GUI in this method will open without the requirement to input line-by-line commands in the *Session* box.

Another option is to use the script method. It is the fastest method of all approaches to perform a simulation ⁶¹. A script is saved as a.txt file and consists of only commands to perform a simulation. No commands to visualize the built geometry are included. Thus, a GUI window is not instantiated. A script is also executed via the terminal window using the compiled code (**./Model**) followed by the script file name. It is recommended to verify the simulation setup using the GUI before switching to the script to perform the simulation. Following is a sample script to perform a simulation to calculate the 3D dose distribution in a water phantom using the 3.0 cm spherical applicator.

Script 1: Example of the content of a script.

```
/Generator/particle_source 2  
/Analysis/Zoom 2  
/Appl/update_geom  
/Appl/applicator 230  
/Phantom/type 666  
/Appl/update_geom  
/SteppingAction/Calculate 5  
#/Appl/update_geom  
/run/beamOn 2000000
```

2.8.3 The new feature of the GUI

Since we have added several new features to the INTRABEAM source model, The existing features are improved. The new capabilities are implemented into the GUI through a defined messenger class of the *DetectorConstruction* derived from the *G4UImessenger* class of the Geant4 package. A messenger class can handle more than one UI commands. Within the messenger class, all commands are defined and deleted. The definition and deletion of the commands in the algorithm are described in Code 11.

The code to define and incorporate commands describing the patient in the existing command directory is through the *G4UIdirectory* class. The users can also add a short

description of the command by the *SetGuidance*. Its implementation in the algorithm is described in Code 11 below. The *G4UIcommand* is a class that represents a UI command and must be instantiated by the users. Geant4 provides derivatives of the *G4UIcommand* according to the types of associating input parameters. The *G4UIcmdWithAnInteger* is used to define a command with an integer input parameter. The *G4UIcmdWithADoubleAndUnit* is used to create a command with an input parameter whose type is double and has a defined unit. For example, the defined unit in *patient_px* (Code 11) is mm and cm (*patient_px->SetUnitCandidates("mm cm")*). Users should explicitly provide the unit when providing an input parameter. If there is no input parameter, the new *G4UIcmdWithoutParameter* is used.

Code 11: Geant4 code to define and delete commands.

```
ZeissDetectorMessenger::ZeissDetectorMessenger(ZeissDetectorConstruction* ZeissDet)
:ZeissDetector(ZeissDet)
{
    Patient = new G4UIDirectory("/Patient/");
    Patient->SetGuidance("UI commands for Patient's dicom");

    patient_build = new G4UIcmdWithAnInteger("/Patient/build",this);
    patient_build->SetGuidance("Select Patient. 001 builds patient");
    patient_build->SetGuidance("Candidates is: 001");
    patient_build->SetParameterName("Patient",false);
    patient_build->AvailableForStates(G4State_PreInit, G4State_Idle);

    patient_px = new G4UIcmdWithADoubleAndUnit("/Patient/patient_x",this);
    patient_px->SetGuidance("Set Patient X position.");
    surf_app_x->SetDefaultValue(0);
    surf_app_x->SetParameterName("Position_x",false);
    patient_px->SetUnitCandidates("mm cm");
    patient_px->AvailableForStates(G4State_PreInit, G4State_Idle);

    patient_py = new G4UIcmdWithADoubleAndUnit("/Patient/patient_y",this);
    patient_py->SetGuidance("Set Patient Y position.");
    surf_app_y->SetDefaultValue(0);
    surf_app_y->SetParameterName("Position_x",false);
    patient_py->SetUnitCandidates("mm cm");
    patient_py->AvailableForStates(G4State_PreInit, G4State_Idle);

    patient_pz = new G4UIcmdWithADoubleAndUnit("/Patient/patient_z",this);
    patient_pz->SetGuidance("Set Patient Z position.");
    surf_app_z->SetDefaultValue(0);
    surf_app_z->SetParameterName("Position_y",false);
    patient_pz->SetUnitCandidates("mm cm");
}
```

```

    patient_pz->AvailableForStates(G4State_PreInit, G4State_Idle);

    geom_update4 = new G4UIcmdWithoutParameter("/Phantom/update_geom",this);
    geom_update4 ->SetGuidance("Update Geometry.");
    geom_update4 ->AvailableForStates(G4State_PreInit, G4State_Idle);
}

ZeissDetectorMessenger::~ZeissDetectorMessenger()
{
    delete patient_build;
    delete geom_update4;
    delete mv_patient_x;
    delete mv_patient_y;
    delete mv_patient_z;
}

```

The *SetnewValue* provides input for the defined command. It converts the input parameter string provided by the user to appropriate values and invoke an appropriate method of the target class. This method is invoked when a command is issued.

Code 12: The input code for the GUI command.

```

void ZeissDetectorMessenger::SetNewValue(G4UIcommand* cmd, G4String val)
{
    if( cmd == patient_build) { ZeissDetector->set_patient_build(patient_build->GetNewIntValue (val));}
    else if( cmd == patient_px) { ZeissDetector->mv_patient_x(patient_px->GetNewDoubleValue (val));}
    else if( cmd == patient_py) { ZeissDetector->mv_patient_y(patient_py->GetNewDoubleValue (val));}
    else if( cmd == patient_pz) { ZeissDetector->mv_patient_z(patient_pz->GetNewDoubleValue (val));}
    else {};
}

```

2.9 Dose quantifications

2.9.1 Dose in heterogeneous medium

The absorbed dose distribution in the target volume and the OARs of a patient were conducted by considering patient tissue heterogeneity and assuming that the applicator fits the tumor cavity perfectly. All the performed simulations used the modified pre-operative CT scans, with the applicator positioned in the tumor bed located in the left breast (**Figure 2-14**). A total of 300 × 300 × 233 voxels with 3D voxel grids of 1 mm × 1 mm × 1 mm were imported into the source model. Voxels outside

the patient outlines were assigned as air. The absorbed dose deposited in each patient voxel and dose calculation uncertainty were then estimated. The dose was scored in 1 mm × 1 mm × 1 mm voxel grids corresponding to the CT voxel size. Since the code for the source model was parallelized and the application was run on a computer with multiple processors, the simulation results from all the processors were combined at the end of a simulation to create a single dose file.

2.9.2 Dose in homogeneous medium vs. heterogeneous medium

Because the current clinical dose prescription is based on a depth dose curve measured in water, we compared the dose distribution of a homogeneous patient CT to reality (the heterogeneous patient CT). A homogeneous water-equivalent patient CT was acquired using the reference CT scan by setting all materials of the patient volume to water and maintaining the materials outside the patient volume to be air. A MATLAB program was developed and the assignments of the patient tissue materials to water are achieved using the organ outlines provided in the DICOM-RT structure data. The boundary for the patient volume is created using the outline for the patient body and assigned the pixel values to the value that represents water. The imported patient files were checked to ensure that the resulting density and material are for water. There are two assessment: Using the GUI or direct checking of the resulting .g4dcm file. In the simulations, the same number of particles was simulated for both the homogeneous and heterogeneous treatment setups. As demonstrated by other authors, the number of simulated particles can be related to the number of Monitor Units (MU) and the treatment time^{62,63}. A direct comparison of their resulting dose distribution is therefore valid. Any observed differences in the dose distributions are, hence, the result of the differential absorptions of the materials in the different setups. The calculated percentage dose difference between the dose data points of the homogeneous and heterogeneous CT was calculated according to the following equation,

$$\text{Relative dose difference (\%)} = \frac{D_{\text{heterogeneous}} - D_{\text{homogeneous}}}{D_{\text{homogeneous}}} \times 100\% \quad (2-15)$$

Where $D_{heterogeneous}$ represents the absorbed dose of the heterogeneous CT and $D_{homogeneous}$ is the absorbed dose of the homogeneous CT.

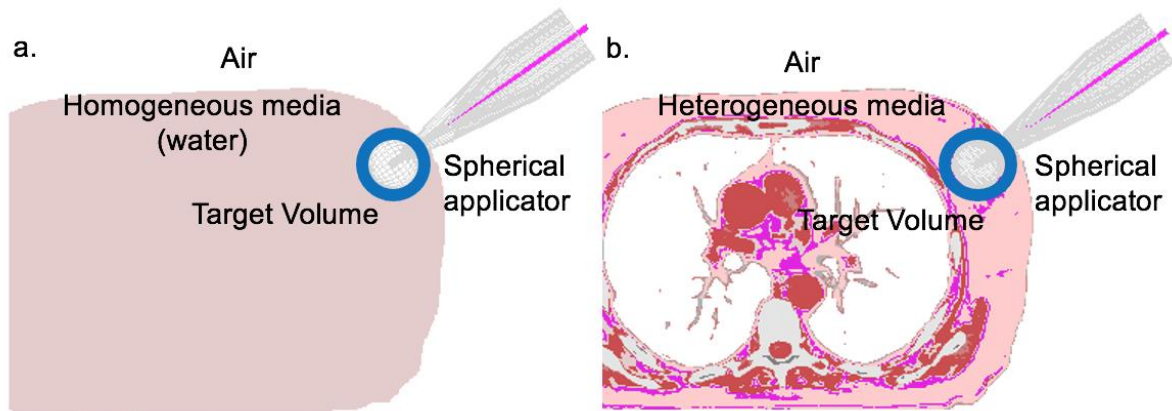


Figure 2-14. The simulation setups. The modeled spherical applicator is placed within the tumor bed in the a. homogeneous patient geometry and b. heterogeneous patient geometry. The blue circle describes a cross-section of the 1 cm defined target volume.

2.9.3 Effects of Geometric errors

Effects of geometric errors on the absorbed dose distributions were investigated by introducing a 2 mm or a 5 mm air or blood interface between the applicator and the tumor bed. While the air was created using information from the data provided by the Geant4 toolkit, elemental composition and density data from ICRU report 46 was used to model the blood ⁵⁶. Setups with air or blood interface included are henceforth referred to as error setups.

Since a realistic air gap or blood interface is only possible to observe from CT images obtained either from intraoperative or postoperative CT images ^{32,33}, the gap or interface in this work is assumed to be a thin layer surrounding the surface of the applicator, as illustrated in **Figure 2-15**. The 2 mm and 5 mm air gaps or blood pooling were created on the .g4cdcm files containing the cavity. The algorithm used is the same as the algorithm utilized for creating the cavity. The radius of the spherical part of the cavity was set to 2 mm and 5 mm larger than the initial radius of the cavity with

the material and the density of the voxels was set to be air or blood. **Subfigure 2-15a** depicts the visualization of the blood interface presenting between the applicator surface and the tumor bed. For all treatment configurations, the position of the applicator is presumed to be fixed within the cavity. Thus, the gap is created by overriding materials and densities of the assumed layer with air or blood of the examined thickness. Clinically, this is perhaps the situation where the size or diameter of the tumor bed is larger than the applicator used ³⁰.

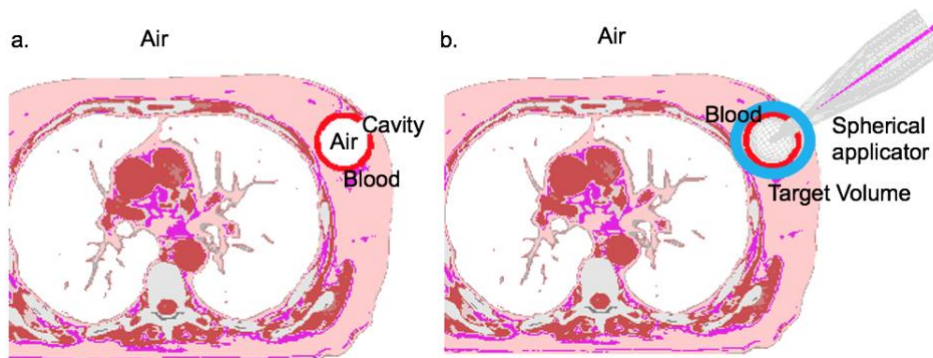


Figure 2-15. Visualizations of the 5 mm blood gap (red circle) a. surrounding the cavity and b. surrounding the surface of the spherical applicator. The blue circle represents the defined target volume.

The pre-operative CT files with the cavity included (the .g4cdcm files) were modified to incorporate air or blood. The modified information was stored as new files with the extension of .g4bdcm. In this work, all simulations to investigate the effect of fluid or air gap were performed using the .g4bdcm files. The magnitude of the impact and its extent on the absorbed doses were quantified by extracting and analyzing the dose profiles of each simulated error setup. The results of the error setups were compared with that of the reference setup. The reference setup is the setup without the air or blood gap between the applicator and the tumor bed, as described in **Subfigure 2-14b**. The percentage dose difference (%) between the selected data points of the dose profiles was determined using the following equation,

$$\text{Relative dose difference (\%)} = \frac{D_{\text{with_air/blood_gap}} - D_{\text{without_air/blood_gap}}}{D_{\text{without_air/blood_gap}}} \times 100\% \quad (2-16)$$

where $D_{without_air/blood_gap}$ represents the absorbed dose in the ideal treatment conditions, without air or blood gap interface, and $D_{with_air/blood_gap}$ is the absorbed dose when air or blood gap is present between the applicator surface and the tumor bed. Since the dose is prescribed at the applicator surface, the relative dose differences for all setups were also calculated from the applicator surface ³⁰.

2.9.4 Analysis of the DVH

The DICOM-RT structure was imported into the MATLAB platform using the Computational Environment for Radiotherapy Research (CERR) software ⁶⁴. The spatial coordinate (x,y,z) of each OAR was extracted. In this work, the OARs considered are the left breast, left lung, heart, and right lung. The 3D matrices of the coordinates data were then resampled and cropped, such that all the coordinate matrices had the same dimension as the CT images used for the MC simulations. The doses of each OARs were subsequently extracted from the resulting dose distributions using the spatial coordinate data as the boundary. Since there is no coordinate data for the target volume (the target volume was not contoured explicitly), the dose for the target volume was retrieved by extracting coordinate data of a 1 cm spherical shell surrounding the applicator on the obtained dose distributions (**Subfigure 2-14b**). This is achieved by generating a 5.5 cm spherical volume that is concentric with another 3.5 cm spherical volume. Dose Volume Histograms (DVHs) were then computed using the resulting dose data points of the target volume and the other OARs.

While the dosimetric consequences of heterogeneities on the absorbed dose delivered to the target volume and each OARs were determined by comparing the DVHs of the heterogeneous CT with the DVHs of the modified homogenous patient CT, the dosimetric implications of the presence of air or blood gap on the absorbed dose distribution were quantified by comparing the DVHs of the patient heterogeneous geometry with and without the presence of air gap or blood interface of different thicknesses in the treatment setups. The 1 cm target volume of the error setups was

generated as the target volume of the reference setup, as previously described. Maximum dose (D2%), minimum dose (D98%), median, and mean absorbed doses were the variables used to compare the DVHs derived for the various simulation setups.

2.10 Dose uncertainty calculations

As previously mentioned, the simulation accuracy represented by the dose uncertainty depends on the number of particle used in the simulations. According to Chetty *et al.*⁶⁵ and Tyagi *et al.*⁶⁶ the number of particles needed to achieve a reasonable accuracy are about 10^8 - 10^{10} particles. In this work, the absorbed dose distribution within the patient geometry for the heterogeneous and homogeneous CTs were simulated with a total of 11.6×10^{10} primary photons tracked through the geometry. For the evaluation of the impact of the geometric errors, the number of particles used in the simulations are 6.4×10^{10} particles. The dose uncertainty is estimated with the *history by history* methods and is calculated according to the following equations⁶⁷,

$$s_x = \sqrt{\frac{1}{N-1} \left(\frac{\sum_{i=1}^N X_i^2}{N} - \left(\frac{\sum_{i=1}^N X_i}{N} \right)^2 \right)} \quad (2-17)$$

Where s_x is the uncertainty of the scored dose for the voxel, N is the total number of histories, X_i is the scored dose during the i th history.

The dose uncertainty was also calculated as the mean uncertainty values of the all voxels with a criteria that only voxels that receive 50% of the maximum dose are considered in the calculation⁶⁸.

2.11 Data Processing analyses

The CT data for the MC simulations and the results of the MC dose calculations were modified and analyzed with MATLAB R2018a (Mathworks Inc., Natick, MA, USA).

3 RESULTS

3.1 Effect of volume overlapping

Figure 3-1 shows a comparison of the depth dose curves of the homogeneous CT and the water phantom. The average percentage difference between the depth dose curve is 0.36%. The difference increased to 23% if the cavity was not included in the modeled CT geometry. The depth dose curves of all simulated configurations were normalized to the maximum value of the central axis dose from the surface of the applicator.

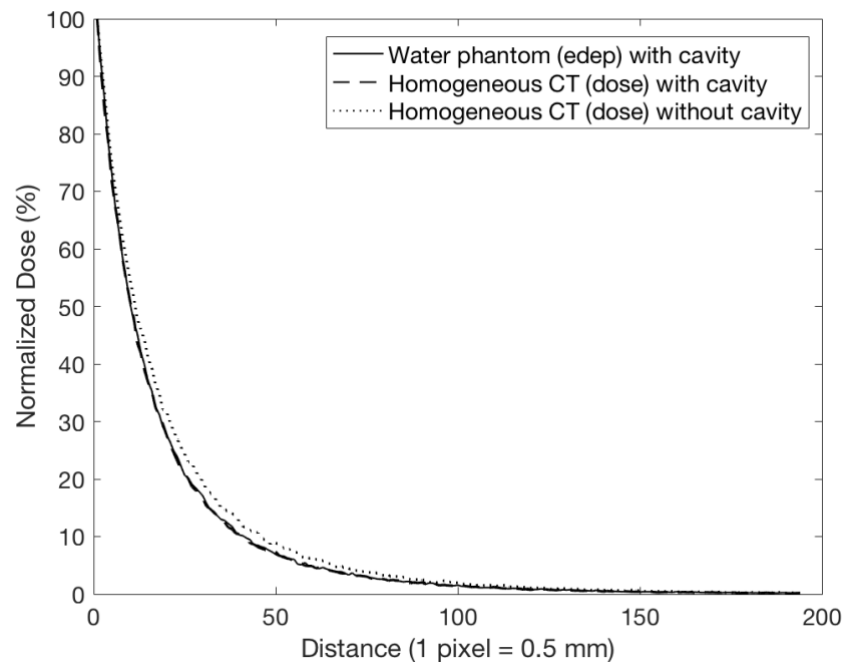


Figure 3-1. Comparison of depth dose curves in patient homogeneous CT and in water phantom for the 3.5 cm spherical applicator.

3.2 Applicator position and orientation

3.2.1 The PrimaryGeneratorAction

Figure 3-2 demonstrates the geometrical model of the 3.5 cm spherical applicator and the trajectories of 100 photon particles generated by the algorithm before and after the initial particle position and orientation in the *PrimaryGeneratorAction* of the source

model was corrected. The simulations were performed in a water phantom. The applicator in both configurations was translated to 50 mm in the x and y axes and rotated at an angle of 315 degrees about the z-axis. The translation and rotation enacted to the spherical applicator in **Subfigure 3-2a** were not applied to the initial conditions of the primary photon particles in the *PrimaryGeneratorAction* class of the source model, such that the trajectories of the particles were not valid. The position of the primary particles remained in its initial position and orientation, which was defined at (0,0,0). In **Subfigure 3-2b**, the trajectories of 100 photons were modeled correctly after implementing the correction.

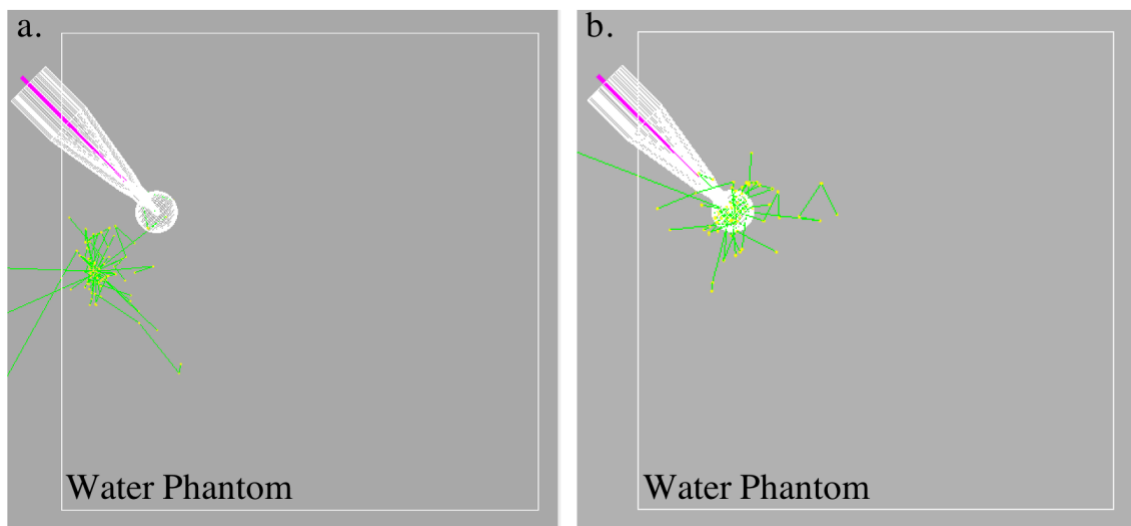


Figure 3-2. Visualization of the path of the 100 primary photon particles that were generated by the algorithm, a. before correction, b after correction to the *SteppingAction* implemented.

3.2.2 The *SteppingAction*

The dose distributions for the 3.5 cm spherical applicator in a water phantom before and after the consideration of particle translation and rotation to the scoring conditions in the *SteppingAction* class of the algorithm are shown in **Figure 3-3**. **Subfigure 3-3a** depicts the dose distribution that is incorrectly modeled. **Subfigure 3-3b** describes the dose distribution on the transverse plane for the 3.5 spherical applicator after the

translation and rotation applied. The applicator shank is modeled by considering the cylindrical part of the applicator. The cavity was not included in this simulation because the aim was to check if the implemented code was valid for the simulated configurations.

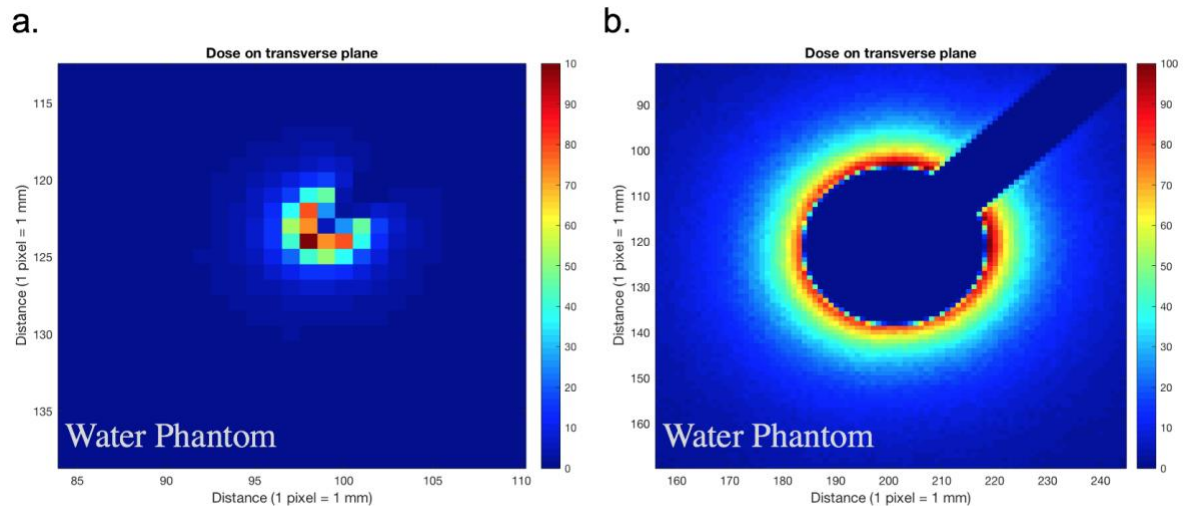


Figure 3-3. The calculated central axis dose plane for the 3.5 spherical applicator before and after the correction applied in the *SteppingAction* class of the algorithm.

3.3 Visualization

Figure 3-4 illustrates the new feature added to the GUI for the INTRABEAM source model. The added feature make it possible to visualize the reconstructed patient geometry and to assess the position of the spherical applicator within the patient geometry. Additionally, it also offers the possibility to conduct the absorbed dose calculation and to create a cavity. The newly added features in the menu are the *Patient* (to build patient geometry, to move the reconstructed patient geometry in the x, y, and z-axes, and to create a cavity) and *SteppingAction* (to calculate the absorbed dose within the patient geometry). The added new menus are presented in **Figure 3-4**.

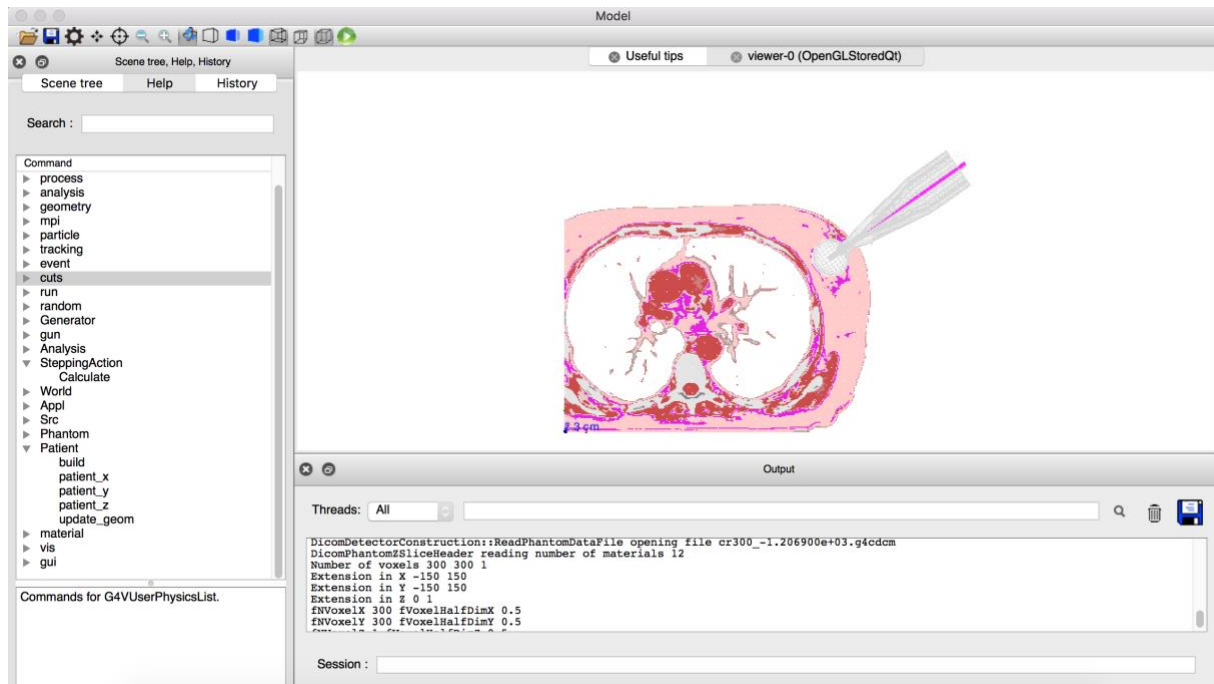


Figure 3-4. The updated GUI of the INTRABEAM source model. The left panel of the GUI shows the added features associated with the geometry of the patient and the scoring functionality.

It is possible to conduct a simulation through a command window, session box, or script, as in the previous version of the algorithm. However, the script approach is preferable because it is fast, and the visualization of the detector components or simulated configurations is no longer necessary. The script consists of a set of commands added to the GUI menus. Following is a sample set of commands to perform a simulation with 100 photon particles. All the commands associated with the patient's geometry were of the *Patient* and the *SteppingAction* menus added in the GUI. The script can be executed from the terminal window.

Script 1: Commands to calculate the absorbed dose within a patient geometry.

```
#Particle generator with VSM
/Generator/particle_source 2
#To build patient geometry, to set its position within the reference coordinate system
/Patient/build 001
/Patient/update_geom
/Patient/patient_x 150 mm
/Patient/patient_y 150 mm
```

```

/Patient/patient_z 116.5 mm
/Patient/update_geom
#To build the applicator, to set its positions within the patient volume
/Apl/applicator 235
/Apl/update_geom
/Apl/app_x 260 mm
/Apl/app_y 170 mm
/Apl/app_z 116.5 mm
/Apl/rot_z 215. deg
/Apl/update_geom
# To compute the absorbed dose
/SteppingAction/Calculate 5
#/Apl/update_geom
/run/beamOn 100

```

The following script describes the steps to generate the cavity. As mentioned in the preceding section, reconstructing the patient geometry should be instantiated before creating the cavity. Executing the script is via the terminal window using the compiled code (./Model) followed by the script file.

Script 2: Command to create a cavity

```

# To build the patient volume
/Patient/build 001
/Patient/update_geom
# To create a cavity for the 3.5 cm spherical applicator
/Patient/create_cavity 235

```

3.4 Effect of heterogeneities on dose distributions

3.4.1 The dose profiles

Figure 3-5 shows the dose distributions in the homogeneous and heterogeneous patient geometries. The dose distributions for both configurations were normalized to a 20 Gy prescribed at the applicator surface. The maximum dose with the spherical applicator is at the applicator surface ⁵⁷. The dose distribution for the homogenous patient geometry is almost symmetrical due to the uniform density of the water in the patient geometry ²³. However, an exception was observed in the area near the applicator stem. This area is outside the patient volume and consists of air. Air has a

small density value compared to water (**Subfigure 3-5a**). Conversely, dose distribution for the heterogeneous CT is observed asymmetrical because of the varied density of the surrounding constituent tissue materials (**Subfigure 3-5b**). Even though the patient tissues are complex and distributed irregularly, it's possible to evaluate the asymmetrical behavior of the dose distribution from the dose profiles extracted from a defined rectangular area near the central axis of the applicator. The tissues covered in this area are glandular breast tissue, adipose tissue, water, muscle tissue, rib, air, and lung.

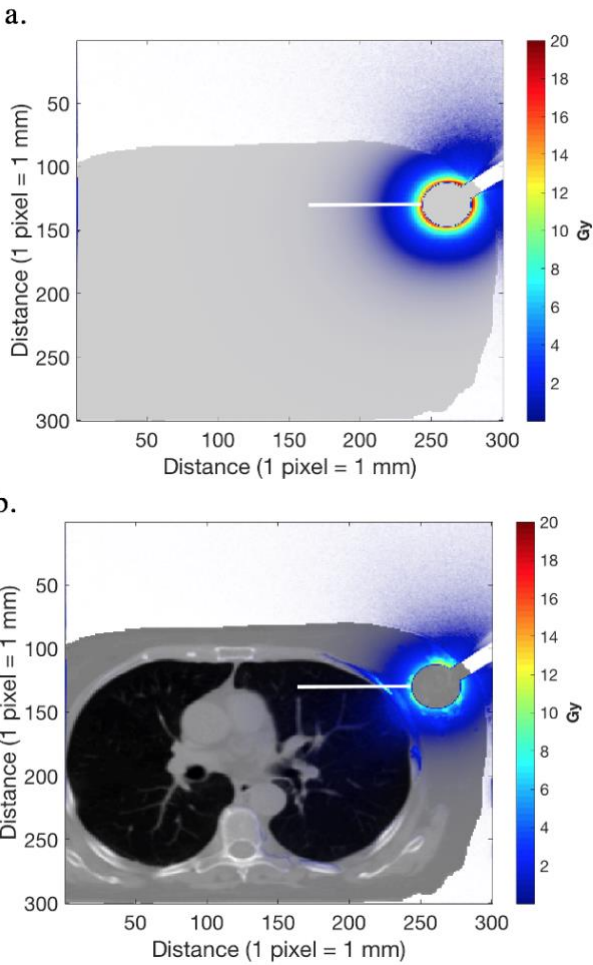


Figure 3-5. Dose distributions in a. homogeneous patient geometry and b. heterogeneous patient geometry superimposed on a CT image of the corresponding slice ²³.

The lateral dose profiles in the homogenous and heterogeneous CTs extracted from the rectangular area are presented in **Figure 3-6**. The profiles are normalized to a 20 Gy prescribed at the surface of the applicator. The compared profiles were retrieved from the surface of the applicator to a depth of 80 mm. The relative deviation between the dose data points of the profiles was computed and used to quantify the difference between both dose values. The formula used to calculate the absorbed dose deviation is presented in equation (2-15) on page 52.

The dose profile for the homogeneous CT is steep and decreases rapidly as the distances from the applicator surface increase, while the dose profile of the heterogeneous CT fluctuates with depth and depends on the structures that the X-ray radiation passes through and their distances from the surface of the applicator (**Figure 3-6**). The maximum absorbed dose values at the applicator surface in the heterogeneous and homogeneous CT are 9.88 Gy and 15.35 Gy, respectively. The absorbed doses of the heterogenous CT were reduced further after penetrating the adipose and glandular breast tissues in the left breast. However, the presence of the muscle and the rib alters the descending trend of the heterogeneous profile. The presence of the muscle tissue and rib increases the absorbed doses with the maximum dose increase at a distance of 21 mm from the applicator surface. The rib escalates the dose value to approximately 7.37 Gy, whereas the absorbed dose at this depth for the homogeneous CT decreases to about 1.48 Gy. The absorbed dose deposited in the lung of the heterogeneous CT indicates low dose values compared to the dose values in the homogeneous CT. However, the doses delivered to the lungs and the heart of the heterogeneous CT show a significant dose increase (**Subfigure 3-6b**). Nevertheless, this increase could not be observed in **Figure 3-6** as the lateral dose profiles presented did not include the proportion of the heart and right lung. Dose escalation in these organs could be evaluated from the obtained DVHs.

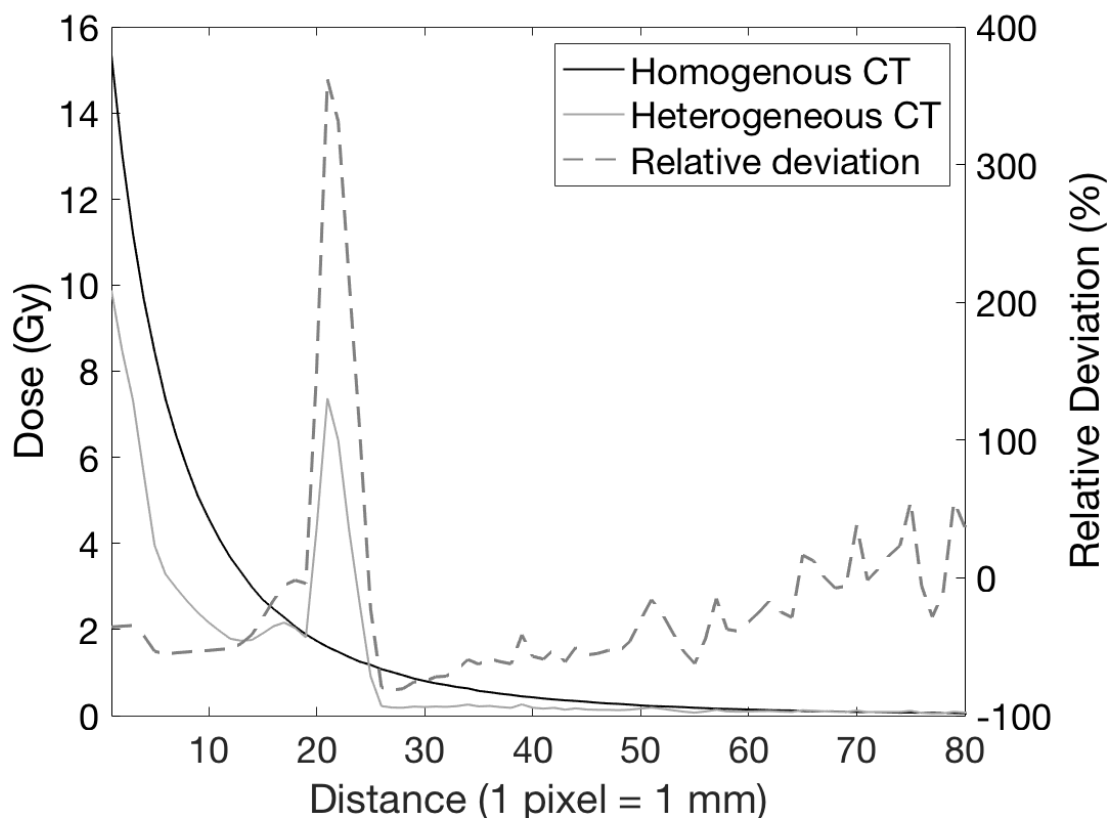


Figure 3-6. Dose profiles for the homogeneous and heterogeneous patient geometries. The dose profiles are obtained from the selected area shown in **Figure 3-5**²³. A bone interface (rib) appears 20 cm from the applicator surface.

3.4.2 The DVHs of the homogeneous vs. the heterogeneous CTs

As mentioned in the preceding section, the target volume is not contoured, such that no spatial coordinate data are available in the DICOM structure data to create the boundary for the target volume. The target volume was then extracted directly from the dose data generated by the MC simulation. **Figure 3-7** shows the generated dose data points and corresponding dose distribution of the target volume retrieved from the central axis of the dose slice. For the homogeneous CT, the shape of the target volume is identical to the heterogeneous CT. The difference is in the absorbed dose values within each voxel of the assumed geometry.

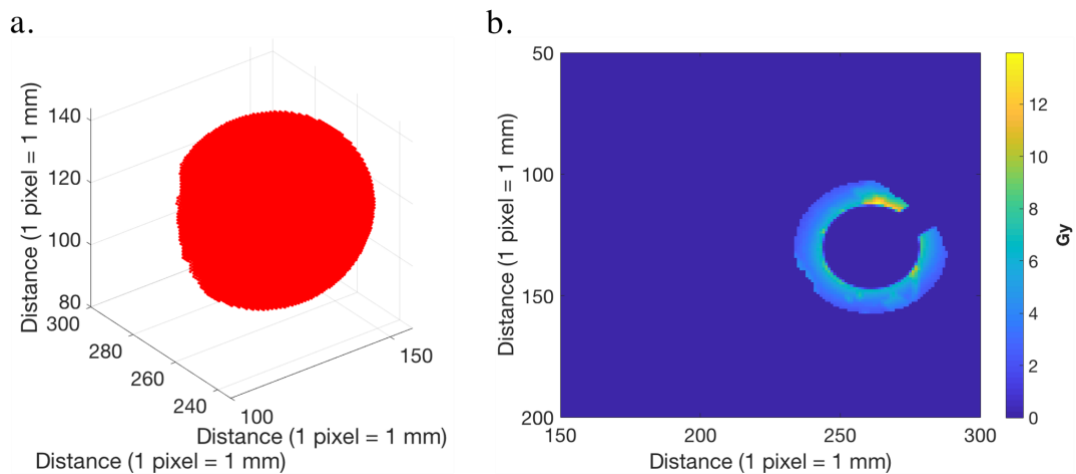


Figure 3-7. a. The dose points of the extracted target volume (left) and b. its central axis dose plane (right).

The DICOM structure data provided the spatial coordinate of the left breast. Because the target volume was extracted from the left breast, the target volume was then excluded from the left breast. (**Figure 3-8**) shows the generated dose data points of the rest of the left breast (minus the target volume) of the heterogeneous patient CT. The shape of the left breast is also identical for the homogenous and heterogenous patient geometries.

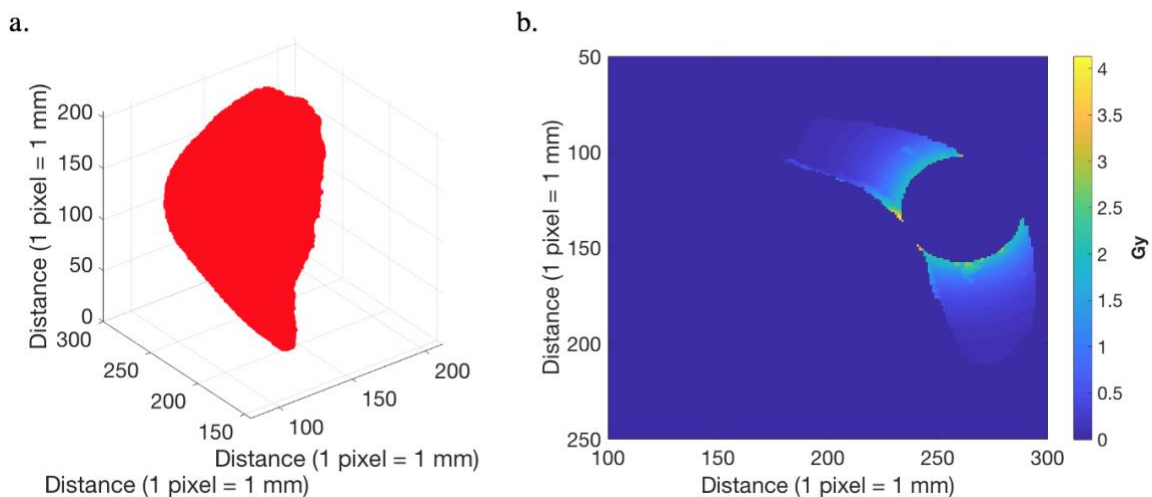


Figure 3-8. a. The dose points of the left breast minus the target volume and b. dose distribution at the central axis.

Figure 3-9 compares the DVHs of the target volume and the OARs of the homogeneous and heterogeneous patient geometries. The DVHs of the target volume and the rest of the left breast were calculated using the dose data points of the target volume and the left breast shown in **Figure 3-7** and **Figure 3-8**. The resulting dose data points for the other OARS can be seen in APPENDIX (**Figure 7-1**, page 115). In accordance with the result shown in **Figure 3-6**, the overall doses in the target volume and the left breast are higher for the homogeneous CT. The absorbed dose of at least 2% of the target volume (D2%) of the homogeneous patient geometry is 16.26 Gy with a mean dose value of 8.17 ± 3.56 Gy, while for the heterogeneous CT, the D2% and the mean dose values of the volume are 9.33 Gy and 4.15 ± 1.91 Gy, respectively. For the rest of the left breast (the whole breast minus the target volume), the D2% and the mean dose values of the rest of the left breast of the homogeneous CT are 3.57 Gy and 0.64 ± 0.86 Gy, which are higher than the values of the left breast of the heterogeneous CT which are 2.01 Gy and 0.392 ± 0.604 Gy).

The doses delivered to the other OARs for the heterogeneous CT are higher than in the homogeneous CT. Although the D2% value of the left lung of the heterogeneous CT is lower than the value of the homogeneous CT, its mean, median, and D98% values of the OARs demonstrate higher absorbed dose values relative to the homogeneous CT. The heart and right lung of the heterogeneous CT also received higher absorbed doses compared to the heart and right lung of the homogeneous CT. The consideration of tissue heterogeneities also affects the proportion of the right lung receiving the radiation dose. The DVHs of this organ in the homogeneous and the heterogeneous setups revealed the reduced proportion of the right lung exposed to radiation doses. Details of the absorbed doses in target volume and the other OARs of each setup are presented in **Table 3-1**.

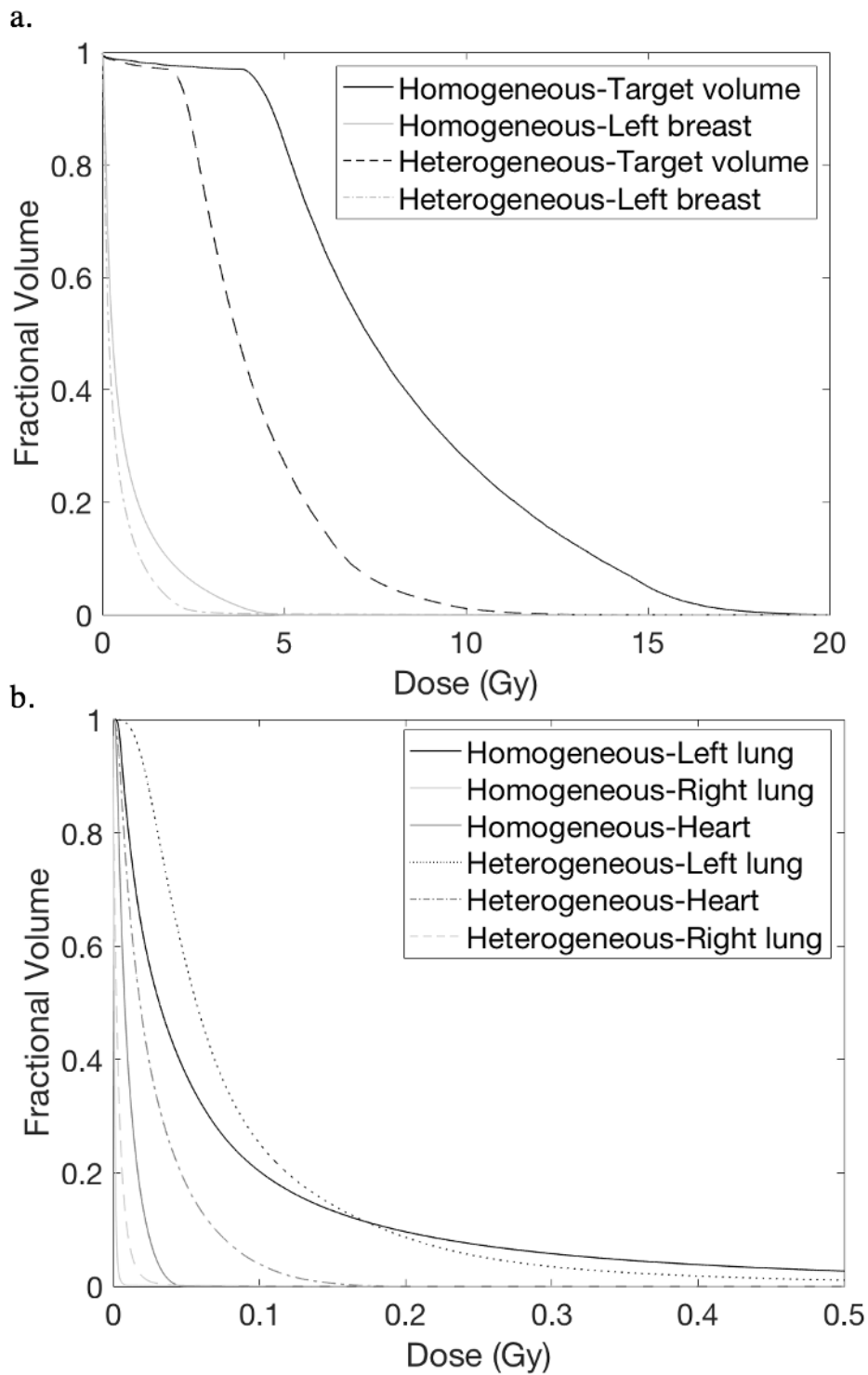


Figure 3-9. DVHs in the patient geometry for 20 Gy prescribed at the applicator's surface for a. the target volume and left breast, b. heart, left and right lungs. Calculations were conducted for the homogeneous CT (solid lines) and heterogenous CT (dotted lines) ²³.

Table 3-1. The absorbed doses in the target volume and other OARs for the homogeneous and heterogeneous patient CT geometries ²³.

Organs	Homogeneous CT (Gy)				Heterogeneous CT (Gy)			
	D2%	D98%	Median	Mean ± STD	D2%	D98%	Median	Mean ± STD
Target volume	16.26	1.403	7.29	8.17±3.56	9.33	0.665	3.70	4.15±1.91
Left breast	3.57	0.0303	0.272	0.64±0.86	2.01	0.016	0.174	0.392±0.604
Left lung	0.595	0.0039	0.032	0.083±0.162	0.383	0.0129	0.057	0.088±0.101
Heart	0.035	0.0016	0.008	0.011±0.009	0.119	0.0022	0.018	0.0292±0.0295
Right lung	0.004	0.00	0.001	0.0012±0.004	0.019	0.00	0.003	0.005±0.007

3.5 Effect of geometric errors on dose distributions

3.5.1 Air gap

Figure 3-10 shows the impacts of the air gap of different thicknesses on the absorbed dose distributions. All the calculated dose values were normalized to the 20 Gy prescribed at the applicator surface. In general, the presence of the air gap alters the dose distributions. The most notable effect was near the applicator surface. However, it was difficult to evaluate the impact on the absorbed doses in the target volume and the other OARs directly from the absorbed dose distributions (**Figure 3-10**). Hence, we compare the lateral dose profiles of the error and reference configurations. The lateral dose profiles of all setups were extracted from the applicator surface to a depth of 75 mm. The effect of the air gap was determined by evaluating the percentage dose deviation of the compared dose profiles. The equation used to calculate dose deviation is the equation 2-16 on page 54. The region covered in this area includes air (the gap), glandular breast tissue, adipose tissue, water, rib, and lung.

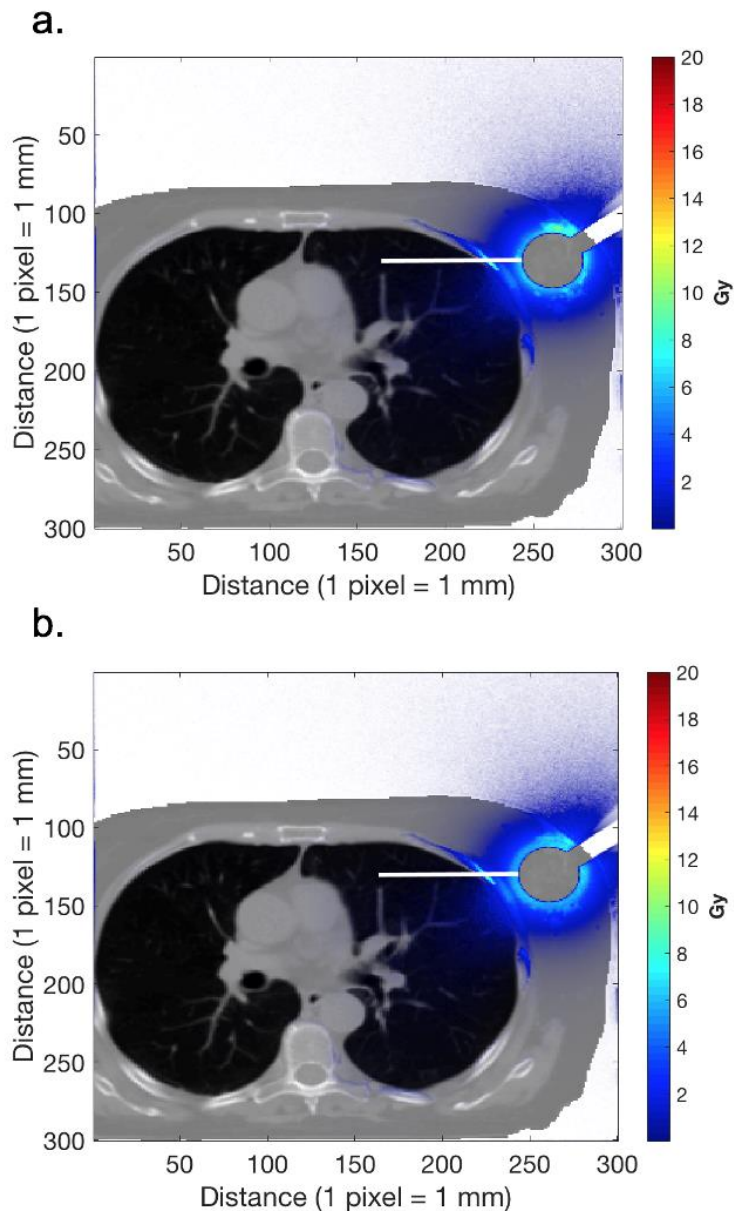


Figure 3-10. Dose distributions in the patient geometry superimposed on the CT axial slice for simulations in the presence of a. 2 mm air gap and b. 5 mm air gap between the applicator surface and tumor bed.

Figure 3-11 presents the lateral dose profiles for the reference and error setups obtained from the small rectangular area of the corresponding dose distribution. The presence of an air gap resulted in lower dose values near the applicator surface. The absorbed dose values at the prescription depths because of the 2 mm and 5 mm air

gap are 5.51 Gy and 5.06, respectively. Meanwhile, the absorbed dose value of the reference setup is 9.89 Gy. However, the absorbed doses of the error configurations increased after the radiation passed through several voxels of the glandular breast and adipose tissue within the left breast. The most notable effect of the air gap on increasing the doses relative to the reference setup was at 4 mm depth for the 2 mm air gap and 5 mm depth for the 5 mm air gap, respectively (**Subfigure 3-11b**). The absorbed doses at these depths are 5.97 Gy and 5.04 Gy. When the depths exceed 21 mm, both the lateral dose profiles of the error setups show a descending trend. This trend occurred when the radiation dose passed through several voxels of the rib (**Subfigure 3-11b**). The presence of the 5 mm air gap has a more significant effect on decreasing the dose compared to the 2 mm air gap at the same depth (21 mm). The results suggested that the extent of the air gap effects depends on the thickness of the air gap used and their distances from the applicator surface. Since the dose profiles are presented only for depths up to 30 mm from the applicator surface, the impacts on the absorbed doses received by the heart and both lungs were assessed from the computed DVHs.

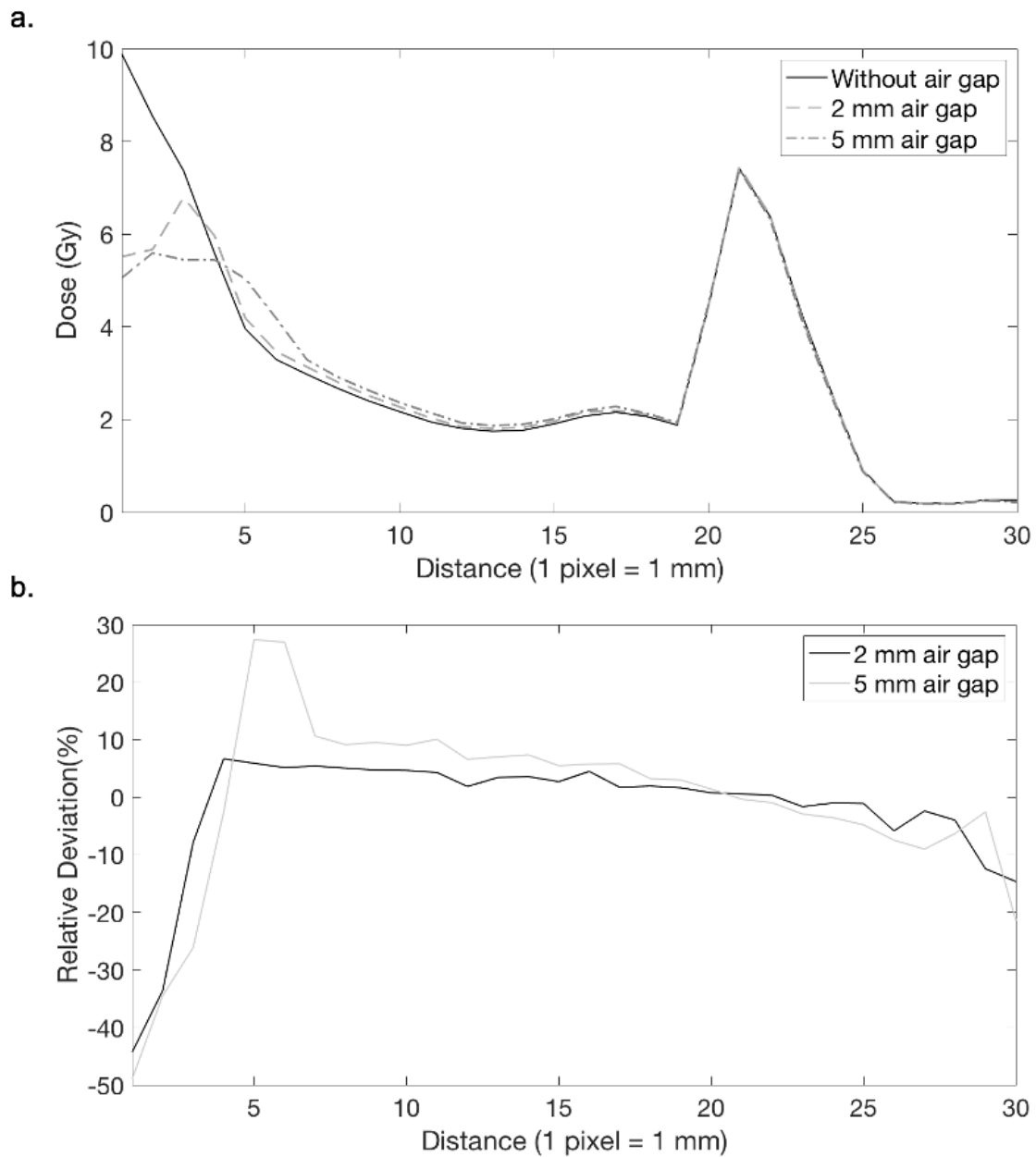


Figure 3-11. Dose profiles a. without and with the presence of the 2 mm and 5 mm air gaps. b. The respective relative deviations. The dose profiles of each setup were extracted from the applicator surface.

Comparisons of DVHs of the target volume and the OARs between the reference and the error setups are shown in **Figure 3-12**. The presence of the air gap modifies the absorbed dose distribution in the target volume. The target volume of the error setups

received a higher dose than the target volume of the reference setup (**Subfigure 3-12a**). The D2% and the mean dose value of the 2 mm air gap setup are 7.31 Gy and 4.0069 ± 1.5470 Gy, while for the 5 mm air gap setup the values are 6.44 Gy and 4.0215 ± 1.4040 Gy, respectively. The D2% and the mean dose value of the target volume of the reference setup are 9.43 Gy and 4.1821 ± 1.9354 Gy. However, the median dose of the target volume of the error setups shows an increased value (3.77 Gy and 3.98 Gy, respectively) compared to that of the reference setup (3.71 Gy). The left breast of the error setups received a lower dose than the left breast of the reference setup. The left breast of the error setups demonstrates higher D2% values (2.06 Gy and 2.09 Gy, respectively) than the D2% value of the reference setup (2.02 Gy). The mean dose values of the left breast of the error setups are also high compared to the reference setups. The mean dose values of the error setups are 0.3954 ± 0.6138 Gy and 0.3957 ± 0.6204 Gy, respectively, while the value for the reference setup is 0.3929 ± 0.6064 Gy. However, the median dose values of the error setups are lower than the median value of the reference setup. The median dose values of the error setups are 0.1730 Gy and 0.1703 Gy. For the reference setup, the median dose value is 0.1745 Gy.

The absorbed doses in the left lung, heart, and right lung are decreased in the error setups (**Subfigure 3-12b**). The D2% of the left lung for the 2 mm air gap setup is 0.391 Gy, with the median, mean dose, and D98% values are 0.0566 Gy, 0.0880 ± 0.1032 Gy, 0.0102, respectively. The D2% of the 5 mm air setup is 0.3947 Gy. The median, mean dose, and D98% values are 0.0558 Gy, 0.0878 ± 0.1046 Gy, and 0.0101 Gy. This reduction trend is also discovered for the other OARs. Furthermore, we observed that most parts of the left breast and the left lung of the error setups received lower doses than that of the reference setup. The reduction in the absorbed dose is proportional to the size of the gap used. This tendency is also observed in the heart. The right lung received partial irradiation. The emergence of the air gap increased the portion of the right lung exposed to the radiation doses. However, the doses received by the right lung of the error setups are generally less than those in the reference setup. Details of the absorbed doses of the other OARs are presented in **Table 3-2**.

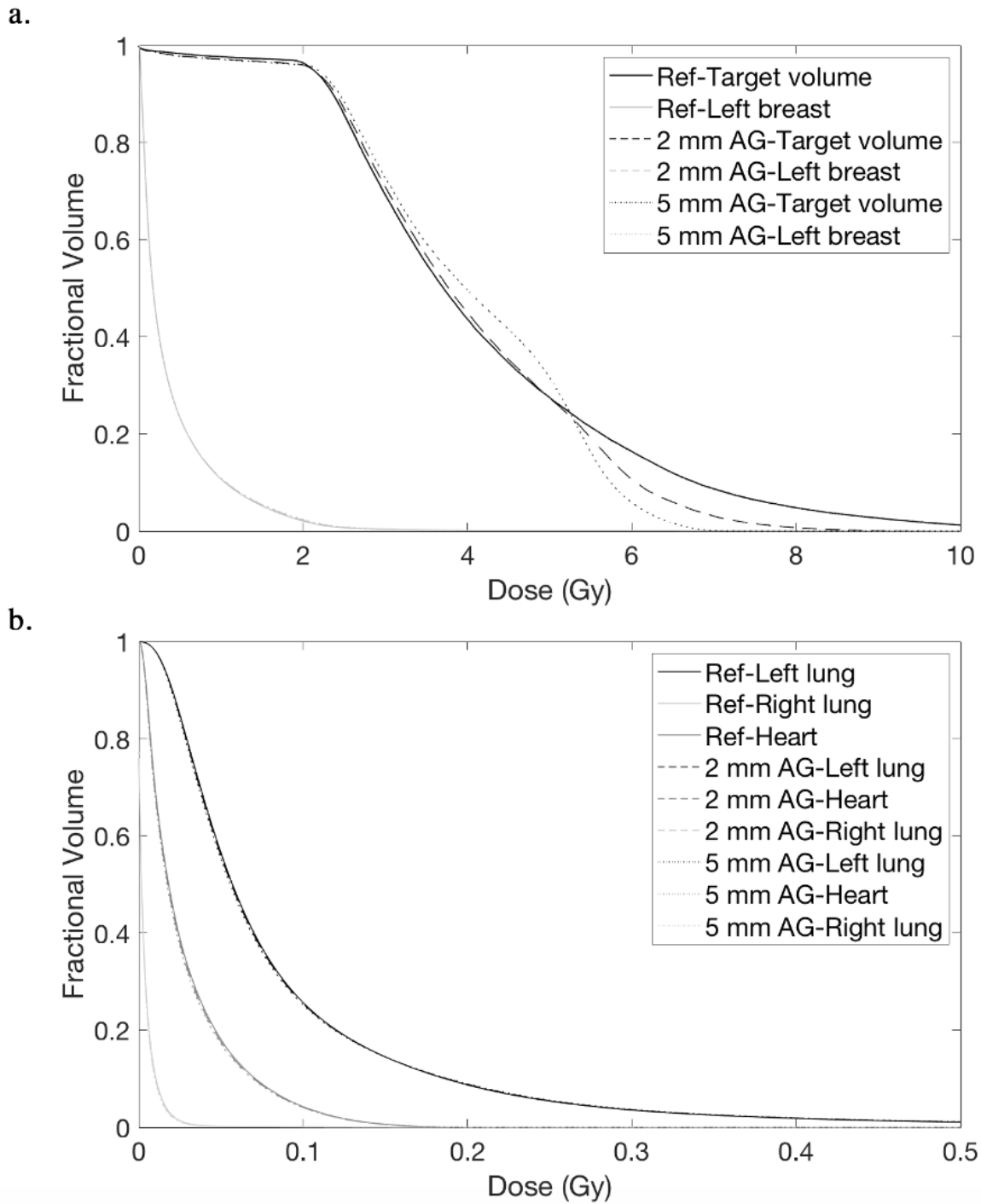


Figure 3-12. DVHs in the patient geometry for a. the target volume and left breast and b. the other OARs for the simulations without the air gap (Ref) and with the air gaps of 2 mm and 5 mm (AG).

Table 3-2. The absorbed dose deposited in the target volume and the other OARs for the simulations with and without the consideration of the air gap between the applicator and tumor bed.

Organs	Without gap (Gy)			
	D2%	D98%	Median	Mean ± STD
Target volume	9.43	0.707	3.71	4.1821±1.9354
Left breast	2.02	0.0156	0.1745	0.3929±0.6064
Left lung	0.3868	0.0103	0.0571	0.0881±0.1021
Heart	0.1219	0.0022	0.0183	0.0294±0.0302
Right lung	0.0220	0,00	0.003	0.0040±0.0080
Organs	2 mm air gap (Gy)			
	D2%	D98%	Median	Mean ± STD
Target volume	7.31	0.42	3.77	4.0069 ±1.5470
Left breast	2.06	0.0153	0.1730	0.3954±0.6138
Left lung	0.391	0.0102	0.0566	0.0880±0.1032
Heart	0.1213	0.0021	0.0179	0.0289±0.0300
Right lung	0.0214	0.00	0.003	0.0040±0.0079
Organs	5 mm air gap (Gy)			
	D2%	D98%	Median	Mean ± STD
Target volume	6.44	0.40	3.98	4.0215±1.4040
Left breast	2.09	0.0150	0.1703	0.3957±0.6204
Left lung	0.3947	0.0101	0.0558	0.0878±0.1046
Heart	0.1209	0.002	0.0174	0.0284±0.0299
Right lung	0.0206	0.00	0.003	0.0039±0.0077

3.5.2 Blood interface

The impact of the blood interface of different thicknesses on the absorbed dose distributions is shown in **Figure 3-13**. The blood interface of varying thicknesses in the

error setups also affects dose distributions, with the effects being most visible near the applicator surface. Assessment of the effects on the target volume and the other OARs was also performed by comparing the lateral dose profiles of a particular region of the 2 mm blood interface and the 5 mm blood interface setups with the lateral dose profile of the reference setup shown with the white rectangular area in **Figure 3-13**.

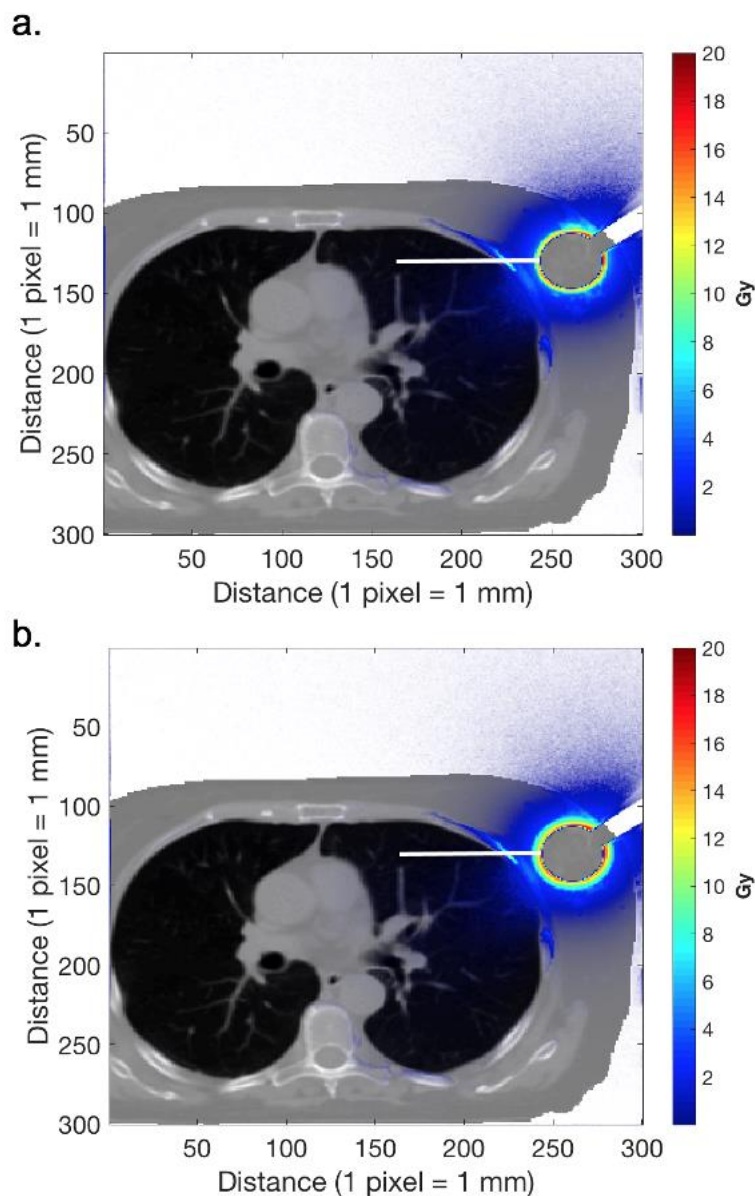


Figure 3-13. Dose distributions in patient geometry overlaid in the CT axial image of a corresponding slice for the simulations with the 2 mm and 5 mm blood present between the applicator surface and tumor bed.

The comparison of the dose profiles and relative dose deviations of the error setups against the reference setup in the presence of the 2 mm and 5 mm blood interfaces are shown in **Figure 3-14**. The absorbed dose values of the error setups at the applicator surface are higher than those of the reference setup (**Subfigure 3-14a**). Regarding the increase, the 5 mm blood interface gives rise to the dose values more significantly than the 2 mm blood interface. The absorbed dose values of the error setups at the surface of the applicator are 13.33 Gy and 14.14 Gy, respectively. The absorbed dose value at the surface of the applicator for the reference setup is 9.89 Gy, as previously stated.

The most prominent impact of the 2 mm blood interface on increasing the dose relative to the reference setup is at the applicator surface, while the 5 mm blood interface has a significant impact at 5 mm depths from the applicator surface (**Subfigure 3-14b**). The absorbed dose value at 5 mm depth from the applicator surface is 7.48 Gy. The 2 mm blood interface has a somewhat greater impact on increasing dose distributions than the 5 mm interface at depths of 7 mm and beyond. The 5 mm blood interface, however, has a greater influence on increasing the dose distributions than the 2 mm blood interface at 19 mm depth near the rib bone and beyond. According to these results, the thickness of the blood interface used and the locations of the investigated organs from the applicator surface determine the magnitude of the blood interface effects on the dose distributions of the target volume and the OARs. The absorbed doses received by the organs located beyond the 30 mm depths were evaluated using the obtained DVHs of these organs.

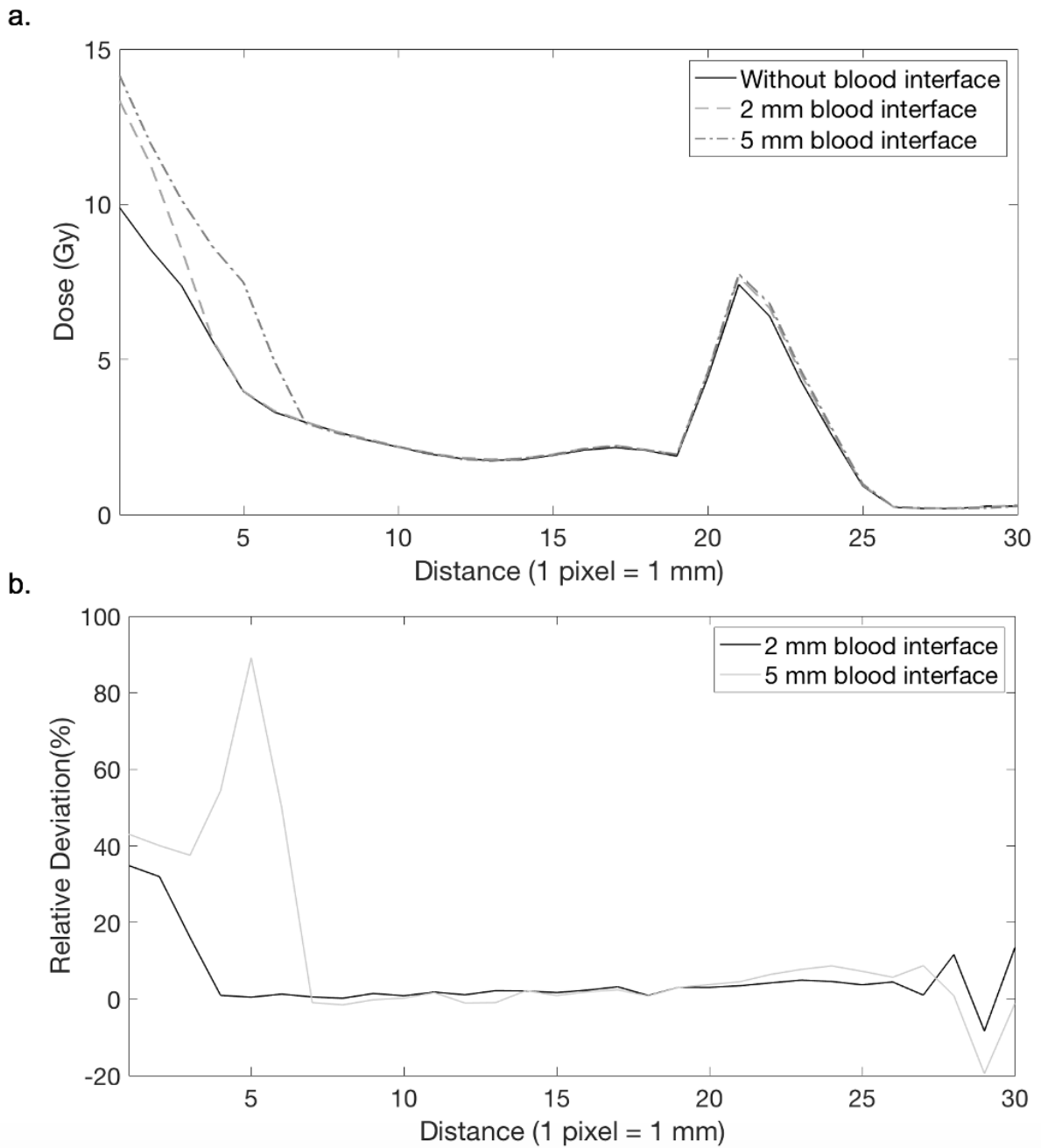


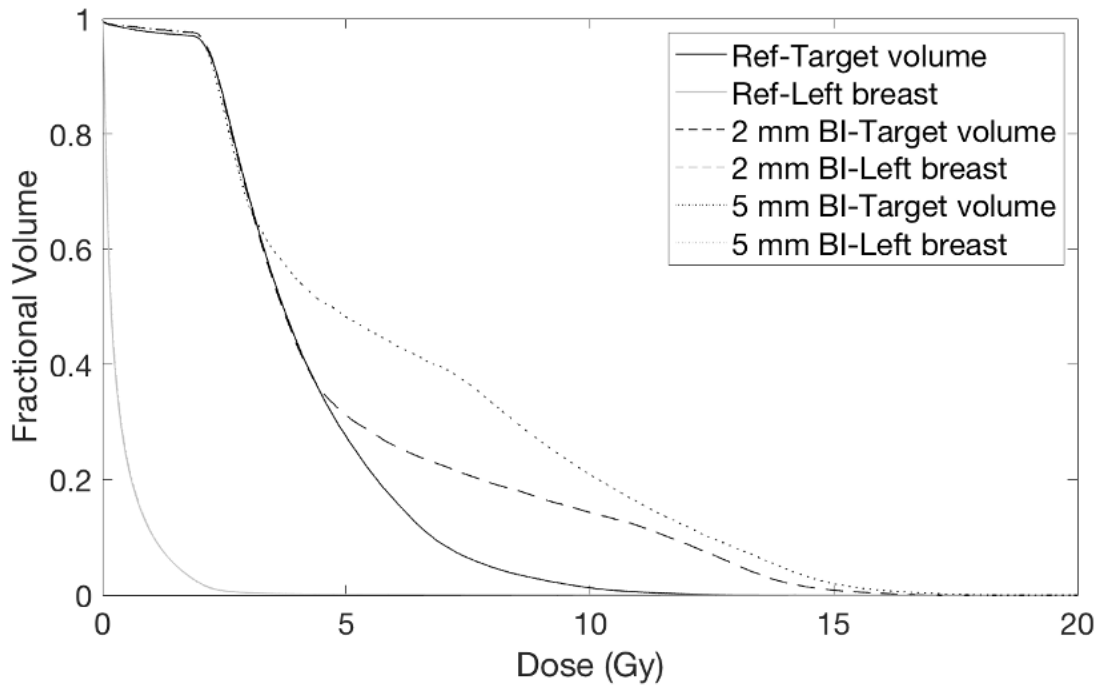
Figure 3-14. Comparisons of dose profiles a. without the presence of blood and in the presence of the 2 mm and 5 mm blood interfaces and b. their relative dose differences.

Figure 3-15 compares the DVHs of the target volume and the other OARs of the simulated treatment setups. The result shows that the overall doses delivered to the target volume and the left breast of the 2 mm and 5 mm blood setups are higher than

that of the reference setup. The D2% and the mean dose values of the target volume of the 2 mm blood setup are 14.10 Gy and 5.1540 ± 3.5279 Gy. For the 5 mm blood setup, the values are 14.99 Gy and 6.2256 ± 4.0389 Gy, respectively. The D2% and mean dose values of the reference setup are 9.43 Gy and 4.1821 ± 1.9354 Gy, respectively. On the other hand, the overall absorbed doses received by the left breast of the error setups are also increased. Even though the D2% of the left breast of the error setups decreased compared to the reference setup, the other dose variables presented in **Table 3-3** increased.

A similar trend was also observed in the left lung and the heart, in which the error setups of these organs received higher doses than the absorbed doses of the reference setup. The D2% of the left lung of the 2 mm and 5 mm blood configurations are 0.3904 Gy and 0.3905 Gy, respectively. The mean and median dose values for the 2 mm blood setup are 0.0895 ± 0.1025 Gy and 0.0585 Gy. The mean dose value of the 5 mm blood setup is 0.0904 ± 0.1022 Gy, with the median dose value of 0.0595 Gy. In contrast, the D2%, mean, and median dose values for the reference setup are 0.3868 Gy, 0.0881 ± 0.1021 Gy, and 0.0571 Gy, respectively. These values are lower than the dose values of both the error setups. The presence of the blood interface increases the dose values of the right lung in the error setups. However, it reduces the proportion of the right lung that receives the radiation doses. **Table 3-3** summarizes the absorbed doses provided to the target volume and the OARs for the compared simulated setups.

a.



b.

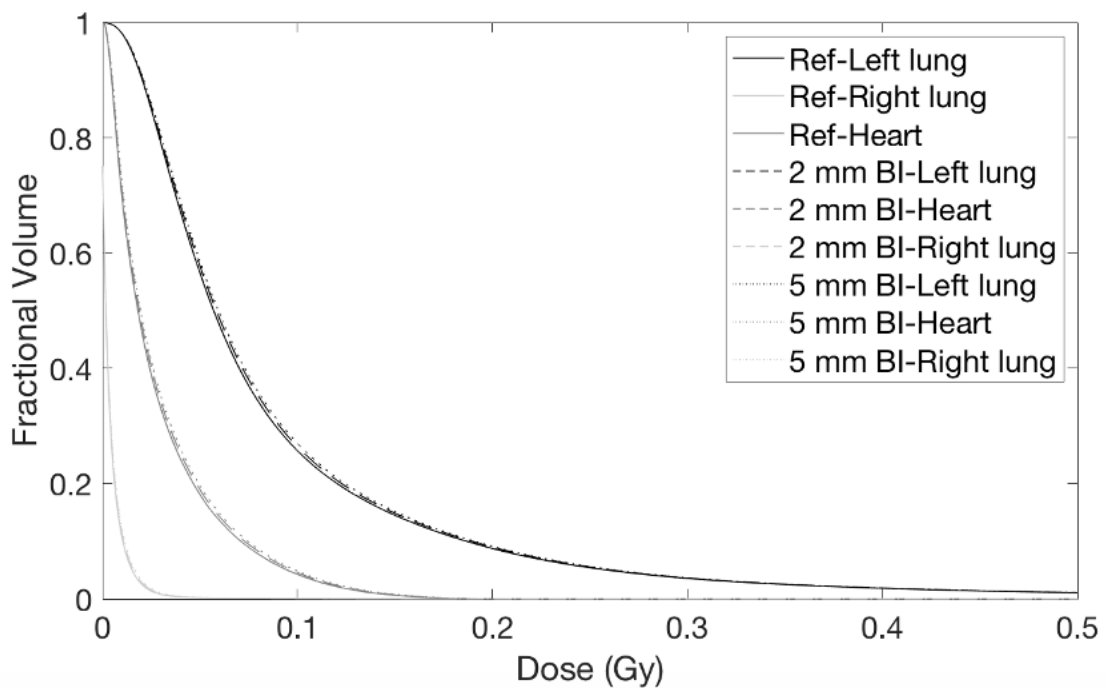


Figure 3-15. DVHs in the patient geometry for 20 Gy prescribed at the applicator's surface for a. the target volume and the left breast and b. the other OARs. Simulations were performed for the reference setup (ref) and the error setups with the presence of the 2 mm and 5 mm blood interfaces (BI).

Table 3-3. The absorbed doses in the target volume and the other OARs for the simulations with and without the presence of blood interface between the applicator surface and tumor bed.

Organs	Without gap (Gy)			
	D2%	D98%	Median	Mean ± STD
Target volume	9.43	0.707	3.71	4.1821±1.9354
Left breast	2.02	0.0156	0.1745	0.3929±0.6064
Left lung	0.3868	0.0103	0.0571	0.0881±0.1021
Heart	0.1219	0.0022	0.0183	0.0294±0.0302
Right lung	0.0220	0,00	0.003	0.0040±0.0080
Organs	2 mm blood gap (Gy)			
	D2%	D98%	Median	Mean ± STD
Target volume	14.10	1.27	3.69	5.1540±3.5279
Left breast	2.01	0.0162	0.1791	0.3969±0.6084
Left lung	0.3904	0.0103	0.0585	0.0895±0.1025
Heart	0.1246	0.0022	0.0190	0.0303±0.0308
Right lung	0.0230	0.00	0.003	0.0042±0.0084
Organs	5 mm blood gap (Gy)			
	D2%	D98%	Median	Mean ± STD
Target volume	14.99	1.39	4.71	6.2256±4.0389
Left breast	2.00	0.0167	0.1832	0.4006±0.6099
Left lung	0.3905	0.0104	0.0595	0.0904±0.1022
Heart	0.1264	0.0023	0.0197	0.0311±0.0313
Right lung	0.0240	0.00	0.003	0.0043±0.0087

3.6 The calculated dose uncertainty

Figure 3-16 presents the calculated dose uncertainty for the homogeneous and heterogeneous CTs as a function of the simulated photon histories. The scored volume for both the setups contained 21 million voxels with the resolution of the calculation grid was 1 mm^3 . The calculated dose uncertainty values for the heterogeneous CT were lower than the values for the homogeneous CT. The simulation of 11.6×10^{10} primary photon particles in the homogeneous CT resulted in a calculated dose uncertainty value of 0.4%. For the heterogeneous CT the calculated dose uncertainty value is 0.35%.

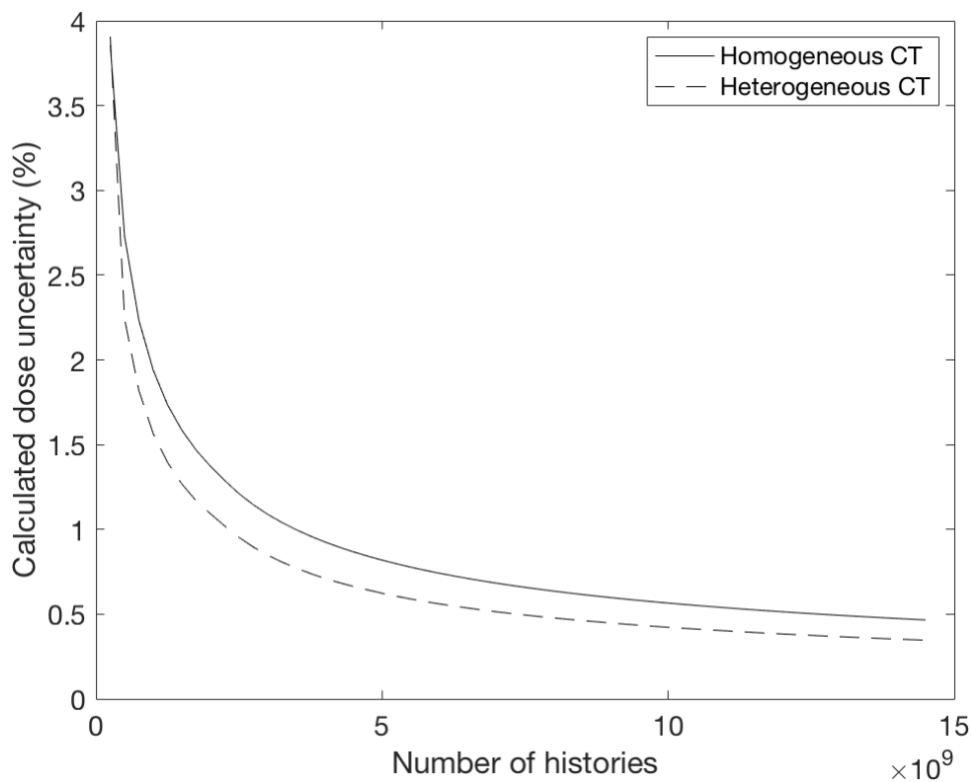


Figure 3-16. Comparisons of the calculated dose uncertainty as a function of the number of primary history for the homogeneous and heterogeneous CTs.

The comparisons of the calculated dose uncertainty for the reference setup (without air gap) and the error setups (with the 2 mm air gap and 5 mm air gap) for the simulated 6.4×10^{10} primary particles are shown in **Figure 3-17**. The calculated dose

uncertainties for the reference and the error setups are 0.68 %, 0.71%, and 0.58%, respectively.

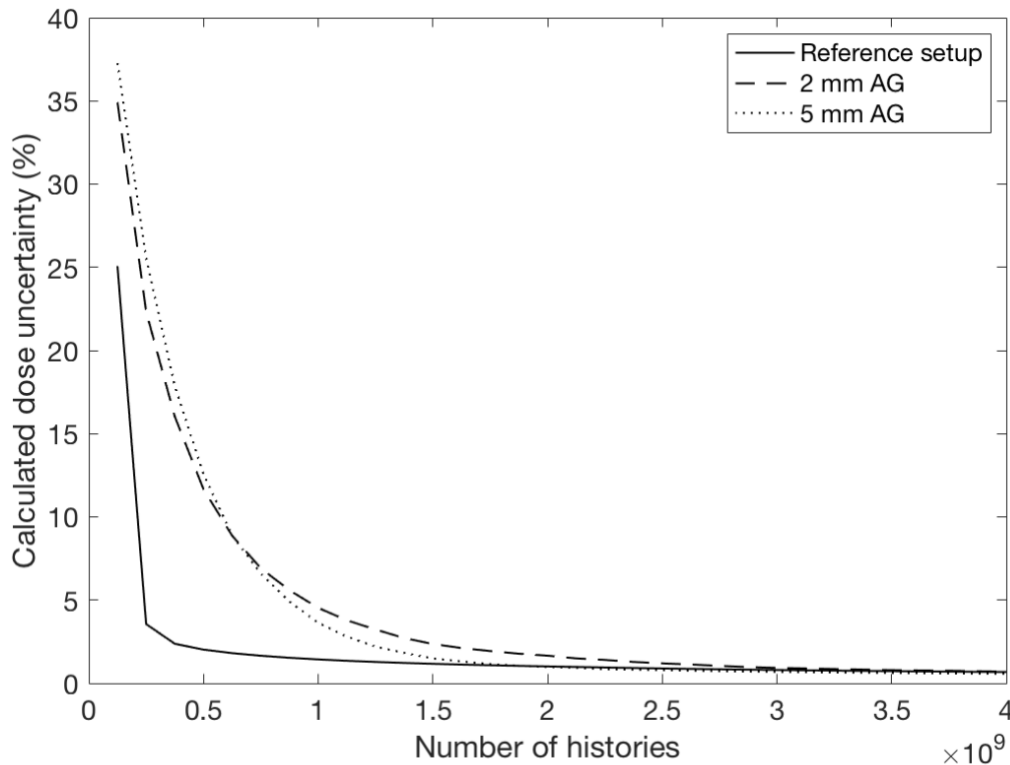


Figure 3-17. Comparisons of the calculated dose uncertainty as a function of the number of primary histories for the reference (without air gap) and the error setups (with the air gap).

Figure 3-18 presents the calculated dose uncertainties for the reference and the errors setups. The presence of the 2 mm blood interface between the applicator and the tumor bed resulted in a calculated dose uncertainty value of 0.71%, while the 5 mm blood interface caused a calculated dose uncertainty of 0.74%.

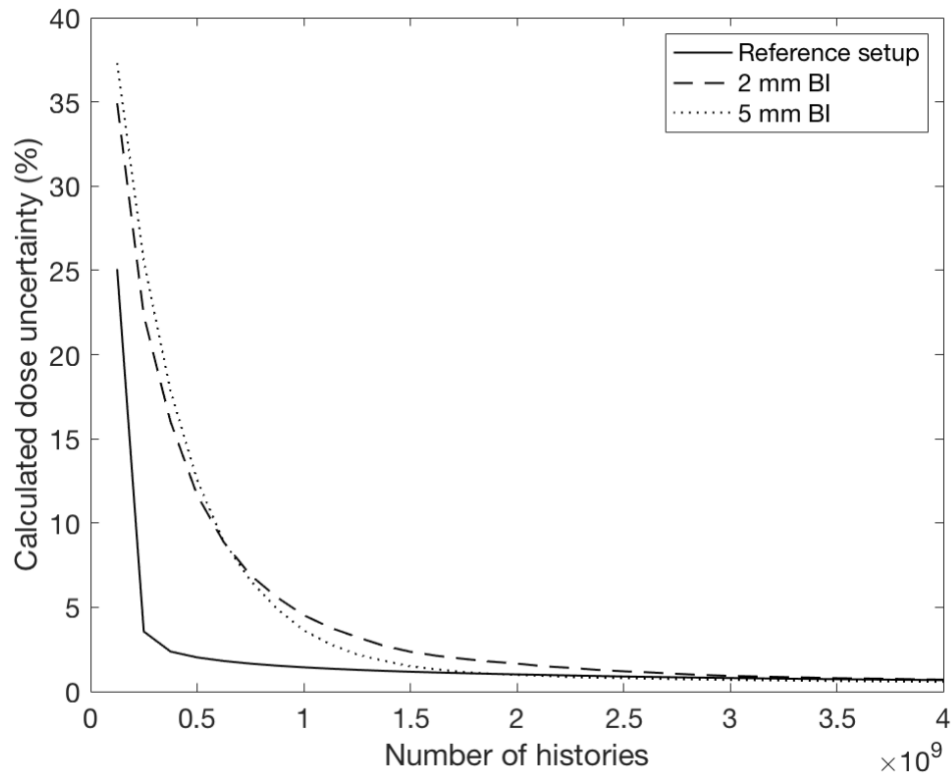


Figure 3-18. Comparisons of the calculated dose uncertainty as the function of the number of histories for the reference and the error setups with the 2 mm and 5 mm blood interfaces.

4 DISCUSSION

Dose prescription in breast IORT with the INTRABEAM device is based mainly on measurements in a water phantom. As such, detailed knowledge of the dose distribution within the heterogeneous patient is largely unknown for a typical IORT treatment. We used an MC dose calculation algorithm developed in-house to investigate the absorbed dose distribution using a pre-operative CT scan of a breast cancer patient. This algorithm allowed us to evaluate the geometrical models of the patient and surgical cavity, assess the position of the applicator within the cavity/tumor bed, perform simulations and generate data on the 3D dose distribution in the patient from the simulated treatment conditions, determine the dose delivered to each organ of interest, and investigate the effect of geometric errors on the dose distributions.

Several aspects of the developed algorithm have been evaluated before simulations with patient CT data were conducted. The first assessed aspect is the volume overlapping caused by the placement of the INTRABEAM source and spherical applicator in the voxelized patient geometry. Visual assessment of the positions of the geometrical models makes use of the GUI (**Figure 3-4**). Our simulation results show that the overlapping has a significant effect on altering the absorbed dose distribution in the patient. Comparisons of the depth dose curves revealed that the overlapping led to a dose difference as high as 23% (**Figure 3-1**). This is perhaps related with particle tracking during the simulation⁵⁰. When a geometry is built, simulation tracks the particle through the geometry. Which volume the particle would traverse next and the distance to this volume are determined by the navigation class of the Geant4. The volume overlapping limits the efficacy of the navigator⁵⁰. We handled the overlapping issue by modeling the cavity in the voxelized patient geometry. The cavity is modeled by removing the CT voxels whose boundaries would intersect the source and spherical applicator. The source and spherical applicator were then placed into the created cavity. The improvement was achieved with the relative dose difference of the depth dose curves between setups was 0.36%. This finding highlighted the importance of modeling and including the surgical cavity in the simulated treatment scenario with the

INTRABEAM source and spherical applicators. Based on these results, all the performed simulations were set with the configuration of the source and the applicator placed in the cavity.

The second aspect evaluated is the position and orientation of the primaries before and after the source and spherical applicator were translated and rotated from their initial position. Simulations of the treatment configurations with the previous version of the algorithm indicated that adaptation to such changes to the primaries was invalid. The initial position and orientation of a photon particle remained unchanged. Adjustment to position and orientation shift requires modifications to the *PrimaryGeneratorAction* and *SteppingAction* classes of the algorithm. The initial position and orientation of the primaries were set in the *PrimaryGeneratorAction*. Since the source and the spherical applicator were translated and rotated, the translation and rotation should also be applied to the primaries. The implementation in the *SteppingAction* was by analyzing the geometrics of the associated applicator. Simulations were performed with the improved algorithm. Our simulation results show that the new algorithm successfully modeled the primaries based on the position and orientation shifts. Both the trajectories of the primaries and the resulting dose distribution confirmed the validity of the new algorithm. However, the resulting dose distribution along the applicator shank in **Figure 3-3** is in the shape of a cylinder. This is expected because the presumption made with consideration that only the cylinder part of the shank is modeled, which in turns reflected in equations (2-3) and (2-15) on pages 40 and 42. The applicator shank has a complex geometry and consists not only of a cylinder but also cones (**Figure 2-12**). Equations (2-3) to equation (2-15) set the boundary for the photon particles to be scored or recorded. Particle transport and its interactions within the patient geometry during the simulation were not affected by the conditions defined by the equations.

4.1 Effects of tissue heterogeneity

The present work aims to evaluate the impact of utilizing the current dose protocol (which considers the patient a large volume of water) on the absorbed dose distribution using the developed MC dose calculation algorithm. The effects were assessed by comparing two simulation setups: Setup with and without the inclusion of patient tissue heterogeneities. Analysis of the lateral dose profiles and DVHs of the target volume and the other OARs of the simulated setups indicated that considering the patient as a homogenous volume of water overestimated the doses to the target volume and the whole breast but underestimated the absorbed doses to the lung and the heart.

In the present work, we assumed that the breast tissue consists of adipose and glandular tissues following the tissue composition data presented in the International Commission on Radiation Units and Measurements (ICRU) report 46⁵⁶. Although the radiation oncologist did not contour the adipose and the glandular tissues in the breast, they still can be distinguished in the tissue segmentation process and the resulting reconstruction geometry²³. Hence, it is possible to evaluate the effect of these tissues on the absorbed dose distributions. According to the ICRU report 46, the adipose tissue consists of 59.8% carbon and 27.8% oxygen and has a density value (ρ) of 0.950 g cm⁻³. While the glandular breast contains 33.2% carbon and 52.7% oxygen and has a density value (ρ) of 1.020 g cm⁻³. The carbon content of a material determines the fractions of photoelectric versus Compton events^{69,70}. The photoelectric effect, the dominant interaction at low-kV energy, is highly dependent on the photon energy (E) and the surrounding medium⁷¹. The higher the atomic number of the medium (Z), the larger the deposited dose in the medium. Since adipose tissue has a lower density and higher carbon content than the glandular breast tissue, a significant proportion of adipose tissue in the whole breast could significantly affect dose distribution.

Based on the elemental composition values provided by the ICRU report 46, effective atomic numbers (Z_{eff}) for water, adipose, and glandular breast tissues are 7.73, 6.67, and 7.27, respectively⁶⁹, resulting in a deviation of -13.71% and -5.95% relative to

water. This result implies that the adipose tissue has a more prominent effect on reducing the absorbed dose than the glandular tissue. Thus, a substantial proportion of the adipose increased the non-equivalent behavior of the tissue with water. The presence of the adipose tissue in place of water in the target volume (1 cm margin around the surface of the applicator) of the investigated area is lower than in the rest of the breast. The dosimetric effect of the spatial distribution of tissue types was evaluated by comparing the dose to the organs in the heterogeneous and modified homogeneous CTs. The results show a lower percentage dose to the target volume (42.62%) than to the rest of the breast (43.7%). If the 5 mm margin surrounding the applicator is used to define the target volume, the percentage dose differences between the target volume and the rest of the breast of the heterogeneous and homogeneous CTs are 40.12% and 45.62%, respectively. The differences are due to a significant glandular breast tissue distribution in the target volume compared to the rest of the breast of the 5 mm margin. For the 10 mm margin, the target volume contains more portions of the adipose tissue than the 5 mm margin (**Subfigure 2-7a**). Thus, the larger the adipose tissue composition of an organ, the larger the deviation in the absorbed dose relative to water, as expected.

The presence of muscle increased the absorbed dose of the heterogeneous CT (**Figure 3-6**). This increase is due to the density value and Z_{eff} (1.050 g cm^{-3} and 7.85, respectively), which are slightly higher than the water. As a result, the presence of muscle will increase the absorbed dose distribution. However, compared to the homogeneous CT (water), the dose increase is insignificant due to the significant impact of the adipose tissue on the absorbed dose before reaching the muscle.

The absorbed dose in the rib (**Figure 3-6**) showed a substantial elevation relative to water. The dose escalation in the rib is due to its higher relative energy absorption than the other surrounding tissues. The presence of rib increased the absorbed dose profile of the heterogeneous CT by up to 370% compared to that of water. The absorbed dose received by the rib, located 23 mm from the applicator surface, is 7.42 Gy. Despite the increase, the delivered dose is limited by the strong attenuation of the rib, as shown

by the steep dose fall-off after the radiation penetrates several voxels of the rib. The steep fall-off indicated that the effect is insignificant and insufficient to cause bone fracture. According to Overgaard *et al.*, a single fraction dose that can cause rib fracture is approximately 13 Gy-16 Gy⁷². However, the risk might be significant for an underweight woman with small breasts and if the tumor is deep-seated¹⁹. A woman with small breasts might have an increased risk of bone fracture because of the short distance between the rib and the prescription depths. If the tumor is deep, this implies that its location becomes closer to the rib bone. As a result, the rib might be exposed to a significant radiation dose. Chiavassa *et al.* reported that the right ischiopubic ramus in the pelvic area led to a dose deviation of 375% from the prescribed dose³². However, the pelvis has completely different constituent tissues compared to our investigated area. Hence, a direct comparison to our results might be irrelevant.

The absorbed dose in the lung and heart of the heterogeneous CT is very low because of their distant location from the applicator surface. However, comparisons with the absorbed doses received by the lung and heart of the homogenous CT (water) showed that the doses delivered to these organs are relatively higher for the heterogeneous CT. This is likely due to the lower absorption in the lung, which leads to a higher dose delivered to the adjacent structures. Lower absorption means more energy is delivered to the following structures.

Although the rib tends to absorb a higher dose and lower the dose delivered to the following structures, the lower absorption in the lung alters the trend at greater depths. The lung of the heterogeneous CT caused the organs situated at deeper depths to receive high doses, compared to the lung of the homogenous CT. This is because the lung in the homogeneous CT was assigned as water and thus had higher absorption. As a result, the delivered doses at greater depths are reduced significantly. **Subfigure 3-9b** shows that only 11.4% of the left lung of the homogeneous CT receives high doses, while the portion of the left lung of the heterogeneous CT that receives high doses is about 88.6% of the volume. Even though the doses delivered to at least 2% of the left lung (D2%) of both the homogeneous and the heterogeneous CTs show a

dose difference of about 35.63% at shallow depths. The difference becomes even more apparent at greater depths, with the dose difference between the homogeneous and heterogeneous CT of about -230%. The minus sign indicates that the left lung of the heterogeneous CT received a dose 230% higher than the lung of the homogeneous CT at greater depths. This also explains why the heart and the right lung of the heterogeneous CT receive higher doses than those of the homogeneous CT. The heart is known to have a higher density value such that it absorbs a higher dose than the lungs. Nevertheless, because the volume of the heart is smaller than the lung, its effect on increasing the absorbed dose was insignificant compared to the net effect of the lung on decreasing the dose values. However, if we compared these findings with the findings from the homogeneous CT, the right lung and the other adjacent organs at distant locations from the heart still receive high doses. The doses received by at least 2% of the heart and the right lung of the heterogeneous CT are 240% and 375% higher than those of the homogeneous CT, respectively (**Subfigure 3-9b**). The high absorption in the heart and right lung of the heterogeneous CT also resulted in the reduced portion of the right lung exposed to the radiation dose.

4.2 Effect of the air gap and blood interface

Dose delivery to a patient treated with the INTRABEAM device is also conducted with the presumption that there is no air or blood between the surface of the applicator and the tumor bed. In fact, as previously stated, the perfect applicator-tumor bed conformity is difficult to achieve and might alter the absorbed dose distributions. Thus, the impact of the geometric errors on the absorbed dose distributions and the absorbed dose deposited in the target volume and the other OARs of the patient were also evaluated. The geometric errors were implemented into the simulation setups by introducing the air gap or blood interface between the surface of the applicator and the tumor bed. The lateral dose profiles of the absorbed dose distributions and the DVHs of the target volume and the other OARS of the simulation setups with and without the presence of air gap or blood interface of different thicknesses were analyzed. Our results indicated that the air gap or blood interface between the surface of the applicator and the tumor

bed during the treatment should be avoided or minimized, as its presence contributes to alteration in the absorbed doses received by the target volume and the OARs. The alteration effect might not be negligible.

The presence of the 2 mm or 5 mm air gap between the applicator surface and the tumor bed resulted in a dose reduction near the prescription depths. The dose reduction is due to the lower density of air, thus, lower absorption compared to the absorption because of the glandular breast or adipose tissue at these depths. As previously mentioned, the gap or interface between the applicator surface and the tumor bed was created by replacing materials and densities of the assumed layer with either air or blood. In the reference setup, this layer consists of voxels whose materials are of the target volume (the glandular breast and adipose tissue). When this layer was replaced with air, it led to a decrease in absorption near the prescription depths. Air has a small density value ($0.00129 \text{ g cm}^{-3}$) compared to the glandular breast (1.020 g cm^{-3}) and adipose tissues (0.950 g cm^{-3}). The low-density values contributed to the low absorption of the medium. The presence of the air gap also indicated a shift to the target depths. This shift resulted in the alteration of the dose distributions of the organs within and beyond these depths (target volume, left breast, and the other OARs).

The 5 mm air gap has a more pronounced effect on reducing the dose (-48.88%) at shallow depths than the 2 mm air gap (-44.26%) (**Figure 3-11**). The reason is simply because of the difference in the thickness of the used air gap. The 5 mm air gap has a thicker layer of air than the layer of the 2 mm air gap. As a result, at shallow depths near the treatment site, the dose values of the 5 mm air gap decreased more prominently compared to the dose values of the 2 mm air gap setup. Similar trends were reported by *Tegaw et al*³⁰. According to *Tegaw et al*, the relative dose difference between depth dose profiles of the simulation setups with and without an air gap depends on the thickness of the air gap simulated. The thicker the air gap layer, the higher the relative dose difference between the compared setups. *Sethi et al* also reported that an air gap between the flat applicator and phantom led to a lower dose rate at the prescription depth with the magnitude of the reduction proportional to the

thickness of the air gap ⁷¹. Our calculated DVH of the target volume also justified these reduction effects. The doses received by at least 2% of the target volume (D2%) of the 5 mm air gap setup show a relative dose deviation of about -0.32%. While for the 2 mm air gap, the difference is -0.22%. The results indicated that an increased air gap size will lead to a higher decrease in the absorbed radiation dose in the target volume.

At 4 mm - 22 mm depths (**Figure 3-11**), the doses are increased due to the presence of glandular breast or adipose tissue, which has a higher density and, thus, higher absorption than the air. As a result, the deeper-sited normal tissues or organs received more energy because the presence of air induced low absorptions near the prescription depths. In contrast, the absorption near the prescription depths of the reference setup is high, as previously described. High absorption means lower energy delivered to the surrounding tissues or organs. The 2 mm and 5 mm air gaps have maximum effects on dose escalations at 4 mm and 5 mm depths from the applicator surface, respectively. These increases are about 6.69% and 27.38% of the reference doses (**Figure 3-11**). The increase implies that the dose enhancements are also proportional to the size of the used air gap. Comparisons of the DVHs showed that the target volumes of the error setups received higher doses (66.8% and 71.56%, respectively) than the target volume of the reference setup (**Figure 3-12**). Even though the presence of air reduced the absorbed dose close to the prescription depths, the absorbed doses at 4-22 mm depths increased, and this led to a significant dose increase to the target volume of the error setups relative to the reference setup.

Even though the D2% dose delivered to the left breast of the error setups showed an increase of about 1.98% and 3.46% higher than the reference setup, the net effect of the presence of the air gap with various thicknesses resulted in at least 75% and 82% of the left breast of the error setups to receive low doses, respectively (**Figure 3-12a**). This reduction is due to the high absorptions in the target volume leading to lower absorptions to the deeper structures. Compared to the same organ in the reference setup, the 2 mm and 5 mm air gaps brought approximately 85% and 86% of the left

lung to receive low doses, respectively. The effect is significant for the organ situated at a distal location from the applicator surface.

Nearly 99% of the heart of the error setups received low doses. Comparisons of the D2% dose values of the error setup showed that at least 2% of the heart received doses -0.49% and -0.82% lower than the reference setup, respectively. The right lung also showed a similar trend, about 37.63% and 39.13% of the volume for the error setups receiving higher doses, respectively. The air gap present between the surface of the applicator and the tumor bed also increases the portion of the right lung exposed to radiation doses. For the reference setup, the exposed proportions are about 75.15%, while for the error setups, the proportions are 76.03% and 77.15%, respectively. These seem to be a combination result of the inverse square law and the air gap effects. Low energy x-rays demonstrate dose fall off faster than typical inverse squares law ($1/r^2$) due to the additional attenuation caused by the medium⁷¹, and the presence of the air gap further reduced the absorbed dose delivered, especially to the OARs. The D2% of the right lung of the error setups shows a decreased dose value compared to the D2% of the reference setup (Table 3-2). The low D2% dose value suggested that the presence of the air gap also caused the radiation dose to be absorbed and deposited more slowly in the right lung of the error setups than in the right lung of the reference setup.

The presence of blood between the applicator and the tumor bed in the error setups also alters dose distributions of the target volume and the other OARs. When the assumed layer is replaced with blood, it increases the absorption near the treatment site (**Figure 3-14**). This high absorption is due to its higher density value (1.060 g cm^{-3}) compared to the density of the glandular (1.020 g cm^{-3}) or adipose tissues (0.950 g cm^{-3}). The magnitude of the increase is observed proportional to the size of the blood interface presented.

The dose value near the applicator surface of the 5 mm blood setup is higher than that of the 2 mm blood setup. The reason is that the portion of blood in the 5 mm setup is

thicker than in the 2 mm setup. These led to high absorption, particularly within 5 mm distances from the applicator surface. Further evaluation showed that the maximum escalation of the 2 mm and 5 mm blood interfaces was at the surface of the applicator and 5 mm depth, respectively. The presence of blood at these depths increases the reference dose value by 34.83% and 89.12%, respectively. **Figure 3-15** revealed that the 2 mm blood interface caused at least 45.29% of the target volume of the setup to receive higher doses than the target volume of the reference setup. The D2% dose received by the target volume is 14.10 Gy (**Table 3-3**). On the other hand, the presence of the 5 mm blood interface led to dose escalations to up to 69.54% of the target volume of the setup. The maximum absorbed dose in at least 2% of the target volume (D2%) is 14.99 Gy.

The absorbed doses varied beyond the depths of 5 mm. The dose profiles of the error setups after passing through several voxels of the glandular breast or adipose tissues were lower than the reference setup (**Figure 3-14**). However, the doses increased again after penetrating the muscle and rib. These fluctuations are the cumulative impacts of the inverse square law/tissue inhomogeneity and the blood interface effects. As a result, the overall doses delivered to the left breast of the error setups were higher than in the reference setup. In the 2 mm and 5 mm error setups, up to 5.3% and 5.9% of the left breast received lower doses than the reference setup. The left lung and the heart received higher doses, while less than 0.01% of these organs obtained lower doses than the reference setup. For the right lung, the overall doses delivered to the right lung of the error setups are higher than in the reference setup. However, the presence of blood reduced the portion of the right lung receiving the radiation dose. The fractions of the right lung receiving high doses were about 75.15% for the reference setup and 74.55% and 73.85% for the error setups. Of that, up to 26.85% and 27.69% of the right lung of the error setups receive lower doses than the reference setup, respectively.

Based on our results and analyses, the presence of air or blood between the surface of the applicator and the tumor bed is not negligible and, thereby, could compromise

the treatment⁵⁷. Its impacts on dose distributions shift the absorbed dose delivered to the target volume and the other OARs. The target volume might receive lower or higher doses than the intended dose. If the target volume received lower doses than the expected doses, this will reduce the effectivity of the treatment on killing the residual cancer cells in the tumor bed. It might also increase the possibility of breast necrosis as the normal breast tissue receives a higher dose¹⁹. If the target volume received high doses, the chance of adverse skin reaction might increase, especially if the resection is near the skin surface¹⁹. Alteration of the absorbed doses to the OARs might also lead to the probability of inducing secondary cancers. It is widely known that small radiation doses to organs located far from the tumor volume can cause secondary cancers⁷³.

4.3 The dose uncertainty

The comparisons of the uncertainty between the heterogeneous and the homogeneous CTs show that considering the patient tissue heterogeneity decreased the resulting uncertainty value. The reduced value can be related to the 50% criteria used in the scored dose uncertainty (Section 2.10, page 55). Based on this criteria, the calculated dose uncertainty depends upon the number of voxels included in the calculation and the number of particles within these voxels⁶⁰. The reduced uncertainty value of the heterogeneous CT is due to the increased number of voxels included in the calculation and the number of particles within these voxels. Previous analysis shows that the inconsideration of patient tissue heterogeneity overestimated the absorbed dose in the target volume and left breast. This also implies that the energy delivered to the deeper-sited organs is reduced when considering heterogeneity. However, since in the homogeneous water CT, the absorbed doses decreased significantly compared to the heterogeneous CT, the deposited dose in the heart and the left lung of the heterogeneous CT increased, as previously described. The increase in energy deposited resulted in more secondary particles produced from the interaction of the particles with the tissues included in the simulation. This is also the reason for

the decreased proportion of the right lung of the heterogeneous CT receiving the absorbed doses.

The air gap and blood interfaces also alter the calculated uncertainty value. The presence of the 2 mm air increased the uncertainty value, while the 5 mm air gap caused the uncertainty value to decrease. **Figure 3-16** shows that the uncertainty value of the 5 mm air setup becomes lower than the reference setup when the number of particles included in the simulation is more than 1.875×10^9 particles. This is most likely due to the decreased energy absorption near the prescription dose and high energy after passing through this depth because of the 5 mm air gap. Lower energy absorption close to the prescription depths means more energy penetrating the adjacent structures, and more secondary particles are produced because of the interaction of the particle and the tissue within the voxels. For the 2 mm air gap, the high energy absorption close to the applicator surface resulted in high energy absorption to the following structures, but the increased absorbed doses were insignificant after reaching a certain depth compared to the 5 mm air setup (see **Figure 3-17**). This caused the calculated dose uncertainty of the 2 mm air gap to reduce more slowly than the 5 mm air gap. The presence of blood increased the dose uncertainty in the error setups. The increased value implies that the presence of blood increases the absorbed dose close to the depths where the blood is present. High absorption led to lower energy absorption to the deeper-sited structure. The reduced energy absorption means fewer particles within the adjacent voxels. Based on **Figure 3-18**, the calculated dose uncertainty of the 5 mm blood setup decreased more gradually than the 2 mm blood gap.

Thus, it is essential to minimize the presence of the air gap or blood interface between the surface of the applicator and the tumor bed, as their presence also compromises the simulation accuracy. Nevertheless, one could improve the simulation accuracy by simulating more primary particles. However, this required significant time for a simulation to run and computer memory to process the results.

4.4 Limitations and future works

The result presented in this work is based on the simulation of a single patient. We believe that a similar tendency will be observed for different anatomies, even though the values in **Table 3-1** may vary from patient to patient. This is based on the fact that the breast contains varying amounts of adipose tissue (**Table 3-1**), which effectively decreases the electron density of the breast relative to water ²³. As a result, the heterogeneous target has lower attenuation than the homogenous target volume due to lower attenuation and higher penetration of the beam, resulting in more penetration to the adjacent normal tissues.

The dose distributions for the 3.5 cm spherical applicator were analyzed in this work. Even though the dose delivered by the INTRABEAM device with the application of a spherical applicator following the TARGIT protocol varies depending on the diameter of the used applicator ⁷⁴, the impact of patient tissue heterogeneity on dose distribution will not depend on the applicator's diameter ³².

Several MC studies have used realistic patient or anthropomorphic phantom CT datasets for different treatment sites with the INTRABEAM device ^{32,63,75}. The authors described that during CT acquisitions, the applicator was placed in a tumor bed within the body, ensuring the fixed position and orientation of the XRS and the applicator within the tumor cavity. This approach eliminates the need to model the treatment setup before conducting the simulation. However, performing surgical procedures and placing the XRS and applicator afterward within the tumor bed for each patient is complicated and impractical. The ideal approach would be real-time treatment planning using intraoperative CT imaging ²³. Schneider et al. conducted a study that demonstrated the possibility of using image guidance with a radiance system and intraoperative cone beam computed tomography (CBCT) for MC online treatment planning with heterogeneity correction during balloon kyphoplasty ⁷⁶. Even though the system is feasible to improve the dose calculations, the artifact present in the acquired CBCT images limits the accuracy of the approach. In addition, the procedures are also complex and time-consuming. A comparison of the result with the simulation results

with the pre-operative CT shows a dose difference as high as 50%. Hence, as long as difficulties regarding the installation of beneficial imaging modality in the OR, as previously highlighted in the preceding section, and limitations associated with such a setup have yet to be solved, the approach we proposed is perhaps the most realistic approach to date.

Nevertheless, the developed algorithm has to be improved for tissue segmentations and assignments. We identified errors in the voxel assignment. For instance, some voxels of the patient geometry were assigned as liver instead of muscle or breast tissues instead of adipose tissues. The assignment errors are most likely because of their minor density differences. However, the effect could be significant because of their different elemental composition. A more sophisticated method to convert CT numbers to materials and densities should be used, e.g., as described by Schneider et al. ⁷⁷ and Jiang et al. ⁷⁸.

The use of pre-operative CT images might introduce uncertainty in the simulations ²³. The position and orientation of the XRS and the applicator in the cavity in our simulations were predefined without any knowledge of their actual position and orientation in the treatment configurations. Other factors like organ motions, patient position, and tumor resection were also neglected. Hence, the breast IORT treatment simulated with the algorithm may not accurately reflect the actual surgical situation. The simulation results might not depict the actual dose distribution. According to Hensley, the possible unexpected deviations of 10%-28% from the intended dose are due to incorrect assessment of target dimensions, air gaps, and blood pooling ⁸.

It must be remembered that the air gap or blood interface in this work was assumed concentric with the applicator surface, with air or blood surrounding the applicator. Although this presumption might be artificial, the findings presented in this work underline the importance of an accurate and precise dose delivery to the patient. Such that the radiation is delivered as intended and the risk of unintended effects on the other OARs is minimized.

A combination of the developed approach with an image-guided surgery could be an option ⁶³. The position and orientation of the XRS and applicator within the tumor cavity can be guided based on the predefined position and orientation of the XRS and applicator in the pre-operative CTs ⁷⁶. The radiation oncologist could also directly observe the presence of air or fluid between the surface of the applicator and the tumor bed and take precautions to ensure the optimal dose delivery to the patient. Finally, the current algorithm is not yet applicable for clinical applications since a full simulation with the algorithm requires a long computational time. The simulation should be completed within minutes, which could be achieved by optimizing the algorithm for speed and implementing variance reduction techniques ⁴⁰.

5 SUMMARY

Dose calculation algorithms are essential for radiotherapy treatment planning. A Monte Carlo-based source model was previously developed in-house for the INTRABEAM source. However, the initial version of the algorithm was limited to dose calculation in a homogenous medium. We overcome this problem by developing the algorithm to compute the absorbed dose in a patient. Using the developed algorithm, the absorbed doses delivered to the target volume and the relevant organs at risk have been accurately quantified for an IORT treatment of a breast cancer patient with the INTRABEAM source. Based on the analyses, the dose distributions in the target volume and the OARs of the heterogeneous patient CT differ considerably from water and depend mainly on density, elemental tissue composition, and the distance from the applicator surface. Although the results presented in this work are based on the simulation of a single patient, we infer that the assumption of a homogeneous patient likely overestimates the dose to the target volume and underestimates the absorbed doses to the organs at risk. The results also reveal that the presence of air led to a dose escalation in the target volume but a dose reduction in the rest of the breast, heart, and lungs. The blood present between the surface of the applicator and the tumor bed, on the other hand, led to a dose escalation in the target volume, the rest of the left breast, and the other OARs. These results highlighted the importance of minimizing the presence of air or blood during the treatment, as its presence could significantly alter the absorbed doses in the target volume and the other OARs, which in turn affects the treatment outcomes. This knowledge will aid the accurate comparison of this technique with alternative techniques and help the clinical decision-making process.

6 REFERENCE LIST

1. Veronesi, U., Zucali, R. & Luini, A. Local control and survival in early breast cancer: The milan trial. *Int. J. Radiat. Oncol. Biol. Phys.* **12**, 717–720 (1986).
2. Williams, N. R., Pigott, K. H. & Keshtgar, M. R. S. Intraoperative Radiotherapy in the Treatment of Breast Cancer: A Review of the Evidence. *Int. J. Breast Cancer* **2011**, 1–7 (2011).
3. Clarke, M. *et al.* Effects of radiotherapy and of differences in the extent of surgery for early breast cancer on local recurrence and 15-year survival: an overview of the randomised trials. *Lancet* **366**, 2087–2106 (2005).
4. Fowble, B., Solin, L. J., Schultz, D. J., Rubenstein, J. & Goodman, R. L. Breast recurrence following conservative surgery and radiation: patterns of failure, prognosis, and pathologic findings from mastectomy specimens with implications for treatment. *Int. J. Radiat. Oncol. Biol. Phys.* **19**, 833–842 (1990).
5. Evans, S. B. & Higgins, S. A. Intraoperative radiotherapy for breast cancer: Deceptively simple? *Oncol. (United States)* **27**, 1–8 (2013).
6. Calvo, F. A., Meirino, R. M. & Orecchia, R. Intraoperative radiation therapy. First part: Rationale and techniques. *Crit. Rev. Oncol. Hematol.* **59**, 106–115 (2006).
7. Wenz, F., Pasciuti, K. & Herskind, C. *Targeted Intraoperative Radiotherapy in Oncology*. (Springer-Verlag Berlin Heidelberg, 2014). doi:10.1007/978-3-642-39821-6
8. Hensley, F. W. Present state and issues in IORT Physics. *Radiat. Oncol.* **12**, 1–30 (2017).
9. Paunesku, T. & Woloschak, G. E. Future directions of intraoperative radiation therapy: A brief review. *Front. Oncol.* **7**, 5–8 (2017).
10. Dinsmore, M. *et al.* A new miniature x-ray source for interstitial radiosurgery:

- Device description. *Med. Phys.* **23**, 45–52 (1996).
11. Esposito, E. *et al.* Intraoperative radiotherapy in early breast cancer. *Br. J. Surg.* **102**, 599–610 (2015).
 12. Schneider, F. *et al.* Development of a Novel Method for Intraoperative Radiotherapy During Kyphoplasty for Spinal Metastases (Kypho-IORT). *Int. J. Radiat. Oncol.* **81**, 1114–1119 (2011).
 13. Wenz, F. *et al.* Kypho-IORT - a novel approach of intraoperative radiotherapy during kyphoplasty for vertebral metastases. *Radiat. Oncol.* **5**, 5–8 (2010).
 14. Giordano, F. A., Wenz, F. & Petrecca, K. Rationale for intraoperative radiotherapy in glioblastoma. *Journal of Neurosurgical Sciences* (2016).
 15. Guo, S. *et al.* Intraoperative radiation therapy with the photon radiosurgery system in locally advanced and recurrent rectal cancer: retrospective review of the Cleveland clinic experience. *Radiat. Oncol.* **7**, 1 (2012).
 16. Emami, B. *et al.* Intraoperative Radiation Therapy in Head and Neck Cancers. *Int. J. Radiat. Oncol.* **99**, E335–E336 (2017).
 17. Amini, S., Viera, M. H., Valins, W. & Berman, B. Nonsurgical innovations in the treatment of nonmelanoma skin cancer. *J. Clin. Aesthet. Dermatol.* **3**, 20–34 (2010).
 18. Schneider, F. *et al.* A Novel Device for Intravaginal Electronic Brachytherapy. *Int. J. Radiat. Oncol. • Biol. • Phys.* **74**, 1298–1305 (2009).
 19. Ebert, M. A. & Carruthers, B. Dosimetric characteristics of a low-kV intraoperative x-ray source: Implications for use in a clinical trial for treatment of low-risk breast cancer. *Med. Phys.* **30**, 2424–2431 (2003).
 20. Liu, Q., Schneider, F., Ma, L., Wenz, F. & Herskind, C. Relative biologic effectiveness (RBE) of 50 kV X-rays measured in a phantom for intraoperative tumor-bed irradiation. *Int. J. Radiat. Oncol. Biol. Phys.* **85**, 1127–1133 (2013).

21. Dai, Y.-H. *et al.* Review of current perspectives on low-energy X-ray intraoperative radiotherapy in early stage breast cancer. *Ther. Radiol. Oncol.* **3**, 12–12 (2019).
22. Shaikh, M. Y., Nalichowski, A., Joiner, M. C. & Burmeister, J. Dosimetric evaluation of the INTRABEAM system for breast intraoperative radiotherapy: A single-institution experience. *Med. Dosim.* **45**, 7–12 (2020).
23. Nasir, Z. *et al.* Organ absorbed doses in the IORT treatment of breast cancer with the INTRABEAM device: a Monte-Carlo study. *Biomed. Phys. Eng. Express* **9**, (2023).
24. Nwankwo, O. MONTE CARLO SOURCE MODELS OF A KILO-VOLTAGE RADIOTHERAPY DEVICE. PhD dissertation (Ruprecht-Karls-Universität Heidelberg, 2015).
25. Culberson, W. S. *et al.* Dose-rate considerations for the INTRABEAM electronic brachytherapy system: Report from the American association of physicists in medicine task group no. 292. *Med. Phys.* **0**, 1–7 (2020).
26. Avanzo, M. *et al.* In vivo dosimetry with radiochromic films in low-voltage intraoperative radiotherapy of the breast. *Med. Phys.* **39**, 2359–2368 (2012).
27. Price, C., Pederson, A., Frazier, C. & Duttenhaver, J. In vivo dosimetry with optically stimulated dosimeters and RTQA2 radiochromic film for intraoperative radiotherapy of the breast. *Med. Phys.* **40**, 1–9 (2013).
28. Enger, S. A., Vijande, J. & Rivard, M. J. Model-Based Dose Calculation Algorithms for Brachytherapy Dosimetry. *Semin. Radiat. Oncol.* **30**, 77–86 (2020).
29. Watson, P. G. F., Bekerat, H., Papaconstadopoulos, P., Davis, S. & Seuntjens, J. An investigation into the INTRABEAM miniature x-ray source dosimetry using ionization chamber and radiochromic film measurements. *Med. Phys.* **45**, 4274–4286 (2018).

30. Tegaw, E. M., Gholami, S., Omyan, G. & Geraily, G. Dosimetric characteristics of the INTRABEAM® system with spherical applicators in the presence of air gaps and tissue heterogeneities. *Radiat. Environ. Biophys.* **59**, 295–306 (2020).
31. Vaidya, J. S. *et al.* An international randomised controlled trial to compare TARGeted Intraoperative radioTherapy (TARGIT) with conventional postoperative radiotherapy after breast-conserving surgery for women with early-stage breast cancer (the TARGIT-A trial). *Health Technol. Assess. (Rockv)*. **20**, vii–188 (2016).
32. Chiavassa, S. *et al.* Monte Carlo evaluation of the effect of inhomogeneities on dose calculation for low energy photons intra-operative radiation therapy in pelvic area. *Phys. Medica* **31**, 956–962 (2015).
33. Trifiletti, D. M. *et al.* Intraoperative breast radiation therapy with image guidance: Findings from CT images obtained in a prospective trial of intraoperative high-dose-rate brachytherapy with CT on rails. *Brachytherapy* **14**, 919–924 (2015).
34. Moradi, F. *et al.* Monte Carlo skin dose simulation in intraoperative radiotherapy of breast cancer using spherical applicators. *Phys. Med. Biol.* **62**, 6550–6566 (2017).
35. Schneider, F. *et al.* OC-0362: Precision IORT - image guided IORT including online CBCT based Monte Carlo treatment planning. *Radiother. Oncol.* **123**, S194–S195 (2017).
36. Eaton, D. J. Quality assurance and independent dosimetry for an intraoperative x-ray device. *Med. Phys.* (2012). doi:10.1118/1.4761865
37. Shamsabadi, R., Baghani, H. R., Azadegan, B. & Mowlavi, A. A. Monte Carlo based analysis and evaluation of energy spectrum for low-kV IORT spherical applicators. *Z. Med. Phys.* **30**, 60–69 (2020).
38. Alvarez, D. S. A. *et al.* Monte Carlo calculation of the TG-43 dosimetry parameters for the INTRABEAM source with spherical applicators. *Phys. Med.*

- Biol.* **66**, (2021).
39. Vidal, M. *et al.* Fast optimized Monte Carlo phase-space generation and dose prediction for low energy x-ray intra-operative radiation therapy. *Phys. Med. Biol.* **64**, (2019).
 40. Nwankwo, O., Clausen, S., Schneider, F. & Wenz, F. A virtual source model of a kilo-voltage radiotherapy device. *Phys. Med. Biol.* **58**, 2363–2375 (2013).
 41. Aichambault, L. *et al.* Overview of Geant4 applications in medical physics. in *IEEE Nuclear Science Symposium Conference Record* (2003). doi:10.1109/nssmic.2003.1352215
 42. Carl Zeiss. INTRABEAM 600 Technical Specification EN - Zeiss. Available at: https://www.zeiss.com/content/dam/med/ref_international/products/intrabeam-600/pdf/zeiss-intrabeam-600.pdf. (Accessed: 3rd August 2021)
 43. Eaton, D. J. & Duck, S. Dosimetry measurements with an intra-operative x-ray device. *Phys. Med. Biol.* **55**, (2010).
 44. Beatty, J. *et al.* A new miniature x-ray device for interstitial radiosurgery: Dosimetry. *Med. Phys.* **23**, 53–62 (1996).
 45. Carl Zeiss. Intraoperative Radiotherapy (IORT) for Breast Cancer. Available at: <https://www.zeiss.com/meditec/int/products/intraoperative-radiotherapy-iort/breast-cancer-iort.html>. (Accessed: 15th September 2019)
 46. Aichambault, L. *et al.* Overview of Geant4 applications in medical physics. *IEEE Nucl. Sci. Symp. Conf. Rec.* **3**, 1743–1745 (2003).
 47. Guatelli, S., Cutajar, D., Oborn, B. & Rosenfeld, A. B. Introduction to the geant4 simulation toolkit. *AIP Conf. Proc.* **1345**, 303–322 (2011).
 48. Geant4. Geant4 User ' s Guide for Toolkit Developers. 1–71 (2013).
 49. Pia, M. G. The Geant4 Toolkit. *Nucl. Phys. B-Proceedings Suppl.* **125**, 60–68 (2003).

50. Enger, S. A. *et al.* Layered mass geometry: A novel technique to overlay seeds and applicators onto patient geometry in Geant4 brachytherapy simulations. *Phys. Med. Biol.* **57**, 6269–6277 (2012).
51. Hubert-Tremblay, V., Archambault, Louis and Jarlskog, C. & Beaulieu, L. *GEANT4 DICOM Documentation*.
52. Hongyu Jiang, Seco, J. & Paganetti, H. Effects of Hounsfield number conversion on CT based proton Monte Carlo dose calculations. *Bone* **34**, 1439–1449 (2007).
53. Varma, D. Managing DICOM images: Tips and tricks for the radiologist. *Indian J. Radiol. Imaging* **22**, 4–13 (2012).
54. Oliveira, A. C. H. & Lima, F. R. A. Computational tools for the construction of calibration curves for use in dose calculations in radiotherapy treatment planning. *Int. Nucl. Inf. Syst.* **43**, (2011).
55. Gammex. CT QA Solution CT Electron Density Phantom. 2 (2015).
56. White, D. R., Griffith, R. V & Wilson, I. J. Report 46. *J. Int. Comm. Radiat. Units Meas.* **os24**, NP-NP (2016).
57. Sethi, A., Emami, B., Small, W. & Thomas, T. O. Intraoperative Radiotherapy With INTRABEAM: Technical and Dosimetric Considerations. *Front. Oncol.* **8**, 74 (2018).
58. Herskind, C., Griebel, J., Kraus-Tiefenbacher, U. & Wenz, F. Sphere of Equivalence-A Novel Target Volume Concept for Intraoperative Radiotherapy Using Low-Energy X Rays. *Int. J. Radiat. Oncol. Biol. Phys.* **72**, 1575–1581 (2008).
59. Cosmo, G. The Geant4 geometry modeler. *IEEE Nucl. Sci. Symp. Conf. Rec.* **4**, 2196–2198 (2004).
60. McCarthy, D. J. A Study on the Comparison of the Dose Distributions of Low kV X-Ray Radiation in Generically Modulated Bone and CT Scanned Bone.

(Heidelberg University, 2017).

61. Nwankwo, O. User manual for the INTRABEAM ® Virtual Source Model algorithm. (2016).
62. Popescu, I. A., Shaw, C. P., Zavgorodni, S. F. & Beckham, W. A. Absolute dose calculations for Monte Carlo simulations of radiotherapy beams. *Phys. Med. Biol.* **50**, 3375–3392 (2005).
63. Bouzid, D. *et al.* Monte-Carlo dosimetry for intraoperative radiotherapy using a low energy x-ray source. *Acta Oncol. (Madr)*. **54**, 1788–1795 (2015).
64. Deasy, J. O., Blanco, A. I. & Clark, V. H. CERR: A computational environment for radiotherapy research. *Med. Phys.* **30**, 979–985 (2003).
65. Chetty, I. J. *et al.* Report of the AAPM Task Group No. 105: Issues associated with clinical implementation of Monte Carlo-based photon and electron external beam treatment planning. *Med. Phys.* **34**, 4818–4853 (2007).
66. Tyagi, N. *et al.* Experimental verification of a Monte Carlo-based MLC simulation model for IMRT dose calculations in heterogeneous media. *J. Phys. Conf. Ser.* **102**, (2008).
67. Walters, B. R. B., Kawrakow, I. & Rogers, D. W. O. History by history statistical estimators in the BEAM code system. *Med. Phys.* **29**, 2745–2752 (2002).
68. Rogers, D. W. O. & Mohan, R. Questions for comparison of clinical Monte Carlo codes. in *The Use of Computers in Radiation Therapy* **6**, 120–122 (Springer, 2000).
69. Landry, G. *et al.* Sensitivity of low energy brachytherapy Monte Carlo dose calculations to uncertainties in human tissue composition. *Med. Phys.* **37**, 5188–5198 (2010).
70. Luc, B. *et al.* Report of the Task Group 186 on model-based dose calculation methods in brachytherapy beyond the TG-43 formalism : Current status. *Med.*

- Phys.* **39**, 6208–6236 (2012).
71. Sethi, A. *et al.* Tissue inhomogeneity corrections in low-kV intra-operative radiotherapy (IORT). *Transl. Cancer Res.* **4**, 182–188 (2015).
 72. Overgaard, M. Spontaneous Radiation-Induced Rib Fractures in Breast Cancer Patients Treated with Postmastectomy Irradiation—A Clinical Radiobiological Analysis of the Influence of Fraction Size and Dose-Response Relationships on Late Bone Damage. *Acta Oncol. (Madr)*. **27**, 117–122 (1988).
 73. Aziz, M. H. *et al.* Estimation of Second Cancer Risk after IORT, APBI, m-IMRT and VMAT using NCRP Report 116 for Breast Cancer. *Int. J. Sci. Eng. Res.* **4**, 4106 (2013).
 74. Watson, P. G. F. *et al.* Clinical Implication of Dosimetry Formalisms for Electronic Low-Energy Photon Intraoperative Radiation Therapy. *Pract. Radiat. Oncol.* **11**, e114–e121 (2021).
 75. Bouzid, D., BouSSION, N., Bert, J., Pradier, O. & Visvikis, D. A simulation based dosimetric study for a Kypho-IORT treatment using intrabeam™. *Transl. Cancer Res.* **3**, 83–87 (2014).
 76. Schneider, F. *et al.* Precision IORT – Image guided intraoperative radiation therapy (igIORT) using online treatment planning including tissue heterogeneity correction. *Phys. Medica* **37**, 82–87 (2017).
 77. Schneider, W., Bortfeld, T. & Schlegel, W. Correlation between CT numbers and tissue parameters needed for Monte Carlo simulations of clinical dose distributions. *Phys. Med. Biol.* **45**, 459–478 (2000).
 78. Jiang, H. & Paganetti, H. Adaptation of GEANT4 to Monte Carlo dose calculations based on CT data. *Med. Phys.* **31**, 2811–2818 (2004).

7.2 The reconstructed patient geometry

Some codes used to build or reconstruct the patient geometry are as follows,

```
ZeissDetectorConstruction.cc
ZeissDetectorConstruction::InitialisationOfMaterials()

4304
4305
4306 void ZeissDetectorConstruction::ConstructPatient()
4307 {
4308     ReadPhantomData();
4309     ConstructPhantomContainer();
4310     ConstructDicom();
4311 }
4312
4313
4314
4315 void ZeissDetectorConstruction::InitialisationOfMaterials()
4316 {
4317     //Creating elements:
4318
4319     G4double z, a;
4320     G4String name, symbol;
4321
4322     G4Element* eIC = new G4Element(name = "Carbon", symbol = "C", z = 6.0, a = 12.011* g/mole);
4323     G4Element* eIH = new G4Element(name = "Hydrogen", symbol = "H", z = 1.0, a = 1.008* g/mole);
4324     G4Element* eIN = new G4Element(name = "Nitrogen", symbol = "N", z = 7.0, a = 14.007* g/mole);
4325     G4Element* eIO = new G4Element(name = "Oxygen", symbol = "O", z = 8.0, a = 16.00* g/mole);
4326     G4Element* eINa = new G4Element(name = "Sodium", symbol = "Na", z = 11.0, a = 22.98977* g/mole);
4327     G4Element* eIS = new G4Element(name = "Sulfur", symbol = "S", z = 16.0, a = 32.065* g/mole);
4328     G4Element* eICl = new G4Element(name = "Chlorine", symbol = "P", z = 17.0, a = 35.453* g/mole);
4329     G4Element* eIK = new G4Element(name = "Potassium", symbol = "P", z = 19.0, a = 39.0983* g/mole);
4330     G4Element* eIP = new G4Element(name = "Phosphorus", symbol = "P", z = 30, a = 30.973976* g/mole);
4331     G4Element* eIfe = new G4Element(name = "Iron", symbol = "Fe", z = 26, a = 56.845* g/mole);
4332     G4Element* eIMg = new G4Element(name = "Magnesium", symbol = "Mg", z = 12.0, a = 24.3050* g/mole);
4333     G4Element* eICa = new G4Element(name = "Calcium", symbol = "Ca", z = 20.0, a = 40.078* g/mole);
4334
4335     //Creating Materials:
4336     G4int numberOfElements;
4337
4338     //Creating Air
4339     G4double density_air = 1.290*mg/cm3;
4340     fAir = new G4Material("Air", density_air, numberOfElements = 2);
4341
4342     fAir->AddElement(eIN, 0.7); //0.7 and 0.3 is fraction mass, which are 70% and 30% respectively
4343     fAir->AddElement(eIO, 0.3);
4344
4345     //Lung Inhale
4346     G4double density_lung = 0.260*g/cm3;
4347     G4Material* lunginhale = new G4Material("LungInhale", density_lung, numberOfElements = 9);
4348
4349     lunginhale->AddElement(eIH, 0.103);
4350     lunginhale->AddElement(eIC, 0.105);
4351     lunginhale->AddElement(eIN, 0.031);
4352     lunginhale->AddElement(eIO, 0.749);
4353     lunginhale->AddElement(eINa, 0.002);
4354     lunginhale->AddElement(eIP, 0.002);
4355     lunginhale->AddElement(eIS, 0.003);
4356     lunginhale->AddElement(eICl, 0.003);
4357     lunginhale->AddElement(eIK, 0.002);
4358
4359     //Lung Exhale
```

```

4359 //Lung Exhale
4360 G4double density_lung2 = 0.508*g/cm3;
4361 G4Material* lungexhale = new G4Material("LungExhale", density_lung2, numberOfElements = 9);
4362
4363 lungexhale->AddElement(eIH, 0.103);
4364 lungexhale->AddElement(eIC, 0.105);
4365 lungexhale->AddElement(eIN, 0.031);
4366 lungexhale->AddElement(eIO, 0.749);
4367 lungexhale->AddElement(eINa, 0.002);
4368 lungexhale->AddElement(eIP, 0.002);
4369 lungexhale->AddElement(eIS, 0.003);
4370 lungexhale->AddElement(eICl, 0.003);
4371 lungexhale->AddElement(eIK, 0.002);
4372
4373 //Adipose Tissue
4374 G4double density_AT = 0.950*g/cm3;
4375 G4Material* adiposeTissue = new G4Material("AdiposeTissue", density_AT, numberOfElements = 7);
4376
4377 adiposeTissue->AddElement(eIH, 0.114);
4378 adiposeTissue->AddElement(eIC, 0.598);
4379 adiposeTissue->AddElement(eIN, 0.007);
4380 adiposeTissue->AddElement(eIO, 0.278);
4381 adiposeTissue->AddElement(eINa, 0.001);
4382 adiposeTissue->AddElement(eIS, 0.001);
4383 adiposeTissue->AddElement(eICl, 0.001);
4384
4385 //Breast
4386 G4double density_Br = 1.020*g/cm3;
4387 G4Material* breast = new G4Material("Breast", density_Br, numberOfElements = 8);
4388 breast->AddElement(eIH, 0.106);
4389 breast->AddElement(eIC, 0.332);
4390 breast->AddElement(eIN, 0.030);
4391 breast->AddElement(eIO, 0.527);
4392 breast->AddElement(eINa, 0.001);
4393 breast->AddElement(eIP, 0.001);
4394 breast->AddElement(eIS, 0.002);
4395 breast->AddElement(eICl, 0.001);
4396
4397 //Water
4398 G4double density_water = 1.0*g/cm3;
4399 G4Material* water = new G4Material("Water", density_water, numberOfElements = 2);
4400
4401 water->AddElement(eIH, 0.112);
4402 water->AddElement(eIO, 0.888);
4403
4404 //Muscle
4405 G4double density_muscle = 1.050*g/cm3;
4406 G4Material* muscle = new G4Material("Muscle", density_muscle, numberOfElements = 9);
4407
4408 muscle->AddElement(eIH, 0.102);
4409 muscle->AddElement(eIC, 0.143);
4410 muscle->AddElement(eIN, 0.034);
4411 muscle->AddElement(eIO, 0.710);
4412 muscle->AddElement(eINa, 0.001);
4413 muscle->AddElement(eIP, 0.002);
4414 muscle->AddElement(eIS, 0.003);
4415
4416 //Liver
4417 G4double density_liver = 1.060*g/cm3;
4418 G4Material* liver = new G4Material("Liver", density_liver, numberOfElements = 9);
4419
4420 liver->AddElement(eIH, 0.102);
4421 liver->AddElement(eIC, 0.139);
4422 liver->AddElement(eIN, 0.030);
4423 liver->AddElement(eIO, 0.716);
4424 liver->AddElement(eINa, 0.002);
4425 liver->AddElement(eIP, 0.003);
4426 liver->AddElement(eIS, 0.003);
4427 liver->AddElement(eICl, 0.002);
4428 liver->AddElement(eIK, 0.003);
4429
4430 //Trabecular Bone
4431 G4double density_TB = 1.180*g/cm3;
4432 G4double density_TB = 1.410*g/cm3; // rib
4433 G4Material* trabecularBone = new G4Material("TrabecularBone", density_TB, numberOfElements = 11);
4434 trabecularBone->AddElement(eIH, 0.064);
4435 trabecularBone->AddElement(eIC, 0.263);
4436 trabecularBone->AddElement(eIN, 0.039);
4437 trabecularBone->AddElement(eIO, 0.436);
4438 trabecularBone->AddElement(eINa, 0.001);
4439 trabecularBone->AddElement(eIMg, 0.001);
4440 trabecularBone->AddElement(eIP, 0.060);
4441 trabecularBone->AddElement(eIS, 0.003);
4442 trabecularBone->AddElement(eICl, 0.001);
4443 trabecularBone->AddElement(eIK, 0.001);
4444 trabecularBone->AddElement(eICa, 0.131);
4445
4446 //Dense Bone
4447 G4double density_DB = 1.920*g/cm3;
4448 G4Material* denseBone = new G4Material("DenseBone", density_DB, numberOfElements = 9);
4449
4450 denseBone->AddElement(eIH, 0.034);
4451 denseBone->AddElement(eIC, 0.155);
4452 denseBone->AddElement(eIN, 0.042);
4453 denseBone->AddElement(eIO, 0.435);
4454 denseBone->AddElement(eINa, 0.001);
4455 denseBone->AddElement(eIMg, 0.002);
4456 denseBone->AddElement(eIP, 0.103);
4457 denseBone->AddElement(eIS, 0.003);
4458 // denseBone->AddElement(eICl, 0.001);
4459 //denseBone->AddElement(eIK, 0.001);
4460 denseBone->AddElement(eICa, 0.225);
4461
4462
4463
4464
4465

```

```

4480 //Blood
4481 G4double density_blood = 1.060*g/cm3;
4482 G4Material* blood = new G4Material("blood", density_blood, numberOfElements = 10);
4483
4484 blood->AddElement(eIH, 0.102);
4485 blood->AddElement(eIC, 0.110);
4486 blood->AddElement(eIN, 0.033);
4487 blood->AddElement(eIO, 0.745);
4488 blood->AddElement(eINa, 0.001);
4489 blood->AddElement(eIP, 0.001);
4490 blood->AddElement(eIS, 0.002);
4491 blood->AddElement(eICl, 0.003);
4492 blood->AddElement(eIK, 0.002);
4493 blood->AddElement(eIFe, 0.001);
4494
4495
4496 //Put the material in a vector //What is this??
4497 fOriginalMaterials.push_back(fAir); // rho = 0.00129, this is density
4498 fOriginalMaterials.push_back(lunginhale); // rho = 0.217
4499 fOriginalMaterials.push_back(lungexhale); // rho = 0.508
4500 fOriginalMaterials.push_back(adiposeTissue); // rho = 0.967
4501 fOriginalMaterials.push_back(breast); // rho = 0.990
4502 fOriginalMaterials.push_back(water); // rho = 1.018
4503 fOriginalMaterials.push_back(muscle); // rho = 1.061
4504 fOriginalMaterials.push_back(liver); // rho = 1.071
4505 fOriginalMaterials.push_back(trabecularBone); // rho = 1.159
4506 fOriginalMaterials.push_back(denseBone); // rho = 1.575
4507 fOriginalMaterials.push_back(ULTEM_PEI); // rho = 1.159
4508 fOriginalMaterials.push_back(blood); // rho = 1.575
4509
4510 }
4511
4512
4513 void ZeissDetectorConstruction::ReadPhantomData()
4514 {
4515
4516     G4String dataFile = "Data.dat";
4517     std::ifstream finDF(dataFile.c_str());
4518     G4String fname;
4519     if(finDF.good() != 1 ) {
4520         G4String descript = "Problem reading data file: "+ dataFile;
4521         G4Exception(" ZeissDetectorConstruction::ReadPhantomData",
4522             "",
4523             FatalException,
4524             descript);
4525     }
4526
4527     G4int compression;
4528     finDF >> compression; // not used here
4529
4530     finDF >> fNoFiles;
4531     for(G4int i = 0; i < fNoFiles; i++ ) {
4532         finDF >> fname;
4533         //--- Read one data file
4534         fname += ".g4cdcm"; //loop to read the number of files, passing the filename as arguments
4535         ReadPhantomDataFile(fname); //read the file name

```

```

4697 void ZeissDetectorConstruction::ConstructPhantomContainer()
4698 {
4699     //---- Extract number of voxels and voxel dimensions
4700     fNVoxelX = fZSliceHeaderMerged->GetNoVoxelX();
4701     fNVoxelY = fZSliceHeaderMerged->GetNoVoxelY();
4702     fNVoxelZ = fZSliceHeaderMerged->GetNoVoxelZ();
4703
4704     fVoxelHalfDimX = fZSliceHeaderMerged->GetVoxelHalfX();
4705     fVoxelHalfDimY = fZSliceHeaderMerged->GetVoxelHalfY();
4706     fVoxelHalfDimZ = fZSliceHeaderMerged->GetVoxelHalfZ();
4707 #ifdef G4VERBOSE
4708     G4cout << " fNVoxelX " << fNVoxelX << " fVoxelHalfDimX " << fVoxelHalfDimX
4709     <<G4endl;
4710     G4cout << " fNVoxelY " << fNVoxelY << " fVoxelHalfDimY " << fVoxelHalfDimY
4711     <<G4endl;
4712     G4cout << " fNVoxelZ " << fNVoxelZ << " fVoxelHalfDimZ " << fVoxelHalfDimZ
4713     <<G4endl;
4714     G4cout << " totalPixels " << fNVoxelX*fNVoxelY*fNVoxelZ << G4endl;
4715 #endif
4716
4717     //---- Define the volume that contains all the voxels
4718     fContainer_solid = new G4Box("phantomContainer",fNVoxelX*fVoxelHalfDimX,
4719     fNVoxelY*fVoxelHalfDimY,
4720     fNVoxelZ*fVoxelHalfDimZ);
4721
4722     // Creating sphere for hole
4723     G4double rMax = 17.5*mm;
4724     G4Orb* sSphere_1 = new G4Orb ("cavity", rMax);
4725     //Tube
4726     G4ThreeVector pos1 = G4ThreeVector(0 *mm, 0 *mm, 0 *mm); //sphere1
4727     G4RotationMatrix* zRot = new G4RotationMatrix; //assumed not rotate.
4728     zRot->rotateZ(0.*deg);
4729     zRot->rotateY(-90.*deg);
4730     G4double pSPhi = 0. *deg;
4731     G4double pDPhi = 360 *deg;
4732
4733     G4String t1_name_35 = "Tube1";
4734     G4double pRMin_1 = 0. *mm;
4735     G4double pRMax_1 = 6.25 *mm;
4736     G4double pDz_1 = (7.323 * 0.5) *mm;
4737     // G4double pDz_1 = (30) *mm;
4738     G4double ang = (180.0-159.0752);
4739     G4double posTube1_z = (0-17.5 * cos(ang*pi/180)-(7.323*0.5)) *mm;
4740     G4ThreeVector pos2 = G4ThreeVector(posTube1_z, 0 *mm, 0 *mm); //Tube1
4741     G4Tubs* sTube_1 = new G4Tubs(t1_name_35, pRMin_1, pRMax_1, pDz_1, pSPhi, pDPhi);
4742
4743     // Union Solid 1
4744     G4UnionSolid* uniSolid_1 = new G4UnionSolid("cavity_part1", sSphere_1, sTube_1, zRot, pos2);
4745
4746     //Cone1
4747     G4String c1_name_35 = "Cone1";
4748     G4double innerRad_1 = 0. *mm;
4749     G4double outerRad_1 = 9.25 *mm;
4750     G4double innerRad_2 = 0. *mm;
4751     G4double outerRad_2 = 6.25 *mm;
4752     G4double hz_1 = (10.7*0.5) *mm;
4753     G4double posCone1_z = (posTube1_z - pDz_1 - hz_1 ) *mm;

```

```

4752 G4double posCone1_z = (posTube1_z - pDz_1 - hz_1) *mm;
4753 G4ThreeVector pos3 = G4ThreeVector(posCone1_z, 0 *mm, 0 *mm); //Cone1
4754
4755 G4Cons* sCone_1 = new G4Cons(c1_name_35, innerRad_1, outerRad_1, innerRad_2, outerRad_2, hz_1, pSPhi, pDPhi);
4756
4757 G4UnionSolid* uniSolid_2 = new G4UnionSolid("cavity_part2", uniSolid_1, sCone_1, zRot, pos3);
4758
4759
4760 //Cone2
4761 G4String c2_name_35 = "Cone2";
4762 G4double innerRad_3 = 0. *mm;
4763 G4double outerRad_3 = (41.4*0.5) *mm;
4764 //G4double outerRad_3 = ((41.4*0.5)-1) *mm;
4765 G4double innerRad_4 = 0 *mm;
4766 G4double outerRad_4 = 9.25 *mm;
4767 //G4double outerRad_4 = 8.25 *mm;
4768 G4double hz_2 = (70.95*0.5) *mm;
4769 G4double posCone2_z = (posCone1_z - hz_1 - hz_2) *mm ;
4770 G4ThreeVector pos4 = G4ThreeVector(posCone2_z, 0 *mm, 0 *mm); //Cone1
4771
4772 G4Cons* sCone_2 = new G4Cons(c2_name_35, innerRad_3, outerRad_3, innerRad_4, outerRad_4, hz_2, pSPhi, pDPhi);
4773
4774 G4UnionSolid* uniSolid_3 = new G4UnionSolid("cavity_part3", uniSolid_2, sCone_2, zRot, pos4);
4775
4776 //G4ThreeVector transl(159.3, (200-189), 0);
4777 //G4ThreeVector transl(146, (200-189), 0); // untuk 378x378x233
4778 G4ThreeVector transl(110, (170-150), 0); // untuk 300x300x233
4779 //G4ThreeVector transl(110, (170-150), 0); // 300-260 = 40. 0 ditengah kr ikut world. jadi posisi cavity (150-40) = 110.
4780 G4RotationMatrix* zRot2 = new G4RotationMatrix;
4781 zRot2->rotateZ(-215.*deg);
4782 G4SubtractionSolid* fContainer_cavity = new G4SubtractionSolid("fContainer_cavity", fContainer_solid, uniSolid_2, zRot2, transl);
4783
4784
4785 fContainer_logic =
4786 new G4LogicalVolume (fContainer_cavity,
4787 //the material is not important, it will be fully filled by the voxels
4788 fMaterials[0],
4789 "fContainer_cavity",
4790 0, 0, 0 );
4791
4792 //--- Place it on the world
4793 //the patient geometry is placed by default at (0,0,0), however, its possible to change the position from messenger
4794 /*
4795 G4double fOffsetX = (fZSliceHeaderMerged->GetMaxX() + fZSliceHeaderMerged->GetMinX() ) /2.;
4796 G4double fOffsetY = (fZSliceHeaderMerged->GetMaxY() + fZSliceHeaderMerged->GetMinY() ) /2.;
4797 G4double fOffsetZ = (fZSliceHeaderMerged->GetMaxZ() + fZSliceHeaderMerged->GetMinZ() ) /2.;
4798 //patient_translation_matrix;
4799 //G4ThreeVector posCentreVoxels(0,0,0);
4800 posPhantX = fZSliceHeaderMerged->GetMaxX();
4801 posPhantY = fZSliceHeaderMerged->GetMaxY();
4802 posPhantZ = (fZSliceHeaderMerged->GetMaxZ() - fZSliceHeaderMerged->GetMinZ())/2.;
4803 //G4ThreeVector posCentreVoxels(posPhantX,posPhantY,posPhantZ);
4804 G4ThreeVector posCentreVoxels(95,-60,0);
4805 */
4806 //G4ThreeVector posCentreVoxels(135.3,-87,0);
4807 #ifdef G4VERBOSE

```

```

4807 #ifdef G4VERBOSE
4808     G4cout << " placing voxel container volume at " << patient_translation_matrix << G4endl;
4809 #endif
4810
4811     fContainer_logic->SetVisAttributes(new G4VisAttributes(G4Colour(1.,1.,1.)));
4812
4813     //G4RotationMatrix*
4814     fContainer_phys =
4815     new G4PVPlacement(0, // rotation, if you want to rotate the dicom, put patient_rot here.
4816         patient_translation_matrix,
4817         fContainer_logic, // The logic volume
4818         "fContainer_cavity", // Name
4819         l_world, // Mother
4820         false, // No op. bool.
4821         1); // Copy number
4822 }
4823 /*
4824
4825 void ZeissDetectorConstruction::SetScorer(G4LogicalVolume* voxel_logic)
4826 {
4827
4828 #ifdef G4VERBOSE
4829     G4cout << "\t SET SCORER : " << voxel_logic->GetName() << G4endl;
4830 #endif
4831
4832     fScorers.insert(voxel_logic);
4833
4834 }
4835 */
4836 void ZeissDetectorConstruction::ConstructDicom()
4837 {
4838 #ifdef G4VERBOSE
4839     G4cout << "DicomDetectorConstruction::ConstructPhantom " << G4endl;
4840 #endif
4841     //----- Create parameterisation
4842     DicomPhantomParameterisationColour* param = new DicomPhantomParameterisationColour();
4843
4844     //----- Set voxel dimensions
4845     param->SetVoxelDimensions( fVoxelHalfDimX, fVoxelHalfDimY, fVoxelHalfDimZ );
4846
4847     //----- Set number of voxels
4848     param->SetNoVoxel( fNVoxelX, fNVoxelY, fNVoxelZ );
4849
4850     //----- Set list of materials
4851     param->SetMaterials( fMaterials );
4852
4853     //----- Set list of material indices: for each voxel it is a number that
4854     // correspond to the index of its material in the vector of materials
4855     // defined above
4856     param->SetMaterialIndices( fMateIDs );
4857
4858     G4Box* voxel_solid = new G4Box( "Voxel", fVoxelHalfDimX, fVoxelHalfDimY, fVoxelHalfDimZ);
4859
4860     G4LogicalVolume* voxel_logic = new G4LogicalVolume(voxel_solid,fMaterials[0],"VoxelLogical",0,0,0);
4861     // material is not relevant, it will be changed by the
4862     // ComputeMaterial method of the parameterisation
4863     // material is not relevant, it will be changed by the
4864     // ComputeMaterial method of the parameterisation
4865
4866     voxel_logic->SetVisAttributes(new G4VisAttributes(G4VisAttributes::GetInvisible()));
4867
4868     //--- Assign the fContainer volume of the parameterisation
4869     param->BuildContainerSolid(fContainer_phys);
4870
4871     //--- Assure yourself that the voxels are completely filling the
4872     // fContainer volume
4873     param->CheckVoxelsFillContainer(fContainer_solid->GetXHalfLength(),
4874         fContainer_solid->GetYHalfLength(),
4875         fContainer_solid->GetZHalfLength() );
4876
4877     //----- The G4PVParameterised object that uses the created parameterisation
4878     // should be placed in the fContainer logical volume
4879
4880     G4PVParameterised * patient_phys = new G4PVParameterised("phantom",voxel_logic,fContainer_logic,
4881         kXAxis, fNVoxelX*fNVoxelY*fNVoxelZ, param);
4882
4883     // if axis is set as kUndefined instead of kXAxis, GEANT4 will
4884     // do an smart voxel optimisation
4885     // (not needed if G4RegularNavigation is used)
4886
4887     //----- Set this physical volume as having a regular structure of type 1,
4888     // so that G4RegularNavigation is used
4889     patient_phys->SetRegularStructureId(1); // if not set true, G4VoxelNavigation
4890     //will be used instead
4891
4892     // SetScorer(voxel_logic);
4893     fScoringVolume = patient_phys;
4894 }
4895

```

7.3 The dose points of the other OARs

Figure 7-1 shows the 3D dose data points of the left lung, heart, and right lung. The boundaries of the OARs were retrieved from the DICOM structure data of the OARs. The transversal view of dose distributions was extracted at the central axis of the corresponding dose slice.

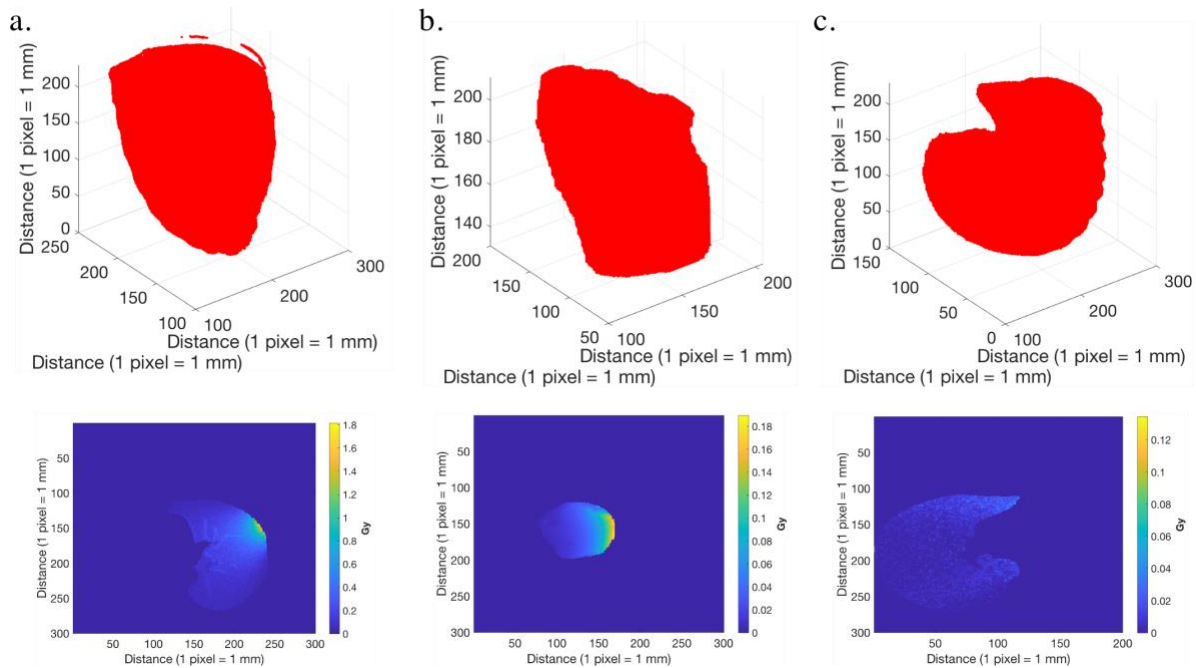


Figure 7-1. The 3D dose points of the defined OARs and their corresponding 2-D dose distributions of the associated dose slice for the a. left lung, b. heart, and c. right lung.

8 CURRICULUM VITAE

PERSONAL INFORMATION

Name: Zulfa
Date of Birth: 18-03-1987
Place of Birth: Bengkalis, Indonesia
Marital Status: Married
Father: Mohd. Nasir
Mother: Jumasnah

CONTACT INFORMATION

Jl. Perumahan UNRI, Perum. Oce Regency Blok B.08 RT.005/RW.003, Kel. Air Putih, Kec. Tampan, Kota Pekanbaru, Riau, Indonesia, 28293
Tel: +62 87798540805
zulfa@lecturer.unri.ac.id

EDUCATION

(2005-2011)

Riau University, Pekanbaru, Indonesia
B.Sc Physics (High Merit)

(2012-2014)

Institut Teknologi Bandung (ITB), Bandung Indonesia
M.Sc. Physics (High Merit)

PROFFESIONAL EXPERIENCE

(2020-present)

Lecturer, Department of Physics, Faculty of mathematics and Natural Sciences, Riau University, Kota Pekanbaru, Riau-Indonesia

(2015-present)

PhD, Geometric Errors and Effects Analysis for the INTRABEAM Source under Treatment Conditions

(Nov 2014-Feb 2015)

Visiting Researcher, Center For Medical Physics and Cancer Research Edwar Technology, Alam Sutera, Tangerang, Banten-Indonesia

WORKSHOP

(2-3 Jun, 2016)

TARGIT Academy

RESEARCH INTERESTS

Monte Carlo modelling, image processing, and analysis, IORT dosimetry

JOURNAL PUBLICATIONS

Z Nasir, L Probst, F Schneider, S Clausen, D Buergy, G Glatting, and O Nwankwo (2021). Organ absorbed doses in the IORT treatment of breast cancer with the INTRABEAM device: A Monte-Carlo study. *Biomed. Phys. Eng. Express* 9 (2023) 025013, DOI 10.1088/2057-1976/acb941

POSTERS AND PRESENTATIONS

1. **Z Nasir**, L Probst, J. Mohd Radzi, F Schneider, S Clausen¹, F A Giordano, G Glatting, and O Nwankwo (2020). Quantification of organs absorbed doses in the IORT treatment of breast cancer with the INTRABEAM device. DGMP annual meeting 2020. ID 90.
2. J. Mohd Radzi, G. Glatting, **Z. Nasir**, L.D. Jiménez-Franco, F.A. Giordano, F. Stieler (2019). The effect of shot sequence on the biological effectiveness in Gamma Knife radiosurgery. DeGBS 2019.
3. **Z. Nasir**, O. Nwankwo, F. Schneider, S. Clausen, G. Glatting, F. Wenz (2017). The effect of geometric error on dose distribution in intraoperative radiation therapy (IORT) with INTRABEAM, DEGRO annual meeting 2017. P22-4-jD.

COMPUTER PROGRAMMINGS

GEANT4, C++, MATLAB

AWARD

(2016-2020)

Indonesia Endowment Fund for Education (LPDP) Scholarship, Ministry of Finance, the Republic of Indonesia.

(2012-2014)

Graduate Scholarship for Outstanding Students (BU/BPPDN Dikti), Ministry of Education, the Republic of Indonesia.

9 ACKNOWLEDGMENTS

Alhamdulillah, praise be to Allah the Almighty of God, the most Gracious, and the most Merciful. Firstly, I would acknowledge and thank Allah for His greatness and blessing for giving me the strength and courage during the accomplishment of this thesis. May Allah's blessing goes to His final Prophet Muhammad (peace be up on him), his family and his companions.

I would like to give my utmost gratitude to Prof. Dr. Med. Daniel Bürgy, M. Sc for giving me the great opportunity, advices, and full support to finish my study despite all the obstacles I had faced during the study. I wish to express my sincere gratitude to Prof. Gerhard Glating for giving me a great opportunity to work on this project and for always being supportive during my study. I am very grateful to Dr. sc. hum. Obioma C. Nwankwo for being my second supervisor. He introduced me to the INTRABEAM source modeling and provided almost everything I needed to accomplish this project. I am very thankful for every time he has spent for our discussions as they were all very helpful to proceed every task in this project. I also wish to sincerely thank Dr. sc. hum. Frank Schneider for his supports and fruitful discussions, advices, and suggestions during the course of this work. It's because the support from him and Prof. Buergy that I could complete my thesis. I am also thankful to Dr.sc.hum. Sven Clausen for the useful discussions I had with him.

I gratefully acknowledge the funding received from the Indonesian Endowment Fund for Education, Ministry of Finance, the Republic of Indonesia throughout my doctoral degree.

Many thanks go to my best friends and colleagues, including Dr. sc. hum. Juliana Binti Mohd Radzi, Luis Probst, Dr. sc. hum. Buthayna Alnaalwa, Dr. sc. hum. Ali Atsgar Attarwala, Dr. sc. hum. Bedor Abu-Alhaj, Dr. sc. hum. Luis Jimenez-Franco for both academic and non-academic supports throughout my graduate study.

My unreserved gratitude to my mother, sister, and brothers in Indonesia. I believe it is because their loves, trusts, and prayers that I could survive in every obstacle I face in life. Finally, I am also grateful to my husband and son for making my life more colorful and meaningful.